Structural Defect Engineering of Tin (II) Sulfide Thin Films for Photovoltaics

by

Rupak Chakraborty

A.B. Physics, Harvard University (2010)
S.M. Mechanical Engineering, Massachusetts Institute of Technology (2014)

Submitted to the Department of Mechanical Engineering
in partial fulfillment of the requirements for the degree of

Doctor of Philosophy in Mechanical Engineering

at the

MASSACHUSETTS INSTITUTE OF TECHNOLOGY

June 2016

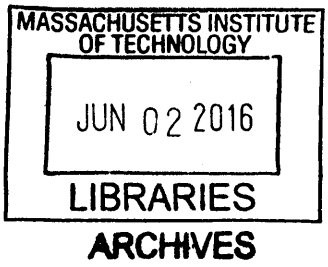

Signature redacted

Author.....
Department of Mechanical Engineering
May 2, 2016

Signature redacted

Certified by.....
Tonio Buonassisi
Associate Professor of Mechanical Engineering
Thesis Supervisor

Signature redacted

Accepted by.....
Rohan Abeyaratne
Professor of Mechanical Engineering
Chairman, Department Committee on Graduate Theses

Structural Defect Engineering of Tin (II) Sulfide Thin Films for Photovoltaics

by

Rupak Chakraborty

Submitted to the Department of Mechanical Engineering
on May 2, 2016, in partial fulfillment of the
requirements for the degree of
Doctor of Philosophy in Mechanical Engineering

Abstract

Tin (II) sulfide (SnS) is a promising Earth-abundant, non-toxic alternative to commercially available thin-film photovoltaic (PV) materials because of its near-ideal bandgap, high absorption coefficient, and potential for facile manufacturing. However, SnS-based photovoltaic devices have reached a maximum experimental efficiency of only 4.4%, compared to a theoretical maximum of 32%, primarily due to a low minority-carrier lifetime. In this work, I assess the impact of structural defects and anisotropy on the minority-carrier lifetime and other key device parameters, shedding light on the path to high-efficiency SnS-based photovoltaics.

SnS thin films are deposited by thermal evaporation in a range of growth temperatures with varying structural defect density. Extended structural defects including intragranular defects and grain boundaries are directly related to minority-carrier collection length using high-resolution correlative electron microscopy. The results suggest that intragranular point defects, as opposed to extended structural defects, are likely responsible for the short minority-carrier lifetimes in present-day SnS films.

Inhomogeneities in the polycrystalline SnS thin films due to the anisotropic material properties of SnS may also impact the device performance. Device simulations taking into account the orientation-dependent electron affinity of SnS show that a uniform grain orientation distribution is optimal. As a route toward both uniform grain orientation and low structural defect density, the anisotropic surface energy of SnS is harnessed by growth on a van der Waals-terminated substrate. An enhancement in both orientation uniformity and minority-carrier lifetime is measured, showing a promising path toward the ideal SnS film.

Lastly, the process of optimization to reduce structural defect density may be expedited by *in-situ* characterization of micro- and nanoscale defects under realistic processing conditions. Toward this end, an *in-situ* temperature stage for synchrotron X-ray spectromicrosopy is developed to track nanoscale defects up to a sample temperature of

600°C. The stage enables previously unattainable *in-situ* studies of defect kinetics, allowing both a deeper understanding of how process conditions affect defect characteristics and the ability to rapidly optimize process conditions toward a defect-free film.

Thesis Supervisor: Tonio Buonassisi
Title: Associate Professor

Acknowledgments

I have many people to thank for making this thesis possible. First, a big thank you to my large, loving family, who have all played a part in my education. A few special thanks: thank you Ma and Baba for your unending support, well beyond the academic kind, since the beginning; and thank you Sudhirmama and Samirmama for setting me on the science path: I wouldn't be here without your early mentorship.

I have been extremely fortunate to work with some exceptionally talented people during my time as a graduate student, without whom this thesis would not be possible. First, thank you Tonio for your mentorship and for bringing together the wonderful group of human beings that is the PVLab.

Thank you Katy for teaching me all the things about SnS at the beginning - you are the Godfather of SnS in the PVLab.

Thank you Vera for being my trusted lab partner for the past three years. Your support has been critical from the experimental planning stages all the way to manuscript-writing.

Thank you Jim for all your help and collaboration in the lab over the past five years - this thesis would not have happened without the decades of experience that you bring to the PVLab every week.

Some notable groups I have been privileged to work with:

SnS Team: Katy "Corleone" Hartman, Vera Steinmann, Rafael Jaramillo, Niall Mangan, Riley Brandt, Jeremy Poindexter, Alex Polizzotti

Gordon group: Roy Gordon, Prasert Sinsermsuksakul, Helen H. Park, Chuanxi Yang, Leizhi Sun

Mexico workshop team: Sergio Castellanos, Karla Franco, Rachel Kurchin, Vera Steinmann

Former PVLab mentors: Mark Winkler, Joe Sullivan, Christie Simmons, Yaron Segal

BRIDGE team: Jim Serdy, Brad West, Michael Stuckelberger, Mariana Bertoni, Barry Lai, Jörg Maser, Marty Culpepper, with help from Marcel Thomas and Aaron Ramirez

Microscopy team: Paul Rekemeyer, Amanda Youssef, Austin Akey

UROPs: Luisa Barrera, Kelsey Doolittle, Frances Lenahan

Simulation buddies: David Berney Needleman, Niall Mangan

Lifetime measurement help: Ben Ofori-Okai, Mark Wilson

Graphene help: Marek Hempel

35-135 crew: Maia Bageant, Adam Libert, Scott Nill, Larissa Nietner. Your uplifting spirits are contagious.

MIT support: Kurt Broderick, Scott Speakman, Charlie Settens

PVLab: Thank you to everyone in the PVLab! Besides being amazingly helpful with experiments, you all have made my time as a graduate student uniquely enjoyable beyond the lab.

Administrative support: Lauren Wolinsky, Allyna Nguyen

Thanks as well to my wonderful old friends: Max Parsons, Kevin Ma, Yohsuke Miyamoto, Will Quayle, Powell Graham, Peter Kim, Jason Gao, and Frances Yun. Grad school would not have been as fun without you. Thank you Amanda West for joining me and supporting me on the roller coaster that has been the last year.

And lastly, I would like to thank funding sources and shared-use facilities: NSF Graduate Research Fellowship, U.S. Department of Energy (DOE) SunShot Initiative (SERIIUS, NextGen II DE-EE0005329, and BRIDGE DE-EE0005848), Total-MIT Energy Initiative Fellowship. Use of the Advanced Photon Source, an Office of Science User Facility operated for the U.S. DOE Office of Science by Argonne National Laboratory, is supported by the U.S. DOE under award DE-AC02-06CH11357. This work made use of the Center of Materials Science and Engineering at MIT which is supported by the NSF under award DMR-08-19762, and the Center for Nanoscale Systems at Harvard University which is supported by NSF under award ECS-0335765.

Contents

List of Figures

Chapter 1

Introduction

Rapid deployment of solar photovoltaic (PV) systems in the range of 1-10 TW by 2030 is deemed necessary to meet global climate change mitigation targets.[1–3] Although PV installation has seen unprecedented growth rates in recent years, the global cumulative installed PV capacity is still only 0.18 TW as of 2014.[4] In order to scale to multi-TW levels, both the capital intensity and cost of PV modules must be reduced drastically.[5]

Over the past decade, there has been significant progress in thin-film PV technology because of its cost advantage over silicon-based PV, which makes up 90% of the PV market today.[4] Thin-film PV offers reduced materials usage (about 1% of that used in Si-based PV) and compatibility with in-line manufacturing processes, lowering raw material costs and capital intensity. In particular, commercial chalcogenide-based thin-films such as copper indium gallium diselenide (CIGS) and cadmium telluride (CdTe) have recently achieved module costs below $0.60 per watt.[6] Unfortunately, CIGS and CdTe use elements that are not abundant in the earth's crust, and cumulative production capacity is limited to less than 1 TW by 2030.[7] In addition, the toxicity of Cd warrants mandatory recycling of CdTe PV modules as they are retired. In order to meet global PV deployment targets while taking advantage of the cost reductions afforded by thin-film PV, thin-film PV devices must be engineered to use earth-abundant, non-toxic materials.

1.1 Suitability of SnS for PV

SnS is a promising earth-abundant, non-toxic alternative to commercially available thin-film PV materials. An analysis of elemental abundance and scalability of PV absorber materials may be found in Hartman,[8] and the results show that both Sn and S fall well within the Earth-abundance range necessary for scaling to terawatt-level PV deployment. In addition, SnS is a non-toxic material, making it suitable for safe manufacturing at scale. There are also key material properties that make SnS suitable as a PV absorber, and the following section gives an overview of these properties.

1.1.1 Binary phase and congruent evaporation

SnS shows promise in terms of manufacturability. SnS is a binary material, unlike other earth-abundant alternatives such as copper zinc tin sulfide (CZTS). Ternary and quaternary compounds tend to have a large number of binary and ternary phases. These phases, when present in the processed solar cell even in small amounts, can be detrimental to efficiency, since they may possess sub-optimal bandgaps, carrier mobilities, and carrier concentrations.[9] In contrast, the Sn-S phase diagram, displayed in Figure 1-1, shows only three phases below 600°C: SnS, SnS_2, and Sn_2S_3,[10] allowing a relatively large process window for manufacturing SnS.

Furthermore, SnS is highly conducive to sublimation-type deposition systems that are already being used by First Solar, the manufacturer of CdTe-based PV that boasts the lowest levelized cost of electricity of the PV market as of this writing.[6] First, the relatively high vapor pressure of SnS[11–17] allows for low processing temperatures (< 600°C) when depositing via sublimation. Secondly, experiments to determine the vapor composition have shown that the dominant sublimation reaction for SnS is that of congruent evaporation:[11,18]

$$SnS(s) \rightarrow SnS(g).$$

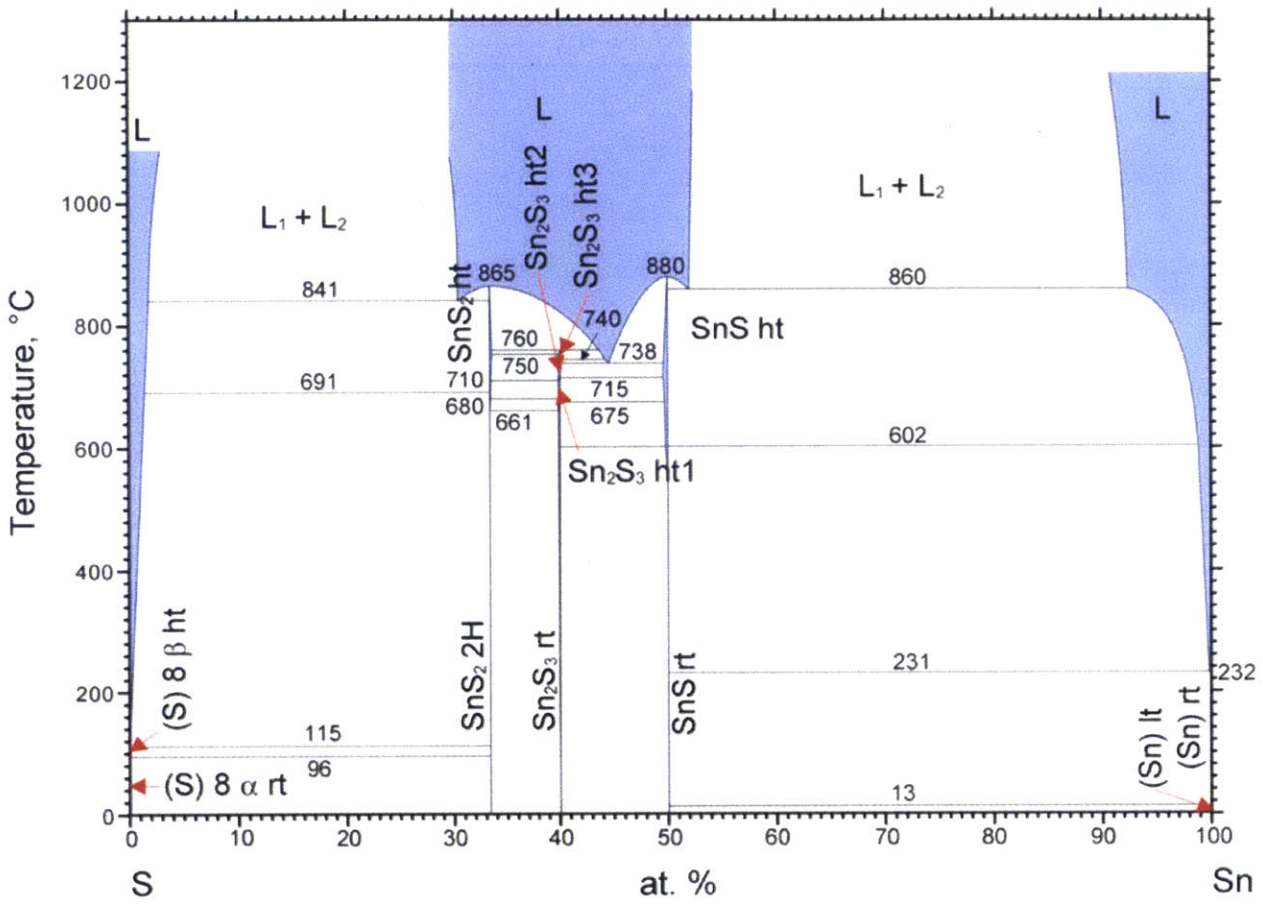

Figure 1-1. Binary phase diagram of the Sn-S system, showing only three phases below 600°C: SnS, SnS_2, and Sn_2S_3. Reproduced after Sharma *et al.*[10]

That is, instead of dissociating into the Sn and S in the vapor phase, the SnS remains as a molecule, thus maintaining stoichiometry during sublimation. The experimental vapor pressure of SnS(g) over SnS(s) from the literature is shown in Figure 1-2. The vapor pressure is also estimated by the author using measured deposition rates and the Langmuir equation,[19] and this is plotted in Figure 1-2 for a coefficient of evaporation of $\alpha_e = 1$ (blue). The agreement between the measured data and the literature equilibrium vapor pressure values demonstrates that the sublimated species in the thermal evaporation system used in this work is congruently evaporated SnS(g). The systematic difference between the measured data and literature values suggests that $\alpha_e < 1$, and an excellent fit to the literature values is found for $\alpha_e = 0.34$ (red in Figure 1-2), consistent with the range observed for other binary compounds.[20]

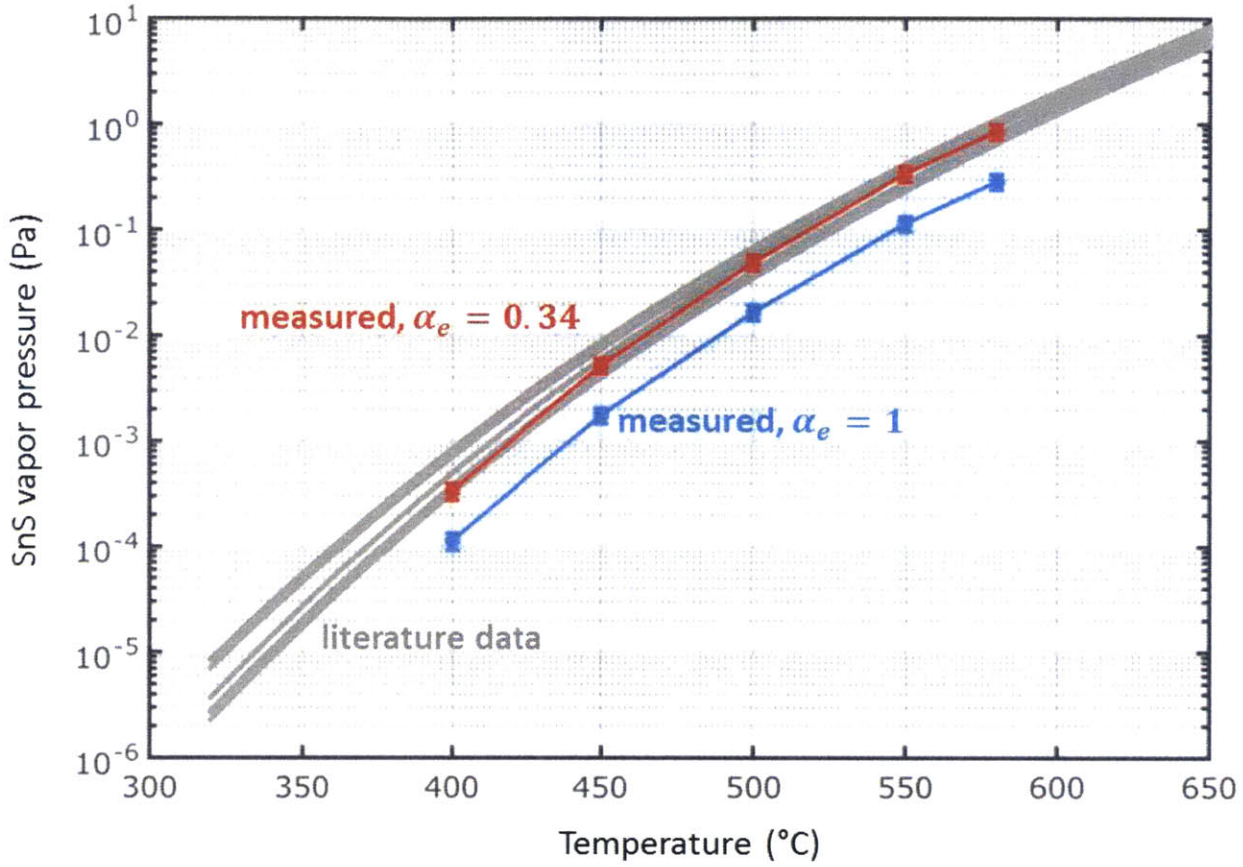

Figure 1-2. Equilibrium vapor pressure versus temperature. The gray lines are fits of the experimental vapor pressure of SnS(g) over SnS(s) from the literature.[11–17] Symbols and associated lines indicate vapor pressure estimates based on deposition rates measured by the author and the Langmuir equation. The blue and red symbols show the vapor pressure estimated using a coefficient of evaporation of 1 and 0.34, respectively. This data has been previously published in Steinmann *et al.*[21]

1.1.2 Anisotropic crystal structure

As shown by the phase diagram in Figure 1-1, SnS has several polymorphs, but there is only one stable phase at or near room temperature ("SnS rt" in Figure 1-1), commonly known as α-SnS. The α-SnS phase, characterized by Wiedemeier and Schnering on single crystals,[22] has a distorted rock salt structure belonging to the space group *Pnma* within the orthorhombic crystal system. The axes of the unit cell at room temperature are a = 11.200 Å, b = 3.987 Å, and c = 4.334 Å. Figure 1-3 shows a three-dimensional view of the orthorhombic crystal structure of α-SnS, revealing that it has a layered crystal structure, with slabs each two atoms thick. The unit cell contains two slabs, where the slabs are

perpendicular to the a axis. It is important to note that the intra-layer Sn-S bonds are relatively short and strong, while the inter-layer bonds exhibit a weak van der Waals character.[23] As this thesis concerns only the α-SnS phase, I shall refer to α-SnS as simply SnS for the remainder of this work.

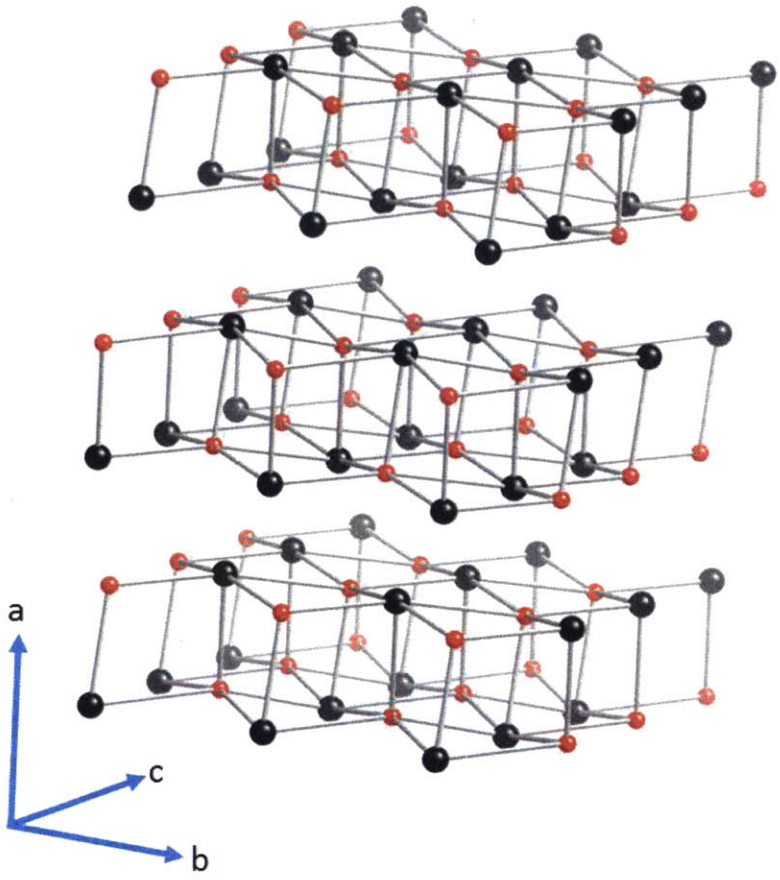

Figure 1-3. The orthorhombic crystal structure of SnS, with Sn atoms in black and S atoms in red. Bonds between layers (along axis a) are omitted for clarity. Reproduced after Hartman.[8]

The layered structure of SnS gives rise to anisotropic material properties, including carrier mobility,[24] surface energy,[25] and ionization potential.[25] Although this anisotropy may be viewed as a drawback in terms of adding complexity to the device engineering process, there are several potential benefits that leverage the anisotropy of SnS. First, the van der Waals-bonded surfaces of SnS crystals are intrinsically passivated, since they do not have any dangling bonds. This opens up the possibility of forming heterojunction interfaces that are nearly free of interface states.[26] Secondly, the anisotropic electronic transport properties may be harnessed to enable superior transport relative to more isotropic crystal

structures. In the case of SnS, the carrier mobility has been measured to be 5-10 times greater along the *b*-*c* plane than along the *a*-axis.[24,27] Thus, if the SnS layer in a device is engineered such that the high-mobility planes are oriented along the desired direction of electronic transport, the boost in mobility can potentially enhance the carrier collection properties relative to a similarly processed isotropic material. Indeed, there is an extensive literature dating back to the 1970s on using layered semiconductor materials for photovoltaics and photoelectrochemistry, motivated by these benefits. For a review of this literature, I refer the reader to the collection edited by Aruchamy.[28]

1.1.3 Bandgap and absorption coefficient

SnS also has a well-suited bandgap and absorption coefficient for use as a solar absorber material. Theoretical calculations suggest that the fundamental bandgap of SnS is indirect in the range 0.9–1.3 eV, with higher direct transitions in the range 1.5–2.1 eV.[29–31] Although most experimental investigations agree with these results qualitatively, with evidence of both the indirect and direct transitions, the measured values vary widely. For single crystals, the indirect bandgap has been measured to be 1.1–1.2 eV,[24,32,33] with a higher direct transition at 1.5 eV.[33] For thin-films, the measured indirect bandgaps fall in the range 0.9–1.2 eV,[34,35] and the direct bandgaps fall in the range 1.2–2.0 eV.[36–42] The wide variation in measured bandgaps might be due to differences in microstructure and strain in the films that result from different processing conditions. However, the fundamental indirect gap of 1.1 eV as calculated by the most recent theoretical study[30] corresponds to a near-optimal bandgap with respect to the Shockley Queisser detailed balance limit for a single-junction solar cell.[43] Figure 1-4 shows the maximum theoretical efficiency as a function of bandgap using the detailed balance analysis for the AM1.5 solar irradiance, highlighting the range 1.1–1.3 eV corresponding to the most recently calculated and measured bandgaps of SnS.[27,30] The bandgap of SnS falls near the maximum of this curve, with a theoretical maximum efficiency of 32–34%.

The direct bandgap of SnS enables a relatively high absorption coefficient, which is shown in Figure 1-5 for a film representative of the ones studied in this thesis. The absorption coefficient exceeds 10^4 cm^{-1} at the direct transition of 1.3 eV, and increases further for

higher photon energies. The high absorption coefficient enables more than 90% of above-bandgap light to be absorbed within only 1200 nm of material, making SnS amenable to a thin-film photovoltaic device architecture.[21]

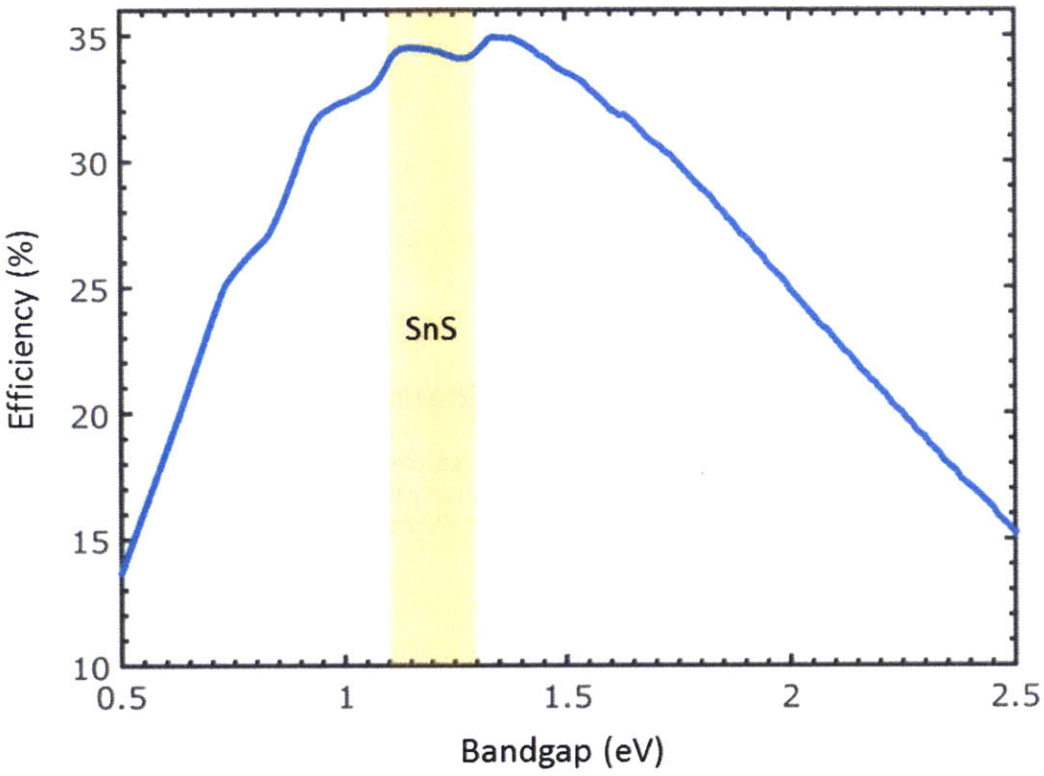

Figure 1-4. The blue curve shows the maximum theoretical efficiency as a function of bandgap, as calculated using detailed-balance analysis of Shockley and Queisser[43] with the AM1.5 solar irradiance.[44] The shaded region indicates the bandgap range bounded by the indirect (1.1 eV) and direct (1.3 eV) bandgaps of SnS.

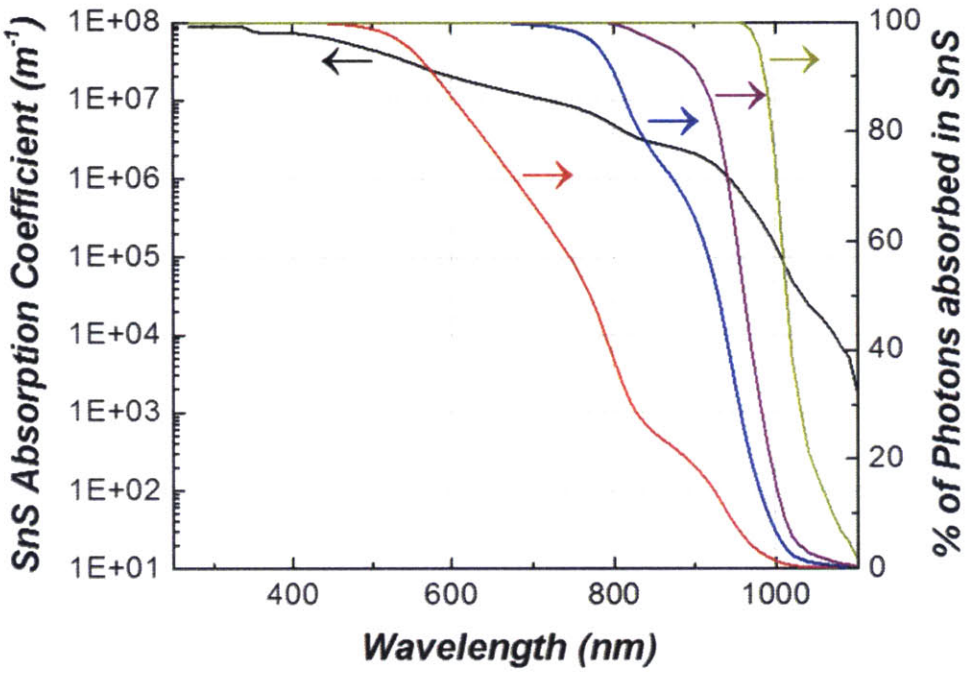

Figure 1-5. Left axis: Absorption coefficient of SnS versus wavelength. Right axis: Colored curves show the percent of photons absorbed in the SnS bulk for varying SnS layer thicknesses: 10 μm (dark yellow), 1200 nm (purple), 500 nm (blue), and 100 nm (red). Reproduced after Steinmann *et al.*[21]

1.2 Previous research on SnS

The near-optimal bandgap, high absorption coefficient, and manufacturability of SnS combined with its Earth-abundance and non-toxicity thus make SnS a strong candidate material for meeting global PV deployment targets in the coming decades. However, despite the advantages of SnS, the record efficiency for a SnS-based photovoltaic device is only 4.4%, paling in comparison to its theoretical maximum efficiency of 32%. The following sections review the literature on SnS thin-film growth and SnS PV device fabrication and assess the probable causes of the underperformance of SnS devices.

1.2.1 Thin-film growth of SnS

In order to gain insight into the requirements for achieving control over phase purity, morphology, and electronic properties of SnS, the breadth of SnS deposition techniques explored in the literature is first reviewed. The majority of the literature on SnS thin-film growth use chemistry-assisted deposition techniques. These depositions rely on one or more chemical species which are necessary during growth, but are not present in the final

thin-film. Within this broad category, SnS has been grown using several variants of chemical bath deposition,[45–49] electrochemical deposition,[34,50,51] chemical vapor deposition,[52–55] atomic layer deposition,[27,56] and spray pyrolysis.[57–59] Although phase-pure SnS can be achieved with these techniques, they are often hindered by slow growth rates and device-incompatible film morphologies. SnS has also been synthesized via sulfurization of a Sn film,[40,60] but phase purity is achieved only in a narrow process window of substrate temperature and sulfur partial pressure.

The most promising route for SnS synthesis seems to be physical vapor deposition. In this category, SnS has been deposited using RF sputtering,[61,62] close-space vapor transport,[63] vacuum thermal evaporation,[21,37,38,64–66] and hot-wall deposition.[67] Of these, the techniques that rely on thermal evaporation of a single source of SnS feedstock material are particularly attractive for several reasons. First, since SnS congruently evaporates,[11] there exists a large process window of substrate temperature and deposition rate in which phase-pure films are readily achieved, assuming that the source material is initially phase-pure.[68] In addition, thermal evaporation limits contamination of the film by extrinsic impurities since the process is typically done in vacuum and does not require extrinsic chemical species, most of which have as-yet unknown effects on the electrical properties of the film. Lastly, thermal evaporation is capable of rapid, industrially relevant growth rates approaching 1 μm/hr.[69] This means that research-scale learnings can more easily be translated into industrial processes in the future.

1.2.2 Solar cells based on SnS

A subset of the SnS literature also reports the fabrication of functional photovoltaic devices. There are numerous accounts of SnS devices; this section focuses on the few that have pushed the record experimental efficiency of SnS solar cells over time.

The first solid-state SnS-based device was reported by Noguchi *et al.* in 1994,[37] achieving a conversion efficiency of 0.29% with a thermally evaporated *p*-type SnS layer and an *n*-type CdS buffer layer. The reported cell had a short-circuit current (J_{SC}) of 7 mA/cm^2, an open-circuit voltage (V_{OC}) of 0.12 V, and a fill factor (FF) of 35%. More than a decade after, the next major improvement in SnS device efficiency was made by Reddy *et al.* in 2006,[42]

achieving a conversion efficiency of 1.3%. The device stack consisted of a spray pyrolyzed *p*-type SnS layer with an *n*-type indium-doped CdS window layer. The main improvements were in the V_{OC} (0.26 V) and FF (53%). However, J_{SC} remained low at 9.6 mA/cm^2. Given that this report was the first SnS device that involved annealing the SnS layer, it is possible that the improvement in device performance was due to a lowering of structural defect density in the SnS layer, but this is not directly measured in the work.

In 2013, Sinsermsuksakul *et al.* achieved a SnS device efficiency of 2.04%, with significant improvement in J_{SC} (19.4 mA/cm^2).[70] The main contribution of this work was the optimization of the conduction band offset between the SnS and the *n*-type buffer layer (zinc oxysulfide). Despite the optimized buffer layer, the V_{OC} remained low at 0.244 V.

Lastly, in 2014, the current record SnS device efficiency of 4.4% was reported by Sinsermsuksakul *et al.* again with a similar device stack.[71] A combination of annealing the SnS layer, depositing a thin oxide layer between the SnS and buffer layer, and optimizing the conduction band offset resulted in a significant improvement in V_{OC} (0.372 V) and smaller improvements in J_{SC} (20.2 mA/cm^2) and FF (58%). The thin oxide layer is thought to passivate the SnS/Zn(O,S):N interface, reducing surface recombination.

1.3 Possible causes of the low efficiency of SnS solar cells

Figure 1-6 shows the measured current-voltage curve and external quantum efficiency of the highest-efficiency NREL-certified thermally-evaporated SnS solar cell to date, which was developed and fabricated with contribution from the author.[21] The device stack in this case is identical to that used in Sinsermsuksakul *et al.*,[71] except that the SnS layer is thermally evaporated instead of deposited by atomic layer deposition. The efficiency of the NREL-certified solar cell is 3.88%, with a J_{SC} of 20.6 mA/cm^2, V_{OC} of 0.334 V, and FF of 56%. These device parameters are comparable to the result of Sinsermsuksakul *et al.*,[71], and they provide a worthy starting point for identifying the efficiency-limiting mechanisms at play in state-of-the-art SnS-based devices.

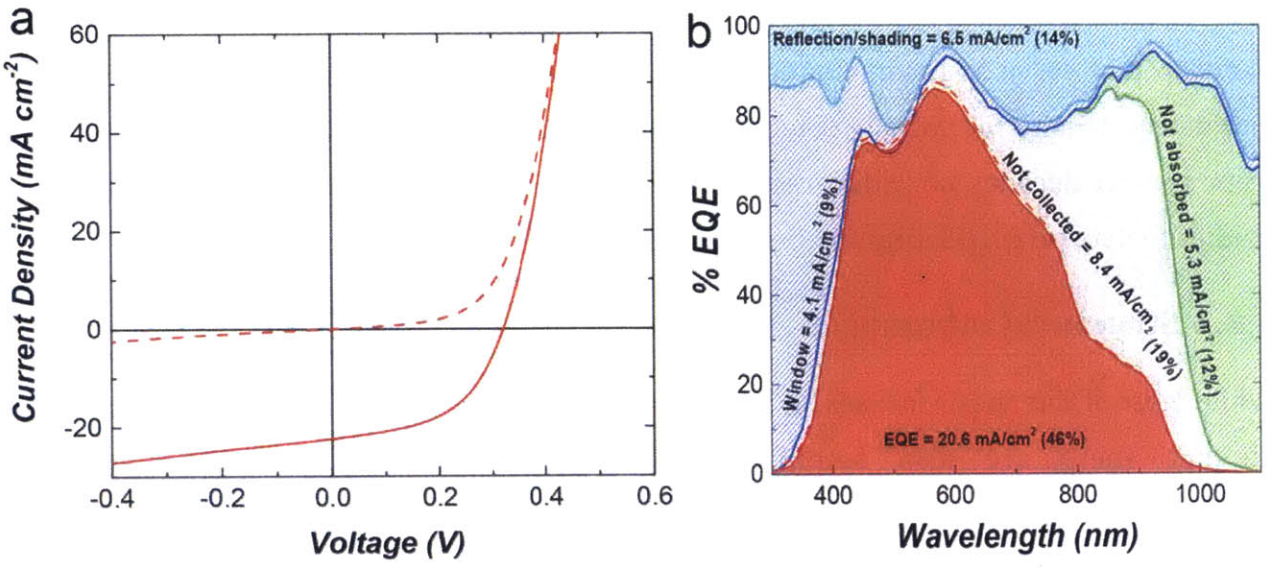

Figure 1-6. (a) Current-voltage curve for the current champion thermally evaporated SnS device, which has an NREL-certified efficiency of 3.88%. (b) The external quantum efficiency of the same device, along with a breakdown of current loss mechanisms. The largest current loss mechanism is the 19% of incident photons that are absorbed in the SnS layer but not collected as current due to recombination. The figure is reproduced after Steinmann *et. al.*[21]

1.3.1 Low minority-carrier lifetime

Figure 1-6 shows that both the current and voltage are lacking in the champion device. With regards to the current, the external quantum efficiency shows that the largest fraction of current loss is due to carriers that are absorbed by the SnS but recombine before collection. This is indicative of a low minority-carrier lifetime (MCL) in the SnS. Recent measurements of the MCL in the best thermally evaporated SnS devices indicate minority-carrier lifetimes in the range 10-70 ps.[72] These lifetimes are significantly lower than the ~1 ns lifetimes measured in CdTe and CIGS devices with efficiencies >10%, suggesting that MCL may be a severely limiting factor in current SnS devices.[72] Indeed, recent optoelectronic simulations suggest that SnS device efficiencies greater than 10% cannot be achieved without significant improvement of the bulk minority-carrier lifetime.[73] Moreover, a low minority-carrier lifetime would explain not only the loss in current, but also the majority of the loss in voltage.[73]

Thus, one of the main goals of present-day SnS research is to determine what recombination-active defects limit the MCL of SnS thin-films. Crystallographic defects, whether they are grain boundaries, stacking faults, dislocations, or extrinsic impurities,

perturb the periodicity of the crystal lattice, which may form discrete energy levels in the bandgap that serve as recombination traps for carriers.[74] The relationship between MCL and defect density for various defect types is well-documented for silicon, which benefits from several decades of widespread research.[75–78] However, for SnS, there are no such studies to date on correlating any type of defect density to MCL.

1.3.2 Structural inhomogeneity

While most of this thesis focuses on structural defects as they relate to the minority-carrier lifetime, there are also secondary efficiency loss mechanisms related to the inhomogeneous, polycrystalline nature of SnS films. In other chalcogenide polycrystalline thin-film absorbers such as CIGS and CZTS, inhomogeneities in the electrical characteristics at the thin film surface contribute significantly to V_{OC} loss in devices.[79,80] While the specific types of inhomogeneities that limit CIGS and CZTS, such as stoichiometric composition, may be less apparent in SnS thin films due to its binary character, the anisotropic material properties of SnS (discussed in Section 1.1.2) may contribute to a similar inhomogeneity-based efficiency loss. For example, a typical SnS thin film is made up of tens of millions of crystallites, or grains,[†] and each of these may have a different crystal orientation, and thus a different set of electronic properties at its surface. Thus, the structural inhomogeneity incurred by the polycrystallinity of SnS thin films, combined with its anisotropic properties, may give rise to secondary efficiency loss mechanisms other than a low MCL.

1.4 This thesis

The path toward high-efficiency SnS PV devices demands an understanding of the relationship between process parameters, material properties, and device performance. This thesis assesses the impact of structural defects on SnS device performance especially as it pertains to the minority-carrier lifetime and inhomogeneity-based losses, and explores the ability to control structural defects through growth engineering. The work is organized as follows. Chapter 2 gives a basic introduction to the key physical principles relevant to the work. Chapter 3 seeks to determine the effect of growth temperature on minority-

[†] For an average through-thickness grain area of 1 μm × 1 μm over a total device area of 1 cm^2.

carrier collection. Chapter 4 seeks to determine the relation between structural defects and minority-carrier collection through correlative microscopy. Chapter 5 explores the role of anisotropy in device performance, as well the potential to harness anisotropy for future device engineering efforts. Chapter 6 focuses on a specialized tool that may be used to expedite the process of structural defect engineering in SnS thin films.

Chapter 2

Theory: Structural defects in thin-film solar absorber materials

This chapter gives an overview of the fundamental physical principles involved at the core of this work, covering the basic principles of a solar cell, an introduction to defects and structural defect formation in thin films, and the electrical impact of these defects in a solar absorber material.

2.1 Brief introduction to solar cells

A comprehensive review of solar cell physics and operation is given in Würfel.[81] This section touches on only the concepts at the core of this thesis. At the most basic level, a solar cell transforms solar radiation into electrical energy by producing a current and voltage. The solar radiation is absorbed by a semiconductor material, generating electrons and holes, and these electrons and holes are steered toward electrical contacts at the boundaries of the solar cell, generating a current through an external circuit. Figure 2-1 depicts the energy band diagram of a heterojunction solar cell without an electric field, consisting of an absorber layer sandwiched by thinner *n*-type and *p*-type layers. In general, the absorber layer may have a *p*-type, *n*-type, or intrinsic character. For the purpose of explanation, let us assume that the absorber layer is *p*-type, and let us define the "*p-n*

junction" as the heterojunction between the *p*-type absorber layer and the contacting *n*-type layer at the right in Figure 2-1. In general, the electron affinities and bandgaps of the absorber layer and the *n*-type layer may be different, resulting in a discontinuity of the conduction band at the *p*-*n* junction. The magnitude of this discontinuity is called the conduction band offset.

In order to produce electrical power, the solar cell must support a current of the minority electrons toward the *n*-type layer across the *p*-*n* junction, while maintaining the quasi-Fermi level separation between the front and back contacts. Three critical processes are necessary for this to happen, denoted by the numbered red arrows in Figure 2-1. In the first process (1), incident light promotes electrons to the conduction band of the absorber layer. This process is governed by the absorption coefficient of the absorber layer. The electron must subsequently travel to the *p*-*n* junction (2), and then across the junction to

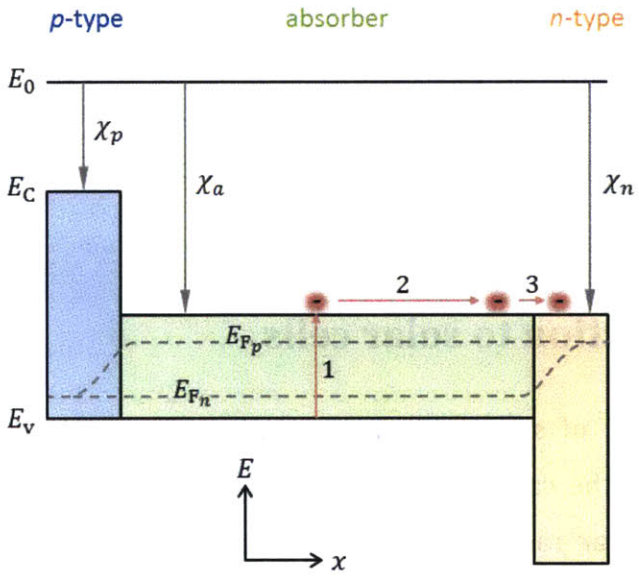

Figure 2-1. Energy band diagram of a solar cell with no internal electric field, consisting of an electron-blocking *p*-type layer (blue) with electron affinity χ_p, an absorber layer (green) with electron affinity χ_a, and a hole-blocking *n*-type layer (orange) with electron affinity χ_n. The conduction and valence band positions are denoted by E_c and E_v, and the electron and hole Fermi levels E_{F_n} and E_{F_p} are shown by the dotted gray lines. The three numbered red arrows denote three critical steps for extracting an electron from the solar cell: promotion to the conduction band via photoexcitation (1); transport to the absorber-*n*-type interface (2); and transport across the absorber-*n*-type interface (3). Figure adapted from Würfel.[81]

the *n*-type layer (3). This thesis focuses on two key parameters that determine the efficiency of processes 2 and 3: the minority-carrier diffusion length and the conduction band offset.

2.1.1 Importance of the diffusion length

The minority-carrier diffusion length L_{diff} is the length scale over which minority carriers travel before recombining and is given by

$$L_{\text{diff}} = \sqrt{D\tau} = \sqrt{\mu \frac{kT}{q} \tau}, \tag{2.1}$$

where D is the diffusivity of minority carriers, τ is the minority-carrier lifetime, μ is the minority-carrier mobility, q is the elementary charge, k is the Boltzmann constant, and T is temperature. Here we have also used the Einstein relation $D = \mu \frac{kT}{q}$. In the absence of drift, only the minority carriers generated within a diffusion length of the *p*-*n* junction have a high probability of being collected by the *p*-*n* junction and thus contribute to the current of the solar cell. A longer minority-carrier diffusion length translates to a longer distance over which a photogenerated carrier travels before recombining, resulting in more photogenerated carriers in the bulk of the semiconductor reaching the *p*-*n* junction of the solar cell. Under simplifying assumptions for a *p*-*n* junction,[82] the minority-carrier diffusion length is directly proportional to the short-circuit current of the solar cell:

$$J_{\text{SC}} \propto L_{\text{diff}}. \tag{2.2}$$

Thus, we see from Equations 2.1 and 2.2 that increasing the mobility-lifetime product, $\mu\tau$, is critical to increasing diffusion length, and thus the generated current of the solar cell.

2.1.2 Importance of the conduction band offset

The conduction band offset at heterojunction is given by the difference between the electron affinities of the *p*-type absorber and the *n*-type contact layer,

$$\Delta E_c = \chi_n - \chi_p. \tag{2.3}$$

The magnitude and sign of ΔE_c can have a profound impact on the device efficiency. Scheer and Schock[83] give a thorough discussion of the impact of ΔE_c on the short-circuit current density J_{sc}, the open-circuit voltage V_{OC}, and the fill factor FF for a heterojunction solar cell. The key concept is that there can be a tradeoff between V_{OC} and J_{SC} as ΔE_c is varied. A large negative value of ΔE_c creates a cliff-type conduction band offset, causing electrons to lose energy as they cross the heterojunction, thus limiting the V_{OC}. On the other hand, a large positive value of ΔE_c creates a spike-type conduction band offset, and electron current across the heterojunction via thermionic emission is impeded because of the large energetic barrier, thus limiting the J_{SC}. Depending on the interface recombination velocity at the heterojunction, an optimum conduction band offset exists for which the efficiency is maximized.[83]

2.2 Structural defects and their impact on devices

2.2.1 Structural defects in crystalline solids

In general, a crystallographic structural defect is *any* perturbation of the periodicity of the crystal lattice. Crystallographic defects may be conveniently classified by their dimensionality.[84] At the lowest dimension, there are point defects such as vacancies, interstitials, and substitutionals. Line defects are one-dimensional defects localized to a space curve within the crystal, such as dislocations. Finally, two-dimensional planar defects are perturbations of the crystal along an entire plane, including free surfaces, hetero-interfaces, grain boundaries, twin boundaries, and stacking faults. In this work, one- and two-dimensional crystallographic defects are referred to as extended structural defects. A further distinction is made between intrinsic and extrinsic defects: intrinsic defects refer to defects that only involve the atoms of the host crystal lattice, while extrinsic defects refer to those that involve atoms other than those of the host crystal lattice.

2.2.2 Impact of structural defects on minority-carrier lifetime

When the periodicity of the crystal lattice is perturbed by any type of these structural defects, extra electronic states beyond those of the perfect crystal lattice are created. In general, these electronic states have discrete, localized energy levels that may be within the valence band, the conduction band, or the bandgap of the material. A defect whose energy levels lies within the bandgap is known as a recombination trap, as it enhances electron-hole recombination in its vicinity when the state is unoccupied.[74] The statistics of recombination through a localized point defect is well-described by the Shockley-Read-Hall (SRH) model,[85,86] in which the time constant for electron capture τ_{n_0} is inversely proportional to the density of defects N, the capture cross-section of the defect σ_n, and the thermal velocity of electrons v_{th}:

$$\tau_{n_0} = \frac{1}{N\sigma_n v_{th}}. \tag{2.4}$$

The important feature of Equation 2.4 is that the time constant is strongly affected by the density of defects N: the greater the density of defects, the lower the time constant. The time constant for electron capture, along with its analogous counterpart for holes, are in turn directly proportional to the carrier lifetime due to SRH recombination, τ_{SRH}. More sophisticated models similarly capture the relation between the density of line and surface defects to their corresponding effective lifetimes τ_{line} and τ_{surface}, respectively.[87–89] The qualitative trend that a higher defect density leads to a lower lifetime still holds in these models. In general, the total effective minority-carrier lifetime is the harmonic sum of minority-carrier lifetimes governed by each recombination mechanism in the material.[81] Thus, we may define the effective lifetime due to all types of structural defects τ_d as the harmonic sum

$$\frac{1}{\tau_{\text{d}}} = \frac{1}{\tau_{\text{SRH}}} + \frac{1}{\tau_{\text{line}}} + \frac{1}{\tau_{\text{surface}}} + \cdots . \tag{2.5}$$

The total effective lifetime τ_{eff} of the material also includes but is not limited to the radiative lifetime τ_{rad} and Auger lifetime τ_{Auger} such that[81]

$$\frac{1}{\tau_{\text{eff}}} = \frac{1}{\tau_{\text{rad}}} + \frac{1}{\tau_{\text{d}}} + \frac{1}{\tau_{\text{Auger}}} + \cdots \quad . \tag{2.6}$$

Thus, the density of structural defects has a direct impact on the effective minority-carrier lifetime, which has a direct impact on device performance through the diffusion length per Equation 2.1. The structural defect density in a solar cell absorber material should thus be minimized to maximize the minority-carrier lifetime.

2.3 Structural defect formation during thin-film growth *via* thermal evaporation

2.3.1 Thermal evaporation

In this work, solid SnS source material is thermally evaporated in a high vacuum to deposit a thin-film of SnS onto a substrate. The basic equation governing the rate of evaporation from a liquid or solid source is given by[19,90]

$$\phi_e = \frac{\alpha_e N_A (P_e(T) - P_h)}{(2\pi MRT)^{1/2}} \tag{2.7}$$

where ϕ_e is the evaporation flux in number of atoms or molecules per unit area per unit time, α_e is the coefficient of evaporation, N_A is Avogadro's constant, $P_e(T)$ is the temperature-dependent equilibrium vapor pressure of the source, P_h is the ambient pressure on the source, M is the molar mass of the source, R is the ideal gas constant, and T is the temperature of the source. The key variable here that influences the evaporation flux is the source temperature, since it has a significant impact on the vapor pressure P_e.

As mentioned previously, SnS has the convenient property of congruent evaporation,[11] which allows us to treat the evaporation of SnS as the single-species evaporative process described by Equation 2.7.

2.3.2 Thin-film growth

Ohring gives an in-depth review of thin film growth from both a thermodynamic and kinetic perspective.[90] Here the concepts most relevant to this thesis are reviewed, starting with ad-atom kinetics, and ending with the structure-zone models.

As evaporated ad-atoms come close to the substrate, they may adsorb onto the substrate surface.[90] The bonded ad-atoms then diffuse over the substrate surface until they either desorb or get trapped at a low-energy lattice site. The surface diffusion process may be modeled in terms of the ad-atom surface diffusion distance $\delta_{ad} = \sqrt{D_{SD}\tau_{ad}}$, where $D_{SD} = D_0 \exp\left(-\frac{\Delta g_{SD}}{kT_{sub}}\right)$ is the ad-atom surface diffusivity, and τ_{ad} is the average time before the ad-atom either desorbs from the surface or arrives at the site of another ad-atom. Here the surface diffusivity is $D_{SD} = D_0 \exp\left(-\frac{\Delta g_{SD}}{kT_{sub}}\right)$, where Δg_{SD} is the energetic barrier of site-to-site migration of ad-atoms, k is the Boltzmann constant, and T_{sub} is the substrate temperature. In the case that τ_{ad} is limited by the interaction with other ad-atoms instead of desorption, the diffusion distance may be expressed as[91]

$$\delta_{ad} = \frac{N_0^{1/2} D_0^{1/2} \exp\left(-\frac{\Delta g_{SD}}{2kT_{sub}}\right)}{F_{dep}^{1/2}}. \tag{2.8}$$

In Equation 2.8, N_0 is the number of surface sites per unit area of substrate, and F_{dep} is the flux of ad-atoms at the surface in number of atoms per unit area per unit time, such that $\tau_{ad} = N_0/F_{dep}$. There are several points to note about Equation 2.8. First, the diffusion distance is strongly influenced by the substrate temperature T_{sub} through the exponential in the numerator. As temperature increases, the ad-atom diffusion distance increases. Second, the diffusion distance is inversely affected by the ad-atom flux F_{dep}. As the ad-atom flux increases, the ad-atom diffusion distance decreases. Lastly, the substrate-film interaction encapsulated by Δg_{SD} also has a strong effect on δ_{ad} through the exponential; a substrate that interacts weakly with the film will have a low Δg_{SD}, resulting in a long ad-atom diffusion distance.

As the ad-atoms interact with one another on the substrate, they begin to form clusters, or nucleate. While inherently a kinetic process, the qualitative features of nucleation can be described from a thermodynamic perspective. Thermodynamically, the way in which a nucleus forms and grows is determined by three interfacial surface energies: the surface energy of the film-vacuum interface γ_{fv}, the surface energy of substrate-vacuum interface γ_{sv}, and the surface energy of the film-substrate interface γ_{fs}. In the case that $\gamma_{sv} \geq \gamma_{fs} +$

γ_{fv}, the film tends to eliminate the substrate-vacuum interface, thus "wetting" the substrate in layers. This mode of growth is called Frank - van der Merwe growth and is typically required for epitaxial growth. More commonly, $\gamma_{sv} < \gamma_{fs} + \gamma_{fv}$, and the film tends to form islands, since the substrate-vacuum interface is energetically more favorable. This mode of growth is called Volmer-Weber island growth, and typically leads to polycrystalline films such as the SnS films observed in this work.

In the case of Volmer-Weber island growth under conditions not limited by desorption of ad-atoms, the nucleation rate $\dot{N}$, in nuclei per unit area per unit time, is given by[90]

$$\dot{N} \propto F_{dep} \exp\left(-\frac{\Delta g_{n^*}}{kT_{sub}}\right) \tag{2.9}$$

where Δg_{n^*} is the energy of formation (< 0) of a cluster of ad-atoms of critical size n^*. Note that the nucleation density increases with increasing deposition flux and decreasing substrate temperature. The nuclei grow until they eventually impinge on one another, creating a continuous polycrystalline film. The average grain size at impingement is proportional to δ_{ad} and $1/\dot{N}^{1/3}$.[92] Thus, the grain size at impingement increases with increasing δ_{ad} and decreasing $\dot{N}$. After impingement, the film grows in the vertical direction away from the substrate, and the kinetic parameters change such that the ad-atom diffusion distance and nucleation rate are redefined for an ad-atom on the film itself instead of on the substrate.

The eventual microstructure of the film is thus determined by a complex interplay between surface energetics of the film and substrate, growth parameters such as the substrate temperature and deposition flux, and the time over which the growth occurs. Predicting the microstructure of a thin-film in this multidimensional parameter space is thus a difficult task. However, the simple ad-atom diffusion and nucleation models discussed above show that the microstructure should be extremely sensitive to the growth temperature. Indeed, the strong dependence on growth temperature is observed for evaporated metal films in the literature, and empirical "structure-zone models" have been developed to capture the qualitative influence of growth temperature on evaporated thin films.[93,94] These models typically express the growth temperature in terms of the homologous temperature, defined

as the ratio of the growth temperature to the melting temperature of the film. As the homologous temperature increases, the microstructure generally changes from a small-grained, high-defect-density film to a large-grained, low-defect-density film.

Chapter 3

Effect of growth temperature on minority-carrier collection‡

As explained in Section 2.3, the defect density found in a thin film can be very sensitive to the growth temperature, as growth temperature is one of the key parameters in determining the ad-atom diffusion length during film growth. Indeed, for other thermally evaporated thin-film solar cell materials such as cadmium telluride and copper (indium, gallium) (diselenide, disulfide), the growth temperature T_g is a critical process parameter affecting charge-carrier collection in devices.[95,96] Although the effect of T_g on crystalline texture, grain size, electrical transport properties, and optical properties of SnS thin films has been studied extensively,[36,38,97–99] its effect on charge-carrier collection has not yet been directly measured through a working SnS photovoltaic device.

In this chapter, I determine the effect of growth temperature T_g on the structural and electrical properties of thermally evaporated SnS films. The internal quantum efficiency (IQE) of devices is measured using a previously developed device stack.[21] IQE probes the collection efficiency due to drift and diffusion, allowing us to analyze the transport properties of SnS under different processing conditions. By increasing the SnS growth

‡ The contents of this chapter are adapted from a previously published journal article in *Applied Physics Letters*,[100] the publisher of which, American Institute of Physics, has granted permission for authors to re-publish in a thesis.

temperature from 150 to 285°C, the long-wavelength carrier collection traverses through a local minimum, a behavior attributed to the combined effects of a varying SnS majority-carrier concentration and minority-carrier diffusion length. A monotonic increase in carrier concentration with increasing growth temperature leads to decreasing drift-assisted carrier collection. This causes a decrease in total collection up to the highest growth temperature of 285°C. Despite the decrease in drift-assisted collection at 285°C, the total long-wavelength carrier collection recovers due to an improvement in minority-carrier diffusion length. This suggests that the films grown at the highest temperature have a lower density of lifetime-limiting bulk defects.

Most of the content of this chapter has been previously published in Applied Physics Letters.[100] My main contributions to this work are the experimental design, growth of SnS films, the majority of the film characterization, device simulation, and device analysis. The post-growth annealing, AFM measurements, spectrophotometry, and device fabrication are performed by my co-authors.

3.1 Materials and Methods

3.1.1 Growth of films and fabrication of devices

The SnS thin films are grown via thermal evaporation on $Si/SiO_2/Mo$ substrates at four substrate temperatures: 150, 200, 240, and 285°C. The deposition rate is held at 1–2 Å/s. Substrate temperatures higher than 285°C result in re-evaporation of SnS from the substrate due to the low deposition rate and large source-to-substrate distance (10 cm) in our thermal evaporation system. All films are subsequently annealed at 400°C in 4% H_2S atmosphere (N_2 balance) at 28 Torr for 60 minutes to promote grain growth. Re-evaporation is strongly suppressed during annealing, because the high total pressure limits re-evaporation. The post-annealed film thicknesses range from 886-1204 nm due to differences in surface topology and error in deposition rate measurement. Devices are fabricated with each annealed film using a previously reported procedure.[68] The device stack includes a thin SnO_2 layer on the SnS surface and a Zn(O,S):N *n*-type buffer layer. Each sample contains 11 devices defined by a shadow-masked ITO pattern. Further details on

the preparation of SnS powder, preparation of $Si/SiO_2/Mo$ substrates, thermal evaporation and annealing parameters, and device fabrication steps are described in prior work.[68]

3.1.2 Film characterization

Scanning electron micrographs are taken using a Zeiss Ultra-55 scanning electron microscope (SEM), with a working distance of 4 mm and an accelerating voltage of 5 kV. Visible grain boundaries in each plan-view SEM (one for each growth temperature) are manually traced using the raster graphics editor GIMP.[101] Each trace is processed using the "Analyze Particles" feature of the image analysis software ImageJ[102] to produce a list of in-plane grain areas A_i in units of pixel^2. Grain areas are converted to μm^2 using the scale bar on each SEM with systematic error ± 0.04 μm^2. The number of traced grains is $n > 120$ for each growth temperature. Using the simplifying assumption of circular grains, Figure 3-1 plots the distribution of grain diameters $d_i = 2(A_i/\pi)^{1/2}$ for each growth temperature.

The SnS film thicknesses on $Si/SiO_2/Mo$ are measured by cross-sectional SEM.

Atomic force microscopy (AFM) measurements are carried out using an Asylum MFP-3D instrument in tapping mode and Olympus AC160-TS probes. The roughness is calculated from images with a 10 x 10 um^2 field of view.

Hall effect measurements are carried out in the Van der Pauw configuration on SnS sister samples grown on Si/SiO_2 wafers.

The texture of SnS films on $Si/SiO_2/Mo$ substrates were analyzed by X-ray diffraction (XRD) on a Rigaku SmartLab with Cu $K\alpha$ radiation in Bragg-Brentano configuration in the 2θ range 20-60°.

External quantum efficiency measurements are performed with a PV Measurements Model QEX7 at room temperature without light or voltage bias. Internal quantum efficiency is calculated by $\text{IQE} = \frac{\text{EQE}}{1-R}$, where R is the reflectivity of the device stack as measured by a Perkins Elmer Lambda 950 spectrophotometer.

3.1.3 Determination of physical parameters used in optoelectronic model

The material parameter values listed in Table 3-1 define our numerical model. In addition to SnS hole concentration, which is measured directly for the current sample set, four additional parameters vary with growth temperature: SnS hole mobility, electron mobility, SnS dielectric constant, and SnS/Zn(O,S):N conduction band offset. The upper and lower bounds in Table 3-1 for these additional parameters represent the expected variation across growth temperatures (see below for discussion of individual parameters). The remaining properties are held constant across growth temperatures, and the upper and lower bounds denote experimental uncertainties.

The following sections clarify the origin of the constants in Table 3-1 that are not directly measured or taken from the literature.

3.1.3.1 SnS dielectric constant

The dielectric constant in SnS is known to be significantly anisotropic as measured on single crystals.[109] For the purpose of the simulation, we are interested in the dielectric constant in the direction of carrier transport, which is perpendicular to the substrate (out-of-plane). For any particular grain in a polycrystalline film, the dielectric constant in the out-of-plane direction depends on the particular orientation of that grain. The effective out-of-plane dielectric constant for the here-studied polycrystalline films is estimated by taking a weighted average of the orientation-dependent dielectric constant based on the grain orientation distribution as measured by X-ray diffraction (XRD).

XRD is taken on each post-annealed sample in Bragg-Brentano configuration in the range 20-60°2θ. Within this range, at least 13 peaks corresponding to orthorhombic SnS (ICDD 00-039-0354) are identified for each sample. The degree of preferred orientation is

Material parameter	Best estimate	Lower bound	Upper bound	Source
SnS thickness	1000 nm	-	-	SEM cross-section
SnS bandgap	1.1 eV	-	-	[30]
SnS dielectric constant	T_g-dependent: see Table 3-2.	37	43	[103], XRD for anisotropic correction
SnS $h^+(e^-)$ mobility	T_g-dependent: see Figure 3-2c.	20 (32) $cm^2/V{\cdot}s$	40 (115) $cm^2/V{\cdot}s$	Hall effect (m_h^*/m_e^* from [30])
SnS h^+ carrier density	T_g-dependent: see Figure 3-2a.	See Figure 3-2a, lower error bar.	See Figure 3-2a, upper error bar.	Hall effect
SnS optical absorption coefficient	Measured for $T_g = 240°C$.	-	-	[21]
SnS $h^+(e^-)$ effective mass	0.68 (0.28) m_0	-	-	[30]
SnS valence (conduction) band density of states	3.6e18 (1.4e19) cm^{-3}			from effective mass
SnS/Zn(O,S):N conduction band offset ($\chi_{SnS} - \chi_{ZnOS}$)	T_g-dependent: see Table 3-3.	-0.53	-0.33	[30,73], XRD for anisotropic correction
SnS/Zn(O,S):N interface recombination velocity	1e4 cm/s	0 cm/s	1e5 cm/s	[73]
Zn(O,S):N thickness	30 nm	-	-	[21]
Zn(O,S):N e^- carrier density	5.3e13 cm^{-3}	2.4e13 cm^{-3}	2.4e14 cm^{-3}	[73]
Zn(O,S):N, ZnO dielectric constant	9	-	-	[104]
Zn(O,S):N, ZnO $h^+(e^-)$ effective mass	2.0 (0.19) m_0	-	-	[105]
Zn(O,S):N, ZnO valence (conduction) band density of states	7.0e19 (2.0e18) cm^{-3}	-	-	from effective mass
ZnO thickness	10 nm	-	-	[21]
ZnO e^- carrier density	1e19 cm^{-3}	-	-	[106,107]
ZnO electron affinity	4.28 eV	-	-	[108]
ITO, ZnO, Zn(O,S):N bandgaps	> 2.5 eV	-	-	[73]

Table 3-1. Material parameter values for device layers assumed in electronic simulations. Note that the best estimates for SnS dielectric constant, hole and electron mobility, hole carrier density, and SnS/Zn(O,S):N conduction band offset vary with growth temperature; for these parameters, the upper and lower bounds represent the range of values expected across growth temperatures. All other material parameters are assumed to be constant with growth temperature; for these parameters, the upper and lower bounds represent uncertainty in the literature value. Values for the Zn(O,S):N carrier concentration are from measurements performed in the dark.

computed using the fiber texture method,[110] in which the volume fraction f_{hkl} of crystals oriented with (h k l) parallel to the substrate is determined by

$$f_{hkl} = \frac{I_{hkl}/I'_{hkl}}{\sum I_{hkl}/I'_{hkl}}$$

where I_{hkl} is the measured peak intensity of the film, and I'_{hkl} is the reference peak intensity of a randomly oriented sample (ICDD 00-039-0354). It is assumed that the set of >13 measured peaks gives a representative distribution of grain orientations for the film.

Using Miller index notation, let $[h'\ k'\ l']$ be the unit normal vector to the set of planes $(h\ k\ l)$. The dielectric constant in the direction of the unit normal vector is given by[111]

$$\epsilon_{hkl} = h'^2\epsilon_{11} + k'^2\epsilon_{22} + l'^2\epsilon_{33}$$

where ϵ_{11}, ϵ_{22}, and ϵ_{33} are the diagonal elements of the dielectric constant tensor for SnS. These tensor components have been measured in the literature via spectroscopic ellipsometry on SnS single crystals, and range from 34.06 to 51.66.[109] Lastly, the effective out-of-plane dielectric constant is estimated as the weighted average

$$\epsilon_{\text{eff}} = \sum_{hkl} f_{hkl}\epsilon_{hkl}.$$

The computed values of ϵ_{eff} range from 37.9 – 42.1 and are listed in Table 3-2 for each growth temperature and are the values used in the optoelectronic model.

Growth temperature (°C)	150	200	240	285
ϵ_{eff}	39.7	41.3	42.1	37.9

Table 3-2. Computed values of ϵ_{eff} for each post-annealed sample based on the volume fractions of grain orientations measured by XRD.

3.1.3.2 SnS hole and electron mobility

The measured SnS Hall mobility is used as the SnS hole mobility in our simulations. Although the Hall mobility is measured in the plane of the thin film, it is not necessary to take anisotropy into account in the parameter regime defined by Table 3-1. In this parameter regime, the electron mobility μ_e does not affect the simulation separate from the electron lifetime τ_e, as only terms with $\mu_e\tau_e$ as a product are dominant.

The mobility for carriers of type i can be expressed as $\mu_i = q\tau_{c,i}/m_i^*$, where q is the electron charge, $\tau_{c,i}$ is the collision time, and m_i^* is the effective mass of carrier type i.[81] We assume equal collision times between holes and electrons and obtain the electron mobility

by multiplying the hole mobility by a factor m_h^*/m_e^*, where the effective masses are listed in Table 3-1.

3.1.3.3 Optical absorption

The long-wavelength optical absorption coefficient for a SnS film grown on glass at 240°C and similarly annealed has been measured and previously published.[21] This absorption coefficient is held constant as a function of growth temperature in the simulations.

3.1.3.4 Effective mass and density of states

SnS hole and electron effective masses m_h^* and m_e^* are taken by averaging the anisotropic effective masses calculated in the literature.[30] The valence and conduction band density of states are then calculated by

$N_V = 2\left(\frac{2\pi m_h^* k_B T}{h^2}\right)^{3/2}$ and $N_C = 2\left(\frac{2\pi m_e^* k_B T}{h^2}\right)^{3/2}$, respectively, where k_B is the Boltzmann constant, h is the Planck constant, and $T = 297$ K.

ZnO hole and electron effective masses are similarly taken by averaging anisotropic effective masses in the literature,[105] and the valence and conduction band density of states are calculated in the same way. The effective mass and density of states for ZnO are assumed to be equal to those of Zn(O,S):N.

3.1.3.5 SnS/Zn(O,S):N conduction band offset

The conduction band offset (CBO) at the SnS/Zn(O,S):N interface has been measured using combined X-ray photoelectron and optical absorption measurements.[73] This measurement was performed for a SnS film grown at 240°C and similarly annealed. Again the issue of anisotropy must be addressed. The SnS electron affinity is predicted to vary with $(h\ k\ l)$,[25] which means the band offset at the SnS/Zn(O,S):N interface may change with grain orientation. Therefore, as a check, an effective weighted-average SnS electron affinity is calculated as is done for the dielectric constant, based on the volume fractions of orientations measured by XRD for each sample. For this calculation, the electron affinity for each crystal surface of SnS is taken from the literature.[25] The implied SnS/Zn(O,S):N CBO is then computed by using the measured value for the sample grown at 240°C as a reference,

assuming that the Zn(O,S):N electron affinity is constant. Table 3-3 shows the computed values of SnS electron affinity and implied SnS/Zn(O,S):N conduction band offset for each sample.

Growth temperature (°C)	150	200	240	285
χ_{SnS} (eV)	4.12	4.21	4.16	4.01
$\chi_{SnS} - \chi_{ZnOS}$ (eV)	-0.42	-0.33	-0.38*	-0.53

Table 3-3. Computed values of SnS electron affinity for each post-annealed sample based on the volume fractions of grain orientations measured by XRD. The conduction band offset is calculated using the measured value (denoted by the asterisk) as a reference.

3.1.3.6 Zn(O,S):N conduction band offset

The electron carrier density in our Zn(O,S):N layer has been measured using the Hall effect.[73]

3.1.3.7 SnS/Zn(O,S):N interface recombination velocity

The recombination velocity at the SnS/Zn(O,S):N interface has not been measured, but more comprehensive fitting of device data including current-voltage data has been done in prior work.[73] From this work, the best-estimate, upper bound, and lower bound values given in Table 3-1 for interface recombination velocity are obtained.

3.1.4 Analytic depletion width calculation

Depletion width is estimated using the analytic form for an absorber/buffer/window system with a fully depleted buffer, derived elsewhere.[83] The material parameters used for this calculation are the best-estimate values listed in Table 3-1.

3.1.5 Optoelectronic model implementation and fitting

The opto-electronic model used in this work is implemented in SCAPS-1D.[112]

In general, there may be differences between the measured SnS hole mobility (via Hall effect on Si/SiO_2 substrates) and the SnS hole mobility for films grown on Mo which are used for devices. For this reason, the IQE analysis of this work does not use the measured carrier mobility on Si/SiO_2 substrates as an input. Rather, the diffusion length $L_{diff} =$

$\sqrt{\frac{kT}{q}\mu_e\tau_n}$ is used as the effective fitting parameter, and within the explored parameter space, the minority-carrier mobility μ_e and minority-carrier lifetime τ_n affect $J_{\mathrm{IQE,lw}}$ equivalently. Thus, μ_e is not used as an input to the simulations; rather, it is wrapped into the effective fitting parameter.

In practice, SCAPS-1D does not allow direct control of L_{diff}; instead, the minority-carrier lifetime τ_n is used as the fitting parameter in practice. The minority-carrier lifetime τ_n is set by Shockley-Read-Hall recombination with a single, neutral mid-gap defect level.[85,86] The lifetime τ_n is varied during fitting by varying the total defect density. The fitted diffusion length is then $L_{\mathrm{diff}} = \sqrt{\frac{kT}{q}\mu_e\tau_n}$, where μ_e is the electron mobility described in Table 3-1. Since only the fitted diffusion length $L_{\mathrm{diff}} = \sqrt{\frac{kT}{q}\mu_e\tau_n}$ is reported, the results are independent of the exact mechanism by which τ_n is controlled.

3.1.6 Overlaying experimental data with simulated data

The best-estimate values for $T_{\mathrm{g}} = 240°\mathrm{C}$ are used to compute the contour plot in Figure 3-11. The salient features of the contour plot do not change by using the best-estimate values for other growth temperatures, so the experimental data points for each growth temperature are overlayed based on the measured carrier concentrations and fitted diffusion lengths.

3.1.7 Two-dimensional modeling of carrier collection for surface-roughness dependence

3.1.7.1 Computing carrier collection

Topology data from AFM line scans are used to create a quantitatively accurate device cross-section. The device cross-section is fed into a finite-difference time-domain optical absorption simulation, resulting in a 2D normalized generation profile $G_n(x, y, \lambda)$ through the thickness of the device. Here, $G_n(x, y, \lambda)$ is normalized to the incident photon flux used in the simulation such that $\iint G_n(x, y, \lambda)\, dx\, dy = 1$. The computed 2D normalized

generation profile is then converted to a 1D normalized generation profile $G_n(w',\lambda)$ as a function of distance to the nearest junction w', such that $\int G_n(w',\lambda)\, dw' = 1$. To estimate the magnitude of the differences in $J_{\mathrm{IQE,lw}}$ due to surface topology, $G_n(w',\lambda)$ is integrated for long wavelengths up to a collection depth w to obtain a collection-depth-dependent current density

$$J_{\mathrm{IQE,lw}}(w) = \int_0^w \int_{700\ \mathrm{nm}}^{950\ \mathrm{nm}} G(w',\lambda)\, \phi_{AM1.5}(\lambda)\, \frac{\lambda}{hc}\, d\lambda\, dw'.$$

3.1.7.2 Finite-difference time-domain (FDTD) optical absorption modeling

Finite-difference time-domain (FDTD) optical absorption modeling is done by randomly choosing 5 scan lines out of the 256x256 point (10x10 μm^2) SnS texture obtained using AFM. For each of these scan lines, the texture of the subsequent layers grown using ALD (30 nm Zn(O,S):N and 10 nm ZnO) is modeled by extending the SnS texture by 30 nm and 40 nm in the direction perpendicular to the SnS surface, while the texture of the sputtered ITO (250 nm thick) is modeled by growing the ZnO texture in the vertical direction. These texture models are combined with the refractive index data of the material layers to construct the full FDTD model (Lumerical FDTD Solutions package). Afterwards, a 2-dimensional FDTD simulation is performed on each model (fixed mesh sizes of 5 nm in the horizontal direction and 2 nm in the vertical direction, electric field distribution $E(x,y)$ is recorded for wavelength range λ = 700–950 nm with wavelength step $\Delta\lambda$ of 10 nm), allowing us to calculate the spectrally-resolved generation profile $G(x,y,\lambda)$ for each of the 5 randomly chosen scan lines, which are then used in the IQE fitting simulation.

3.2 Results and Discussion

3.2.1 Microstructure, electrical properties, and carrier collection

I first examine the impact of T_g on the structural properties of SnS thin films, summarized in Figure 3-1. The morphology of the SnS films are shown in the scanning electron micrographs in Figure 3-1a, which indicate a variation in packing density of grains. As T_g increases, intergranular voids decrease in size and frequency. Figure 3-1b shows a box plot

representing the distribution of in-plane grain diameters for each growth temperature. The median grain diameter increases monotonically with T_g, ranging from 191 nm at $T_g = 150°C$ to 383 nm at $T_g = 285°C$. The grain diameter distribution profile also changes as a function of T_g. As T_g increases, the midspread of grain diameters increases, accompanied by an increasingly positive skew in the distribution. For example, the upper quartile grain size for $T_g = 150°C$ is 269 nm, as compared to 616 nm for $T_g = 285°C$. All of these morphological trends are observed despite an identical 1-hr post-deposition anneal at 400°C for all samples. This suggests that the as-grown film morphology may kinetically limit the grain-growth during the subsequent anneal step.

The electrical properties of the SnS thin films, as measured by the Hall effect on SnS sister samples grown on Si/SiO_2 wafers, are shown in Figure 3-2. All films were *p*-type, and the hole concentration increased monotonically with T_g from 6.3×10^{15} to 3.1×10^{16} cm^{-3}. The

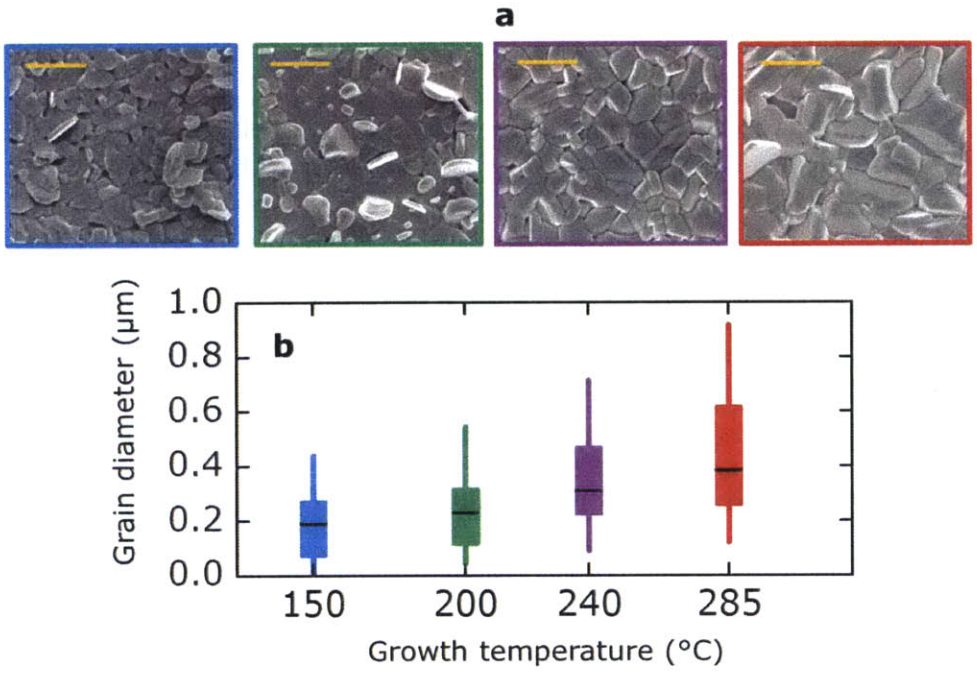

Figure 3-1. Experimental data on structural properties. (a) Plan-view SEM, showing increasing grain size with growth temperature (increasing temperature left to right: 150°C in blue, 200°C in green, 240°C in purple, 285°C in red). Scale bar indicates 1 μm. (b) Distribution of post-annealed grain diameters tending towards larger grains with increasing growth temperature. Black horizontal line indicates median; edges of box indicate 25th and 75th percentiles; whiskers indicate 5th and 95th percentiles.

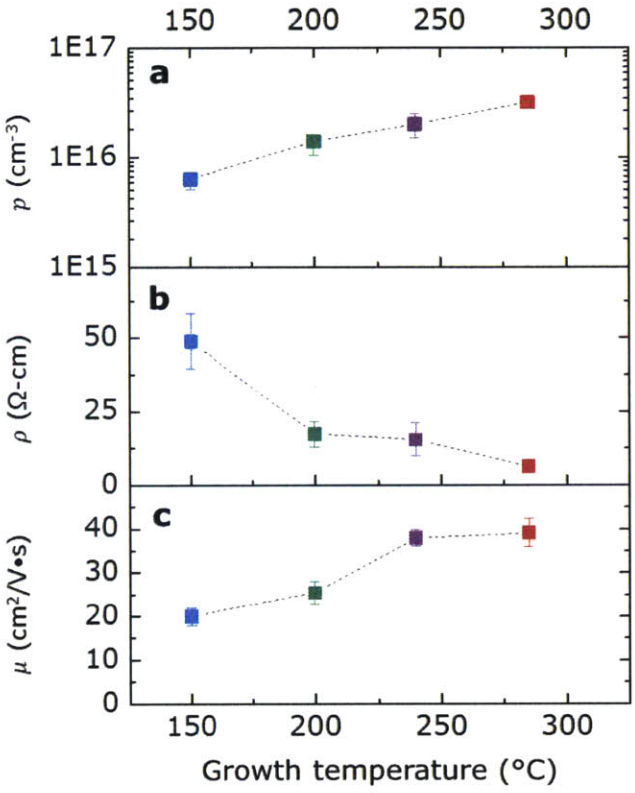

Figure 3-2. Experimental data on electrical properties. (a) Hall carrier concentration; (b) resistivity; and (c) Hall mobility. Both carrier concentration and mobility increase monotonically with growth temperature. Error bars indicate propagation of experimental uncertainty in thickness measurement by SEM and contact placement.

hole concentration is likely controlled by the concentration of doubly-ionized Sn vacancies, which are predicted to be shallow acceptors.[30] The film resistivity decreased from 49 to 6.3 Ω-cm. Hole mobility tended to increase with T_g, ranging from 20.1 to 31.6 $cm^2/V \cdot s$. The upward trend in grain size and mobility with T_g is consistent with decreasing grain boundary scattering,[113] but other intragranular scattering processes may also limit mobility. Notably, the dependence of electrical properties on T_g persist despite a post-deposition anneal at 400°C.

Figure 3-3 shows the average internal quantum efficiency (IQE) from all rectifying devices on each substrate. Below 450 nm, the IQE drops sharply due to optical absorption in the Zn(O,S):N and ITO layers.[21] In the wavelength range 450-700 nm, the IQE varies across growth temperatures. Although this short-wavelength region is sensitive to carrier collection within 100 nm from the SnS/Zn(O,S):N interface (as $\alpha > 10^5$ cm^{-1} for these

wavelengths), this region is also particularly sensitive to errors in the reflectivity measurement due to pronounced optical interference in the ITO and Zn(O,S):N layers. In contrast, the long-wavelength region 700-950 nm is more sensitive to changes in carrier collection throughout the bulk, because for these wavelengths the absorption coefficient α is as low as 10^4 cm^{-1} and film thicknesses are $\sim 10^{-4}$ cm. Moreover, interference fringes in the reflectivity spectrum due to the ITO and Zn(O,S):N layers are less pronounced for wavelengths beyond 700 nm. Thus, the analysis of carrier collection is restricted to the long-wavelength region 700-950 nm. In this region, an unexpected trend is observed: the magnitude of IQE varies non-monotonically with T_g. Figure 3-4a shows the integrated IQE in the long-wavelength range in terms of the current density

$$J_{\mathrm{IQE,lw}} = \int_{700\,\mathrm{nm}}^{950\,\mathrm{nm}} \mathrm{IQE}(\lambda)\, \phi_{\mathrm{AM1.5}}(\lambda)\, \frac{\lambda}{hc}\, d\lambda$$

where $\phi_{\mathrm{AM1.5}}(\lambda)$ is the AM1.5 spectral irradiance. As growth temperature increases, $J_{\mathrm{IQE,lw}}$ decreases from 8.4 mA/cm^2 at $T_g = 150$°C, to 6.3 mA/cm^2 at $T_g = 240$°C, and then increases back to 8.4 mA/cm^2 at the highest growth temperature of 285°C (Figure 3-4a).

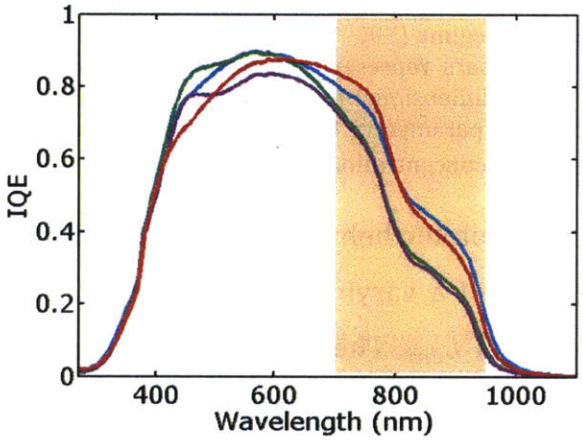

Figure 3-3. Measured internal quantum efficiency of SnS thin-film devices for the four growth temperatures (150°C in blue, 200°C in green, 240°C in purple, 285°C in red). The highlighted region indicates the wavelength range (700–950 nm) which is fitted using a one-dimensional opto-electronic model in SCAPS-1D.

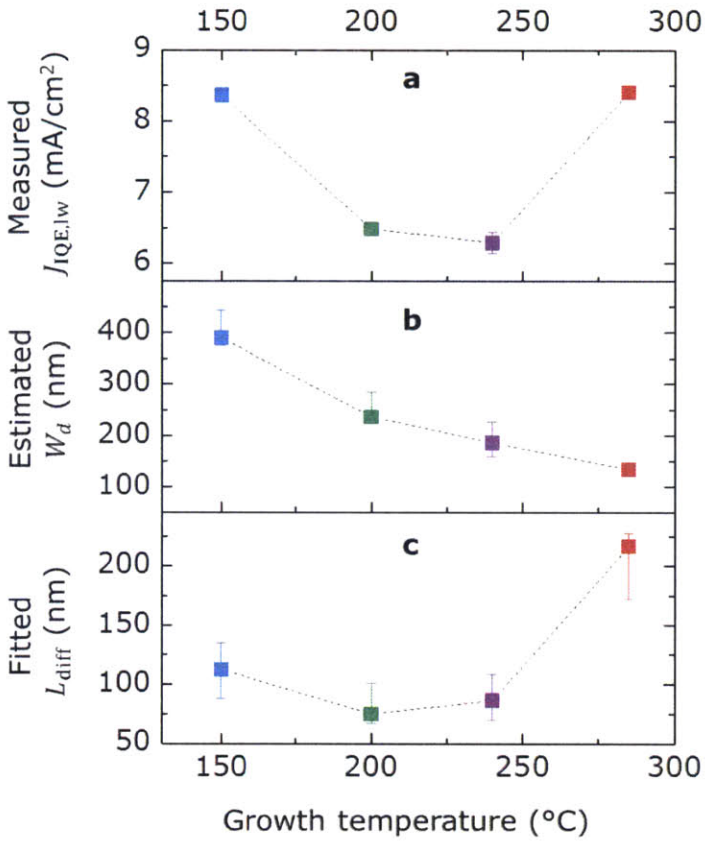

Figure 3-4. SnS thin-film device parameters as a function of growth temperature (150°C in blue, 200°C in green, 240°C in purple, 285°C in red). (a) Current density $J_{IQE,lw}$ extracted from experimental IQE by integrating over the long-wavelength regime (700–950 nm). (b) Estimated depletion width W_d based on the measured hole concentration. Error bars represent uncertainty in material parameter values. (c) Fitted diffusion length L_{diff} based on a one-dimensional opto-electronic model in SCAPS-1D. Error bars take into account both uncertainty in material parameters from the literature, as well as the effect of varying T_g-dependent parameters other than hole concentration.

I hypothesize that this non-monotonic behavior in long-wavelength IQE with temperature is due to the combined effects of a varying majority-carrier (hole) concentration p and minority-carrier diffusion length L_{diff}. The depletion width decreases with increasing p, reducing the distance over which the internal electric field assists collection of minority electrons from the SnS bulk. That is, a lower hole concentration should result in a larger photo-generated carrier collection because there is a higher minority-carrier drift current. Figure 3-4b shows the depletion widths computed using measured hole carrier concentrations and an analytic expression for heterojunctions.[83] The SnS film grown at the lowest temperature of 150°C has the lowest p (Figure 3-2a), the largest depletion width, and thus the most drift-assisted collection. As carrier concentration increases with T_g, a

decrease in drift-assisted collection is expected due to a shrinking depletion width. This trend in expected drift-assisted collection is consistent with the trend in $J_{\mathrm{IQE,lw}}$ for $T_g \leq$ 240°C. However, for the highest growth temperature of 285°C, $J_{\mathrm{IQE,lw}}$ recovers despite the relatively small depletion width. One possible mechanism for the relatively high $J_{\mathrm{IQE,lw}}$ at 285°C is by an enhancement of L_{diff}.

This hypothesis is verified by implementing a one-dimensional opto-electronic model and fitting to the experimental long-wavelength IQE (see Section 3.1.5 for details). The model demonstrates that the decreasing trend in $J_{\mathrm{IQE,lw}}$ for growth temperatures up to 240°C is caused by an increasing hole concentration, while the resurgence in $J_{\mathrm{IQE,lw}}$ at 285°C is driven by an increase in L_{diff}. As inputs to the simulation, material parameters extracted from experimental data on the here-studied samples are used in conjunction with literature values (see Section 3.1.3 for details). Within the defined parameter space, the minority-carrier mobility μ_e and minority-carrier lifetime τ_n affect $J_{\mathrm{IQE,lw}}$ equivalently. The simulated long-wavelength (700–950 nm) IQE is fit to experimental data by using the $\mu_e\tau_n$ product as the effective fitting parameter, and then extract the fitted diffusion length $L_{\mathrm{diff}} = \sqrt{\frac{kT}{q}\mu_e\tau_n}$ (see Section 3.1.5 for details).

The fitted diffusion lengths are shown by the filled squares in Figure 3-4c. The error bars in Figure 3-4c take into account both uncertainty in material parameters from the literature, as well as the effect of varying T_{g}-dependent parameters other than hole concentration. In particular, the fitted diffusion lengths use the best-estimate material parameter values from Table 3-1, and the error bars represent the upper and lower bounds for the fitted L_{diff} using all permutations of the upper and lower bounds from Table 3-1.

For the lowest growth temperature of 150°C, the fitted diffusion length ranges from 88–135 nm. Remarkably, the L_{diff} ranges for $T_{\mathrm{g}} = 200$°C and 240°C statistically overlap with the range for $T_{\mathrm{g}} = 150$°C, implying that the change in hole concentration alone is sufficient to explain the change in $J_{\mathrm{IQE,lw}}$ for growth temperatures up to 240°C. However, the fitted diffusion lengths for T_g =285°C range from 172–228 nm, well above the ranges for lower growth temperatures. Thus, even accounting for the variation of other parameters within

the bounds outlined in Table 3-1, the recovery in $J_{\mathrm{IQE,lw}}$ at $T_g = 285°C$ cannot be explained without an increase in L_{diff} of the films deposited at this temperature. However, there are several other factors that could contribute to the perceived increase in L_{diff}. In the following section, I examine the sensitivity of the analysis to these factors.

3.2.2 Sensitivity to other co-varying material parameters

3.2.2.1 SnS morphology on Si/SiO_2 substrates

The hole concentration measurements are performed on different substrates (Si/SiO_2) from those used for device measurements. As a check, I examine the possibility that the carrier concentration p on these substrates is different from the carrier concentration on the original substrates ($Si/SiO_2/Mo$).

Figure 3-5 shows plan-view SEMs of SnS grown on Si/SiO_2 substrates for each growth temperature. Similar to SnS grown on $Si/SiO_2/Mo$, SnS grown on Si/SiO_2 exhibits increasing grain size with growth temperature. However, in general, the absolute grain sizes and morphology of SnS films on Si/SiO_2 are not identical to those on $Si/SiO_2/Mo$.

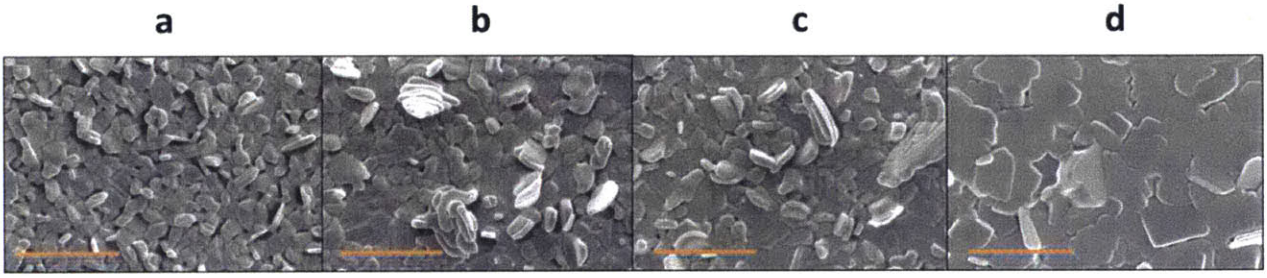

Figure 3-5. Scanning electron micrographs of post-annealed $Si/SiO_2/SnS$ for each growth temperatures. (a) 150°C; (b) 200°C; (c) 240°C; (b) 285°C. Scale bar indicates 1 μm.

Although the IQE analysis does not rely on the measured electron mobility μ_e, it does rely on the measured hole concentration p, which is also measured *via* the Hall effect on Si/SiO_2 substrates. However, the conclusion that L_{diff} increases at the highest growth temperature of 285°C depends on the *trend* in carrier concentration with growth temperature rather than the absolute values of carrier concentrations. Since a the trend in SnS film morphology on Si/SiO_2 substrates is similar to that on $Si/SiO_2/Mo$ substrates, a similar trend in hole concentration between the two substrates as a function of growth temperature is expected.

Thus, although this effect could result in quantitative differences in p and the fitted L_{diff}, the trends in p and L_{diff} as a function of T_g are likely unaffected.

3.2.2.2 SnS film thickness

Variation in thickness is also a factor not taken in account by the error bars in Figure 3-4c. Figure 3-6 shows the measured thickness of as-deposited and annealed SnS films for each growth temperature, with error bars representing the standard deviation of surface roughness as measured by atomic force microscopy (see Section 3.2.2.3). For each growth temperature, annealing does not change the film thickness to within error. Re-evaporation is strongly suppressed during annealing presumably because of the high total pressure (28 torr). The post-annealed film thicknesses range from 886-1204 nm due to differences in surface topology and error in deposition rate measurement.

Despite the slight variation in film thickness with growth temperature, all of the thicknesses are >5 times the fitted diffusion lengths. The thickness variation is thus expected to have a negligible influence on the carrier collection in the device.

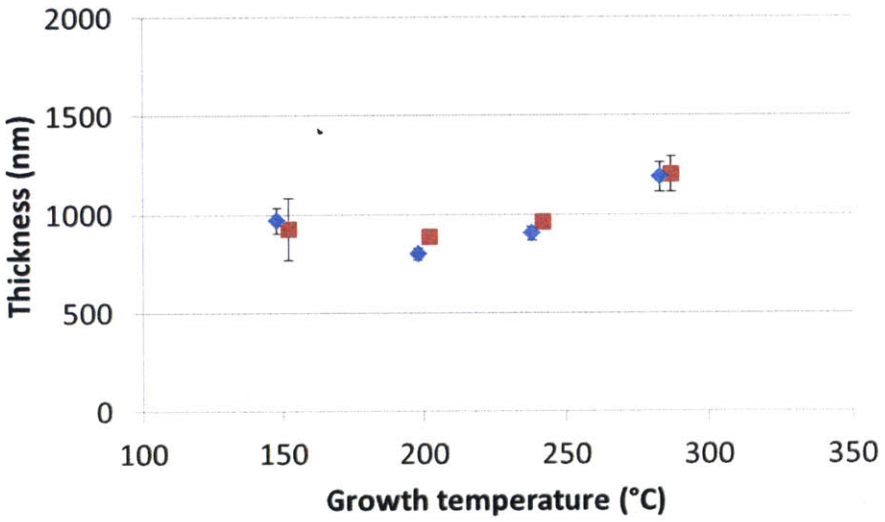

Figure 3-6. Data points indicate the SnS film thickness as measured by cross-sectional SEM of as-deposited (red squares) and annealed (blue diamonds) samples, respectively. The error bars represent the standard deviation of surface roughness as measured by AFM over one 2x2 μm^2 area on each sample (see Section 3.2.2.3).

3.2.2.3 Variation in surface roughness

As a check, I also consider the effects of a varying surface roughness on the long-wavelength current density $J_{\mathrm{IQE,lw}}$. As shown by the atomic force microscopy (AFM) scans in Figure 3-7, the structure of the SnS surface changes with growth temperature. Surface topology may affect carrier collection in that high-aspect-ratio surface structures tend to lower the average distance from the bulk to the junction. Note that this mechanism is different from surface roughness leading to decreased reflectance, of which IQE is independent. The root-mean-squared roughness for the post-annealed samples are shown in Figure 3-8. The trend in roughness roughly mirrors that of $J_{\mathrm{IQE,lw}}$; to rule this out as the main contributor to the trend in $J_{\mathrm{IQE,lw}}$, two-dimensional simulations are carried out to quantify the effect of surface topology on long-wavelength carrier collection. For these simulations, a collection-depth-dependent $J_{\mathrm{IQE,lw}}(w)$ is computed based on a two-dimensional optical simulation of quantitative device cross-sections (see Section 3.1.7).

The computed $J_{\mathrm{IQE,lw}}(w)$ for each growth temperature is plotted in Figure 3-9, along with a similarly computed $J_{\mathrm{IQE,lw}}(w)$ for the case of a planar surface. All AFM-based simulations show enhanced $J_{\mathrm{IQE,lw}}(w)$ relative to the planar case, indicating that the diffusion length may be systematically overestimated by assuming a planar surface. In addition, the range of $J_{\mathrm{IQE,lw}}(w)$ due to surface topology alone – that is, for a given collection depth w – may account for up to 35% of the differences in measured $J_{\mathrm{IQE,lw}}$ across samples. Although this effect is significant, a change in collection depth is still necessary to account for the majority of the variation in measured $J_{\mathrm{IQE,lw}}$.

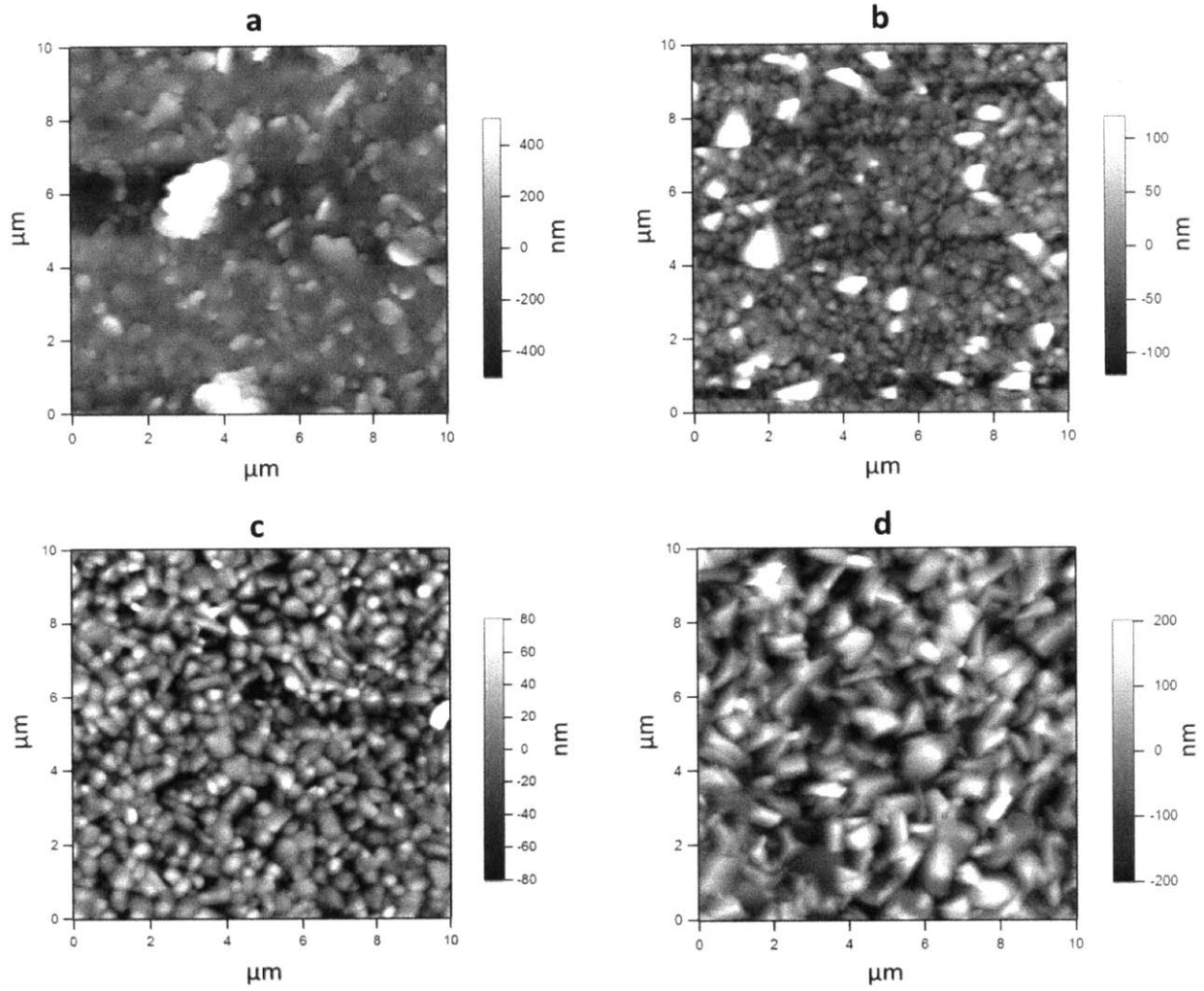

Figure 3-7. AFM scans of the post-annealed SnS films for each growth temperature. (a) 150°C; (b) 200°C; (c) 240°C; (b) 285°C. Note the changing surface morphology.

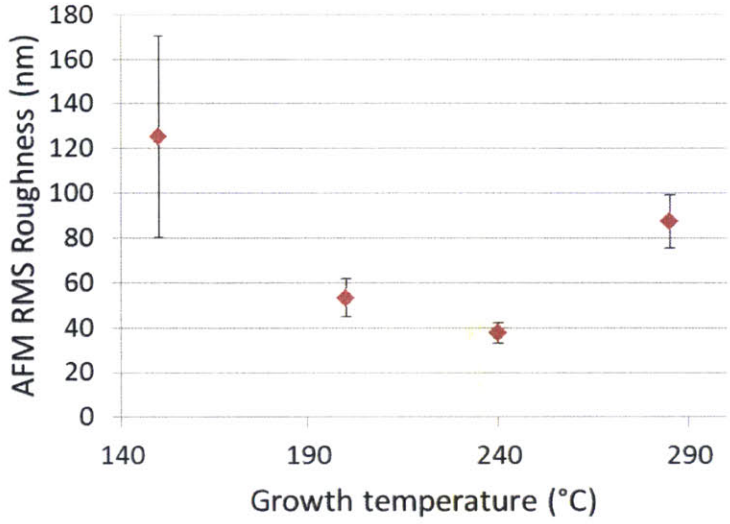

Figure 3-8. Root-mean-squared (RMS) surface roughness as measured by AFM for each post-annealed sample. Points and error bars represent the average and standard deviation of RMS roughness over 9 distinct 3x3 μm^2 areas on each sample, respectively.

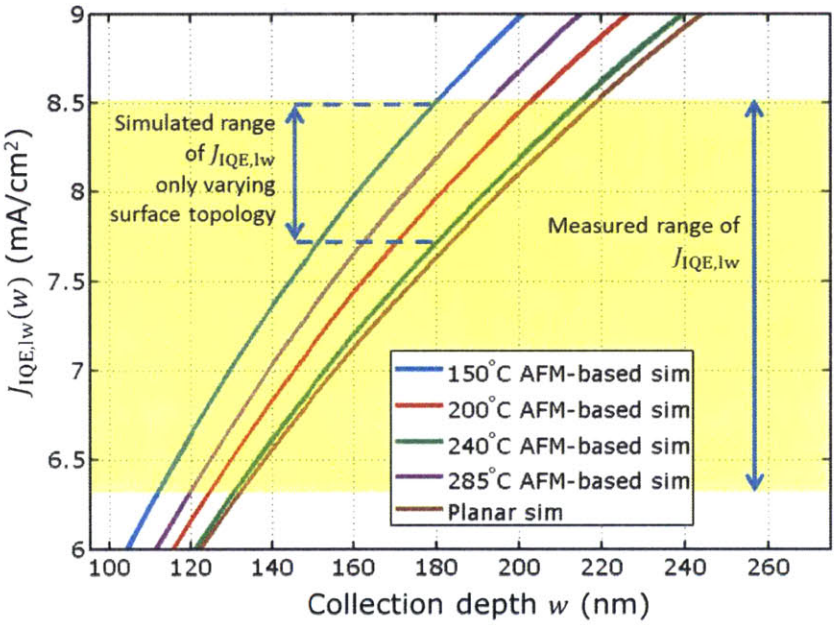

Figure 3-9. Collection-depth-dependent integrated IQE, simulated using a 2D optical model informed by AFM measurements for each post-annealed sample. The same simulation assuming a planar surface is also shown for comparison. All AFM-based simulations show enhanced $J_{IQE,lw}(w)$ relative to the planar case. However, the difference in $J_{IQE,lw}(w)$ across samples for a given collection depth w is not sufficient to account for the change in measured $J_{IQE,lw}$, which ranges from 6.3-8.5 mA/cm².

3.2.2.4 Variation in absorption due to anisotropy

The long-wavelength optical absorption coefficient is held constant as a function of growth temperature in the simulations. However, the absorption coefficient is anisotropic. Therefore, as a check, a calculation is done similar to that done for the anisotropic dielectric constant in Section 3.1.3.1, to obtain an effective weighted-average absorption coefficient based on the volume fractions of orientations measured by XRD for each sample. For this calculation, the anisotropic extinction coefficient is extracted from spectrally resolved anisotropic optical measurements from the literature.[109] For each growth temperature, the diffusion length is re-fit using the modified absorption coefficient calculated for that growth temperature, along with best-estimate values of other material parameters listed in Table 3-1. The results are shown in Figure 3-10; the two points for each growth temperature represent the limits of fitted L_{diff} obtained by varying the SnS carrier concentration between the lower and upper bounds defined in Table 3-1. Although the absolute value of L_{diff} decreases from that in Figure 3-4c, the trends still hold; an increase in diffusion length at $T_g = 285°C$ is still necessary to explain the long-wavelength IQE enhancement at that temperature.

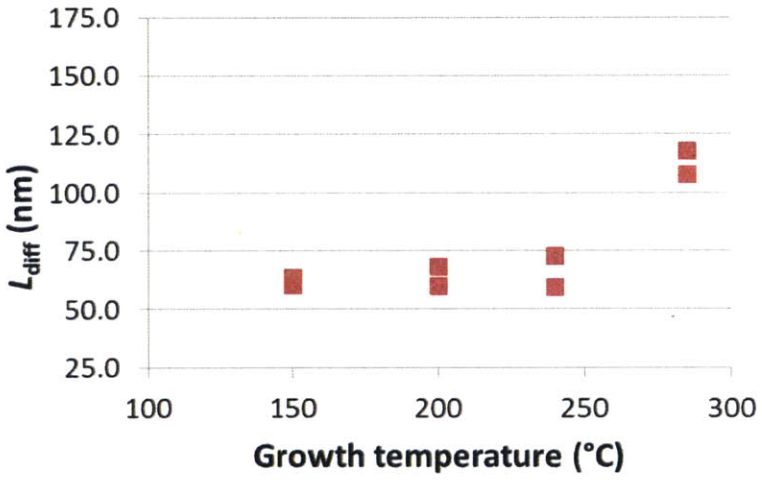

Figure 3-10. Re-fitted diffusion lengths using modified orientation-dependent absorption coefficient for each sample. The two points for each growth temperature indicate the limits of fitted diffusion length obtained by varying the SnS carrier concentration between the lower and upper bounds defined in Table 3-1. The trend of near-constant L_{diff} for $T_g < 285°C$ and an increase in L_{diff} still holds.

3.2.3 Causes of minority-carrier collection difference

Because the Hall mobility increases by only 2.9% from $T_g = 240°C$ to 285°C, the rise in L_{diff} at 285°C is likely driven by an enhancement of effective minority-carrier lifetime. Recalling that the grain size is highest for $T_g = 285°C$, a reduction in grain boundary recombination may contribute to the increase in L_{diff}.[114] However, grain size tends to increase monotonically with temperature, whereas the fitted L_{diff} stays nearly constant for $T_g < 285°C$. Thus, grain boundary recombination alone does not explain the trend in fitted L_{diff} . Instead, I suspect that a reduction of intragranular defect density is responsible for the enhancement of minority-carrier lifetime at $T_g = 285°C$.

In optimizing SnS bulk properties for maximum carrier collection, we would ideally benefit from both drift and diffusion. Figure 3-11 is a contour plot of simulated $J_{IQE,lw}$ for a range of SnS hole concentrations and diffusion lengths, with the results of the present study appropriately overlayed in the parameter space (see Section 3.1.6 for details). Here it is more easily seen how as T_g increases, we traverse through the parameter space in a way that produces lower $J_{IQE,lw}$ at the intermediate temperatures. Additionally, we should aim for both lower carrier concentrations (towards 10^{15} cm^{-3}) and higher diffusion lengths to achieve long-wavelength current densities approaching the theoretical maximum of $J_{IQE,lw} = 15.0$ mA/cm^2. It is also important to note a qualitative difference in the effect of hole concentration versus that of diffusion length on $J_{IQE,lw}$. Increasing L_{diff} increases both diffusive and drift collection and is especially effective at improving carrier collection. In contrast, decreasing p can only increase collection by enlarging the depletion region and has a more limited improvement capacity. As the carrier concentration is decreased, the loss in current due to the series resistance of SnS counteracts the benefit of drift-assisted collection. Consequently, for a given diffusion length, the net benefit of decreasing p diminishes as p is lowered. The author notes that while the IQE measurements focus exclusively on the short-circuit point, the SnS hole concentration also affects the open-circuit voltage and fill factor. The SnS hole concentration should thus be optimized not only for short-circuit carrier collection, but for overall device efficiency.

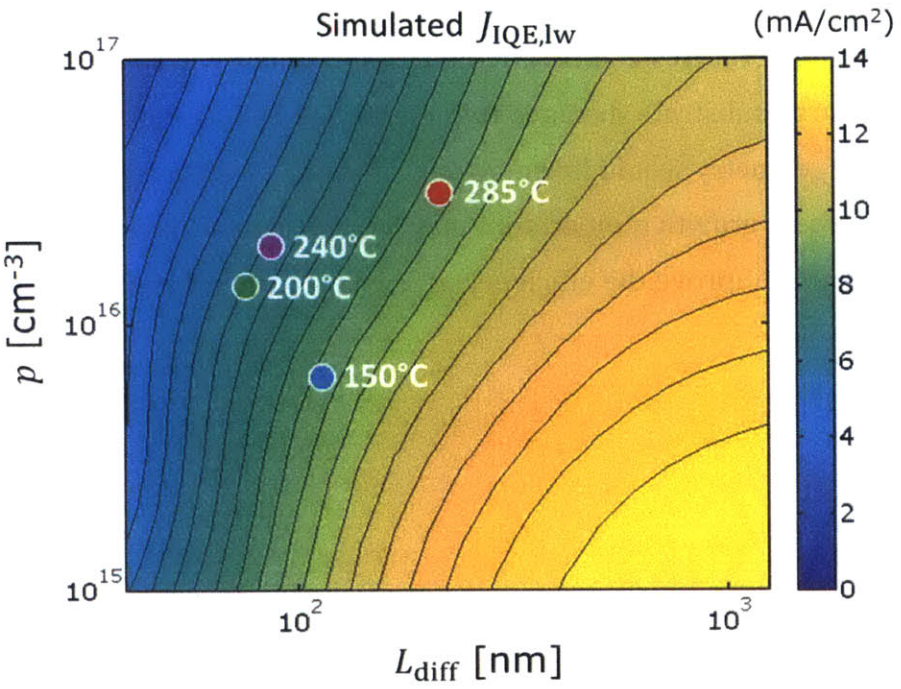

Figure 3-11. Contour plot of the current density $J_{IQE,lw}$ as a function of diffusion length L_{diff} (abscissa) and hole concentration p (ordinate). The experimental data points representing each growth temperature are positioned based on measured carrier concentration and fitted diffusion length. Within the parameter space plotted, lower p and higher L_{diff} tend to increase $J_{IQE,lw}$.

3.3 Conclusion

In summary, this work shows that by increasing growth temperature from 150 to 285°C, a local minimum in current density at long wavelengths is traversed due to the combined effects of a varying carrier concentration and diffusion length. The hole concentration monotonically increases with increasing growth temperature, which leads to decreasing drift-assisted carrier collection. At the highest growth temperature, the carrier collection recovers due to an increase in diffusive minority-carrier transport. Higher carrier collection may be achievable by simultaneously decreasing carrier concentration and increasing diffusion length. The fact that the trends in grain morphology, carrier concentration, and extracted diffusion length are observed after a post-growth annealing step of 400°C in H_2S ambient highlights the importance of defect engineering during thin-film growth to achieve optimum bulk material properties. The increase in diffusive carrier transport at 285°C is promising, as it suggests that even higher diffusion lengths and

enhanced device performance may be achieved with growth temperatures beyond 285°C. Higher substrate temperatures can be attained by increasing the source temperature and decreasing the source-substrate distance to increase the SnS adatom flux. Ideally, a close-space sublimation geometry would be employed, allowing far higher growth temperatures. These steps to increase growth temperature may be critical to achieve high-quality SnS thin films which ultimately improve the efficiency of SnS-based photovoltaic devices.

Chapter 4

Correlation between structural defects and minority-carrier collection

In this chapter, I seek to determine what types of extended structural defects are responsible, if any, for the low minority-carrier diffusion lengths in SnS. The results of Chapter 3 hinted that intragranular defects, as opposed to grain boundaries, are limiting the lifetime of our SnS films. I seek to test this hypothesis, and moreover, to reveal what types of intragranular defects are responsible for the low minority-carrier lifetime in our SnS films.

The minority-carrier collection properties measured in Chapter 3 are measured without spatial resolution. Ideally, the carrier collection properties would be measured with sub-micron spatial resolution to deduce what type of defect is limiting our minority-carrier collection. For this purpose, I focus on the highest-diffusion-length sample of the growth temperature study in Chapter 3, grown at 285°C, and employ correlative microscopy to ascertain the relative influence of different defects on the minority-carrier collection. Three microscopy techniques are employed on the same region of the sample that allow us to directly correlate extended structural defects to low minority-carrier collection.

The first technique, electron-beam-induced current (EBIC), provides information about the local minority-carrier collection properties of the film. In EBIC measurements, an electron beam excites free carriers in a sample with electrical contacts that connect to an external ammeter circuit. The free carriers that travel to the contacts are measured by the circuit. By scanning the electron beam across the sample, a spatial map showing the relative number of collected free carriers is obtained.

The second technique, transmission electron backscattered diffraction (tEBSD),[§] indicates the location of grain boundaries. The tEBSD technique measures the diffraction pattern of an electron beam transmitted through the sample using a two-dimensional detector. The measured diffraction pattern can then be fit to the calculated orientation-dependent diffraction pattern based on the known crystal structure of SnS, and thus the crystal orientation of the region of interest can be obtained. By scanning the electron beam spatially across the sample, tEBSD gives us the ability to spatially map grain orientation, and as a byproduct, the location of grain boundaries.

Lastly, transmission electron measurements (TEM) give us information about intragranular extended structural defects. In this technique, an electron beam is transmitted through a representative lamella of the sample are measured, and the electron transmission characteristics can be analyzed to identify stacking faults, twin boundaries, screw dislocations, and edge dislocations.

The results of this correlative microscopy study suggest that intragranular point defects, rather than extended defects, are the main lifetime-limiting defect in our highest-performing SnS thin-films.

In the second experiment, I seek to determine the cause of the improvement in diffusion length from the 240°C sample to the 285°C sample from Chapter 3. In particular, I seek to resolve whether a change in intragranular extended structural defect density is responsible

§ Technically, this measurement should be called "convergent beam electron diffraction." However, at the time of this writing, "transmission electron backscatter diffraction" is the terminology used in the literature for this type of measurement despite being somewhat of an oxymoron, likely because the associated data analysis techniques are similar to those used for standard electron backscatter diffraction. For the sake of consistency, I use "tEBSD" to refer to the measurement throughout the chapter.

for the increase in diffusion length at the highest growth temperature. Here, tEBSD and TEM are employed to characterize the structural defects in the 240°C sample, and the results are compared to those present in the 285°C sample. Although there is a difference in cross-sectional grain boundary density between the two samples, the intragranular extended structural defect density does not differ significantly, suggesting that another type of intragranular defect is responsible for the increase in diffusion length from 240°C to 285°C.

My main contributions to the work in this chapter are the experimental design, growth of SnS films, preparation of samples for microscopy, and the data analysis. The EBIC measurements are performed by Paul Rekemeyer. The TEM and tEBSD measurements are performed by Amanda Youssef and Austin Akey, who also helped in the interpretation of the TEM micrographs.

4.1 Materials and Methods

4.1.1 SnS films

The SnS thin-films used in this study are taken from the sample set used for the growth temperature study in Chapter 3. The $Si/SiO_2/Mo/SnS$ samples are grown at 240°C and 285°C followed by a post-deposition anneal at 400°C as already detailed in Section 3.1.1.

4.1.2 Cross-sectional electron-beam-induced current measurements

For electron-beam-induced current (EBIC) measurements, one representative device (of 11) from the sample is cleaved around the device as defined by the limits of the indium tin oxide layer, leaving a 0.5 mm border beyond the limits of device. The device is then cleaved midway along the short dimension of the device, leaving a 2.75 mm length of device cross-section exposed to air. Because of the polycrystalline nature of the SnS thin-film, the SnS layer generally cleaves along grain boundaries, leaving a relatively rough topology at the cross-section.

A 20 μm length of device cross section is then polished in a four-step process using a dual-beam scanning electron/focused Ga-ion beam microscope (Helios NanoLab 600, FEI). First,

a 20 μm × 2 μm rectangular platinum bar is deposited using the built-in gas injection system of the microscope. The platinum serves to protect the top surface of the device stack during the next three ion milling steps. In the first ion milling step, an ion beam with beam current of 2.7 nA and accelerating voltage of 30 kV is used over a rectangular area at the edge of the cross-section, with length 20 μm and width no more than 500 nm, completely overlapping with the Pt bar. The ion beam is tilted at an angle of 2.5 degrees off the top surface normal of the device, away from the cross-section plane. The tilt serves as an additional protection mechanism, ensuring that the top of the device stack is milled before the bottom. This initial step is done until the ion beam clearly mills through the entire device stack, as monitored by the SEM. A second milling step, employing a 90 pA, 30 kV ion beam over the same area, is done at 2 degrees tilt to more gently polish the cross-section. Finally, a third ion milling step at 150 pA and 5kV at 3 degrees tilt is done, primarily to remove Ga precipitates that originate from the ion beam itself.

After the cross-section polishing procedure, the sample is vented to air and removed from the microscope for 10–20 minutes, during which time the sample is mounted onto a custom EBIC sample stage. The sample is affixed to the stage using double-sided copper tape. The Mo back contact of the device stack is then exposed by mechanically exfoliating the top device layers with a razor blade in an area of the sample off of the active device area. A 2 mm × 1 mm × 0.5 mm indium bar is placed onto the Ag contact pad of the device. The indium bar serves as a soft mechanical buffer between the Ag contact pad and the electrical probe of the EBIC stage, preventing the accidental formation of shunts due to the probe puncturing the contact pad. Each of the two electrical probes consists of a copper-beryllium wire spot-welded to a stainless steel washer, which is fixed by a screw into the base of the stage. One of the probes is placed on the exposed Mo back contact of the device, and the other is placed on the indium bar on the top contact of the device. The sample is then placed back into the same dual-beam microscope (Helios NanoLab 600, FEI), which is equipped with an EBIC system (Point Electronic DISS5).

Electron-beam-induced current measurements were done at an accelerating voltage of 5 kV and beam current of 86 pA.

4.1.3 Preparation of the lamellae

The lamellae are prepared using a dual-beam scanning electron/focused Ga-ion beam microscope (Helios 660, FEI). If not already polished, the device cross-section is first polished using the procedure described in Section 4.1.2. The sample area of interest is then milled from the backside of the cross-section to a thickness of 1 μm at a slight angle so as to intersect with the polished cross-section surface at the substrate. One end of the milled out section is attached to a tungsten micromanipulator *in-situ* (Omniprobe 400) *via* platinum deposition, and then lifted out by ion-milling the opposite end. The sample bar is lifted out and placed on a sample grid meant for transmission electron microscopy. Pt is again used to weld the sample bar onto the sample grid. Once welded, the sample cross-section is thinned to 90–110 nm thickness using the ion beam again on the backside of the cross-section.

4.1.4 Transmission electron backscatter diffraction measurements

For obtaining grain orientation and grain boundary information, transmission electron backscatter diffraction (tEBSD) is done using again the dual-beam scanning electron/focused Ga-ion beam microscope (Helios 660, FEI). For this work, the electron beam is scanned in 150 nm steps, at an accelerating voltage of 30 kV and beam current of 26 nA. At each pixel, the software (OIM) automatically attempts to fit the diffraction lines to predicted diffraction lines based on user-inputted crystallographic data. The crystallographic data used in this case is based on literature data on single crystals of SnS.[22]

4.1.5 Transmission electron microscopy

Transmission electron microscopy is carried out in a JEOL 2010F at 200 kV. For both lamellae, a series of overlapping images along the entire length of the lamella is taken. The images are then stitched together using the vector graphics software Inkscape. Multi-beam micrographs are taken with a primary transmitted beam and one diffracted beam strongly excited.

4.2 Results and Discussion

4.2.1 Correlation between structural defects and current collection

Figure 4-1a shows a scanning electron micrograph (SEM) of the polished cross-section of the 285°C sample. The Mo back contact is visible as the smooth layer at the bottom, above which lies the SnS thin-film layer. The buffer layer (not visible at the magnification shown) and the transparent conducting oxide (TCO) layer conform to the topology of the SnS layer. The topmost layer shown in the SEM is platinum, used as a protective layer in the polishing process (Section 4.1.2). Several cracks are visible in the SnS layer. In addition, there is a large void in the SnS layer at the right side of the image.

The corresponding EBIC measurement is shown in Figure 4-1b, which uses a color scale to indicate the magnitude of the measured current. Here, the absolute magnitude of the measured current is not as important as the relative local variation in current. The brighter areas in the EBIC map correspond to areas of higher collection current. In the ideal case, the EBIC map would appear homogeneously bright throughout the entire SnS film thickness, which would indicate that carriers excited near the back Mo contact, despite having to travel through the entire SnS thickness, still reach the top contact. This would be indicative of a minority-carrier collection length well in excess of the film thickness. An example of this case is shown in Vyvenko *et al.*[115]

In contrast, the results show a ubiquitous presence of a short minority-carrier collection length relative to the film thickness. The majority of the current is collected from points of generation within 100-200 nm of the SnS/buffer junction. That is, only electrons that are generated within 100-200 nm of the SnS/buffer junction are likely to travel to the contacts and contribute to the current. There are two exceptions to this behavior in the EBIC map shown. The first is an unusual extension of the current collection near the midpoint of the map. The current profile follows the profile of a crack in the SnS, visible in Figure 4-1a. This can be explained by the fact that the buffer layer may coat the inside the crack, which extends the electrical junction into the thickness of the SnS layer. In fact, this phenomenon has been shown to lead to shunting in similarly processed SnS devices.[116] Thus, the

extension in the apparent current collection should not be mistaken for an increase in effective collection length in that area; instead, if the junction is assumed to extend into the crack, the current profile is consistent with the observed behavior in the rest of the sample – that the current collection is limited to 100-200 nm from the junction. The second exception occurs at the far right side of Figure 4-1b. Here there is a similar pattern, where the current profile dips below the normal 100-200 nm distance from the junction two times in close proximity. I attribute this behavior to a combination of two effects: there are two cracks that the current profile follows for the same reason as just explained; and electron scattering in the void visible in SEM causes an artificially high current magnitude at the location of the void. Thus, accounting for these two instances of unusual behavior, the data is consistent with a collection length of 100-200 nm.

The tEBSD data is shown in a series of three maps in Figure 4-1c-e. Figure 4-1d shows the tEBSD data in "image quality" view, where the brightness of each pixel indicates the certainty with which the tEBSD software is able to fit the measured diffraction pattern for that point. This view is especially useful for locating grain boundaries, as dark lines in this view should correspond to grain boundaries. As shown in Figure 4-1d, the 285°C lamella contains many grain boundaries, most of which are invisible by SEM alone. Figure 4-1e shows the inverse pole figure view of the data as fitted by the tEBSD software. The colors of each pixel correspond to a specific grain orientation fit by the software. Thus, pixels covering a single grain should be the same color. However, this view is difficult to interpret on its own due to the spatially varying certainty with which the software fits the measured diffraction pattern. Therefore, the inverse pole figure view is often overlaid with the image quality view to give a normalized pole figure, shown in Figure 4-1c. This view gives us additional information about the location of grain boundaries that may be difficult to distinguish from Figure 4-1d alone. For example, the boundary between grains that overlap through the thickness of the lamella will appear with weak contrast in Figure 4-1d, but may appear with strong contrast in Figure 4-1c. By using both views, one may deduce the location of grain boundaries in the film.

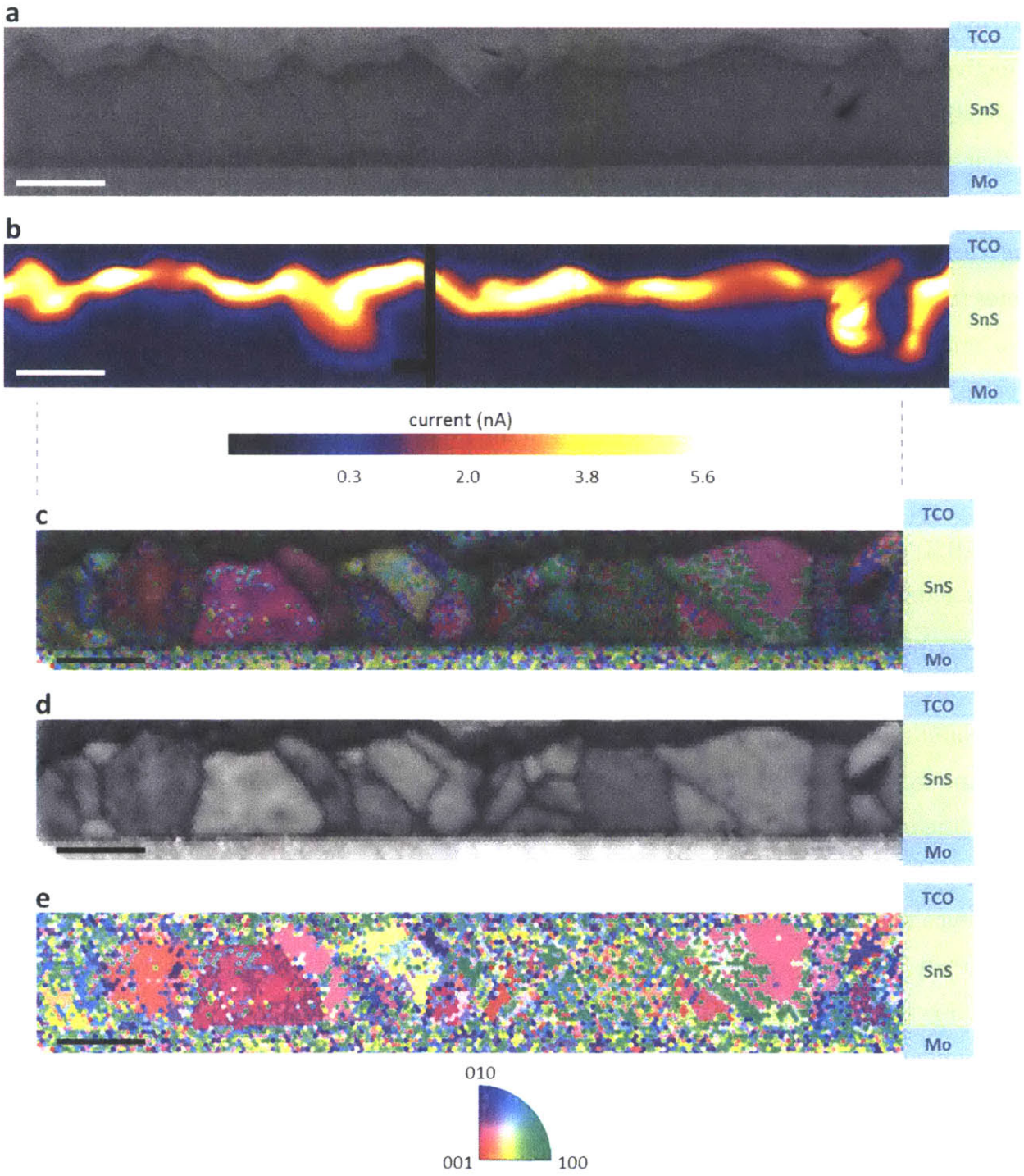

Figure 4-1. Correlative microscopy of the 285°C lamella. (a) Scanning electron micrograph, with the device stack labeled schematically at right. The buffer layer is present between the SnS and TCO layers, but is too thin to be seen at this magnification. (b) Electron-beam-induced current map. For clarity, the black rectangular areas near the center of the map block out annotations automatically generated by the data collection software. (c) Overlay of "Image quality" and inverse pole figure views from tEBSD data. (d) "Image quality" view of tEBSD data; dark lines indicate the position of grain boundaries. (e) Inverse pole figure from tEBSD data. All the images are aligned in the horizontal direction, and the scale bars indicate 1 μm.

Figure 4-2a shows a stitched bright-field transmission electron micrograph of the same lamella. The locations of grain boundaries apparent from TEM agree with those deduced from the tEBSD data. Only 3–4 stacking fault planes are found in the entire lamella. Instances of stacking faults are indicated by the red and blue squares in Figure 4-2a. Figure 4-2b is a close-up view of the red square in Figure 4-2a, showing a nearly complete stacking fault loop. Three more stacking fault edges are visible in Figure 4-2c, which is a close-up of the blue square, but it is unclear whether a subset of these stacking fault edges make up one stacking fault loop. Thus, the number of stacking fault planes is bounded at 3–4.

Although stacking faults are readily visible in off-axis bright-field micrographs, a thorough search for dislocations generally requires more sophisticated approaches. One representative grain is chosen on which to perform a thorough dislocation search (green square in Figure 4-2a), because dislocations may not be visible in the specific diffraction condition used by the bright-field TEM mosaic in Figure 4-2a. Figure 4-2d shows a micrograph of the grain in the multi-beam condition. In this condition, dislocations should appear as dark streaks, as they break the Bragg condition. There is no evidence of dislocations in this grain in the multi-beam condition. As a further check, the dark-field micrograph of the same grain is shown in Figure 4-2e. In this condition, dislocations should appear as bright streaks, and again, there is no evidence of dislocations.

For ease of visual analysis, the key features of the EBIC, tEBSD, and TEM data are consolidated in Figure 4-3. Here, the EBIC data from Figure 4-1b is overlaid with cyan lines that trace the location of grain boundaries inferred from tEBSD and TEM data, as well as gray boxes that indicate the location of stacking faults from TEM data. Using Figure 4-3, the structural defects characterized by tEBSD and TEM can be directly correlated to the minority-carrier collection.

First, it is apparent from Figure 4-3 that some grain boundaries are detrimental to minority-carrier collection. Regions 1, 3 and 4 in Figure 4-3 support this claim. In these regions, a reduction of current coincides with the location of a grain boundary. However, not all grain boundaries are equally detrimental. One case of this is Region 2 in Figure 4-3. Region 2 highlights an example where current collection within a grain remains nearly

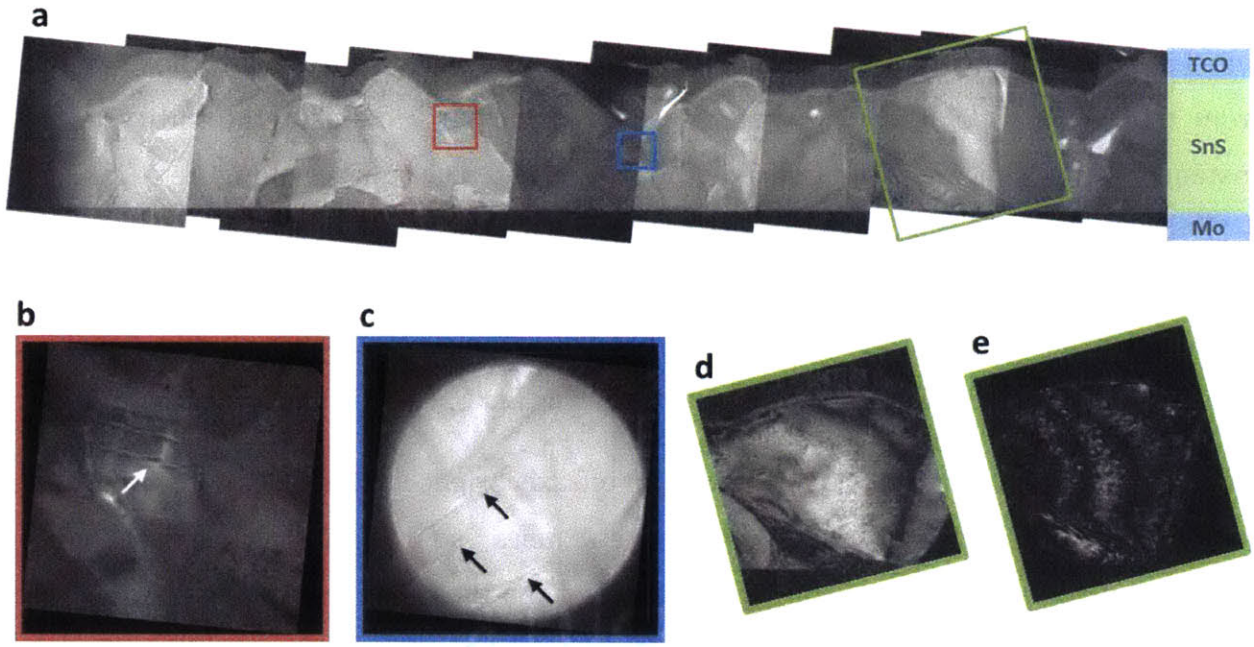

Figure 4-2. Transmission electron micrographs of the 285°C lamella. (a) Stitched bright-field micrograph of the entire lamella. Red and blue squares indicate locations of stacking faults. Green square indicates the grain chosen for measuring in the multi-beam condition and dark-field condition for the purpose of finding dislocations. (b) Close-up of the red square in (a), showing one nearly complete stacking fault loop, indicated by the arrow. (c) Close-up of the blue square in (a), showing evidence of three stacking fault lines (indicated by arrows), some of which may be of the same stacking fault loop. (d) Grain in the green square region measured on-axis in the multi-beam condition; no dislocations are visible. (e) Dark-field image of the grain in the green square region; again, no dislocations are visible.

constant in the lateral direction, even across grain the boundaries. This implies that the grain boundaries highlighted in Region 2 are not as recombination-active as those highlighted in Regions 1, 3 and 4.

Region 2 provides a counterexample to the hypothesis that grain boundaries are responsible for the ubiquitously short collection length observed in this sample. Even in Region 2, where the grain boundaries have little to no effect on the current collection, the effective collection length within the grain remains at 100-200 nm. If grain boundaries are the lifetime-limiting defect in our films, then there would be an increase in the collection length for the few grains with recombination-inactive grain boundaries, such as those in Region 2. Instead, Region 2 exhibits a similar collection length to that of the rest of the cross-section. Thus, I deduce that the ubiquitously short collection length is likely *not* due to recombination at grain boundaries, but rather intragranular defects. This is consistent

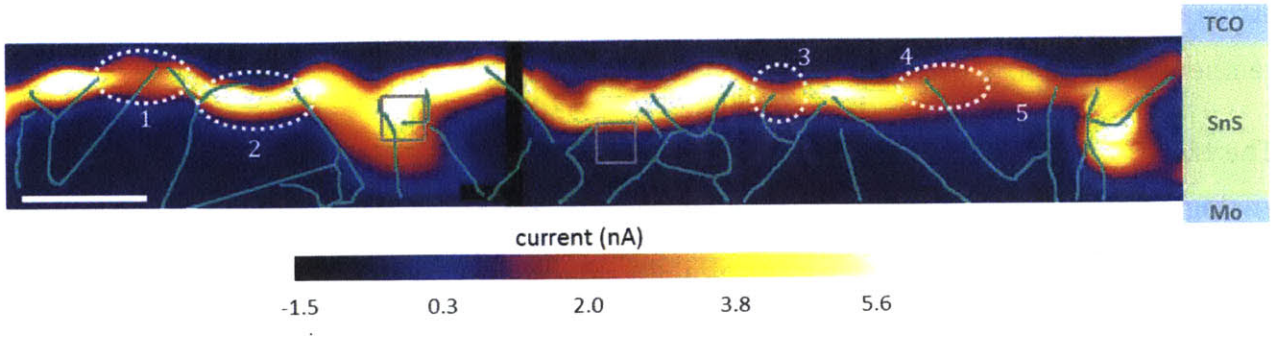

Figure 4-3. Electron-beam-induced current map from Figure 4-1b, with cyan lines tracing the location of grain boundaries inferred from tEBSD and TEM data (cyan lines), and gray boxes indicating the location of stacking faults from TEM data. Regions 1–4, indicated by the white dotted circles, are regions of current collection discussed in the text. Region 5 indicates the grain on which the thorough dislocation search is done. Scale bar indicates 1 μm.

with the results of Chapter 3, which do not show a correlation between plan-view grain size and quantum-efficiency-fitted minority-carrier diffusion length.

It is further inferred from the sparse presence of stacking faults and dislocations that intragranular extended structural defects are also not responsible for the short collection length. To explain the ubiquitously short carrier collection lengths, the density of the intragranular defects must be on the order of the collection length itself. Clearly, the density of stacking faults observed (3–4 within a volume of 10 × 1 × 0.1 μm^3 of SnS) is not enough to explain the short collection length. The density of dislocations is also similarly too low to explain the short collection length, at least within the grain for which the thorough dislocation search is done, indicated by Region 5 in Figure 4-3. Thus, I conclude that extended intragranular structural defects do not appear to be the lifetime-limiting defect in this SnS thin-film. The ubiquitous presence of a short collection length, combined with the flat EBIC profile of Region 2, suggests that a ubiquitously distributed defect is the root cause. The possibilities for this lifetime-limiting defect include intrinsic point defects such as sulfur vacancies and extrinsic point defects or complexes due to contaminants.

4.2.2 Effect of growth temperature on extended structural defect density

In this section, I present and discuss the results of the tEBSD and TEM measurements on the 240°C sample, with the intent to determine whether a change in intragranular extended

structural defect density is responsible for the increase in diffusion length from a growth temperature of 240°C to 285°C.

The tEBSD data for the 240°C lamella is shown in a series of three images in Figure 4-4, analogous to the series for the 285°C lamella in Figure 4-1a,c-e. Figure 4-4a shows the SEM of the lamina just before taking the tEBSD data. Analogous to the 285°C sample lamella, the Mo back contact, the SnS layer, the TCO layer, and the Pt protective layer are visible. One crack, along with several voids at the Mo/SnS interface, are visible. Figure 4-4c shows the tEBSD data in "image quality" view, where the dark lines are indicative of grain boundaries. Figure 4-4d shows the inverse pole figure, and Figure 4-4b shows the overlay of the image quality and inverse pole figure views. Comparing Figure 4-1c to Figure 4-4b, the cross-sectional grain boundary density of the 240°C sample is higher than that of the 285°C sample. This is consistent with the plan-view grain size quantification done in Chapter 3 for these two samples.

Figure 4-5a shows a stitched bright-field transmission electron micrograph of the same 240°C lamella. The locations of grain boundaries apparent from TEM agree with that deduced from the tEBSD data. Evidence of only 2 stacking faults are found in the lamella, indicated by the red and blue squares in Figure 4-5a. Figure 4-5b is a close-up view of the red square in Figure 4-5a, showing a stacking fault edge that traverses nearly the entire thickness of the SnS layer. Figure 4-5c is a close-up view of the blue square in Figure 4-5a, showing evidence of a stacking fault edge near the Mo/SnS interface. Although a thorough dislocation search on the 240°C lamella is not done, the presence of dislocations at a significantly higher density than in the 285°C is unlikely because no evidence of dislocations is found for any of the >30 differently oriented grains observed in the bright-field transmission micrographs.

The 240°C and 285°C samples are observed to have similar densities of stacking faults and dislocations. This provides further evidence to support the hypothesis in the previous section and in Chapter 3, that the improvement in diffusion length is likely not due to a reduction of intragranular extended structural defects, but rather, a change in another type of intragranular defect not measured herein. As discussed in the previous section, this may

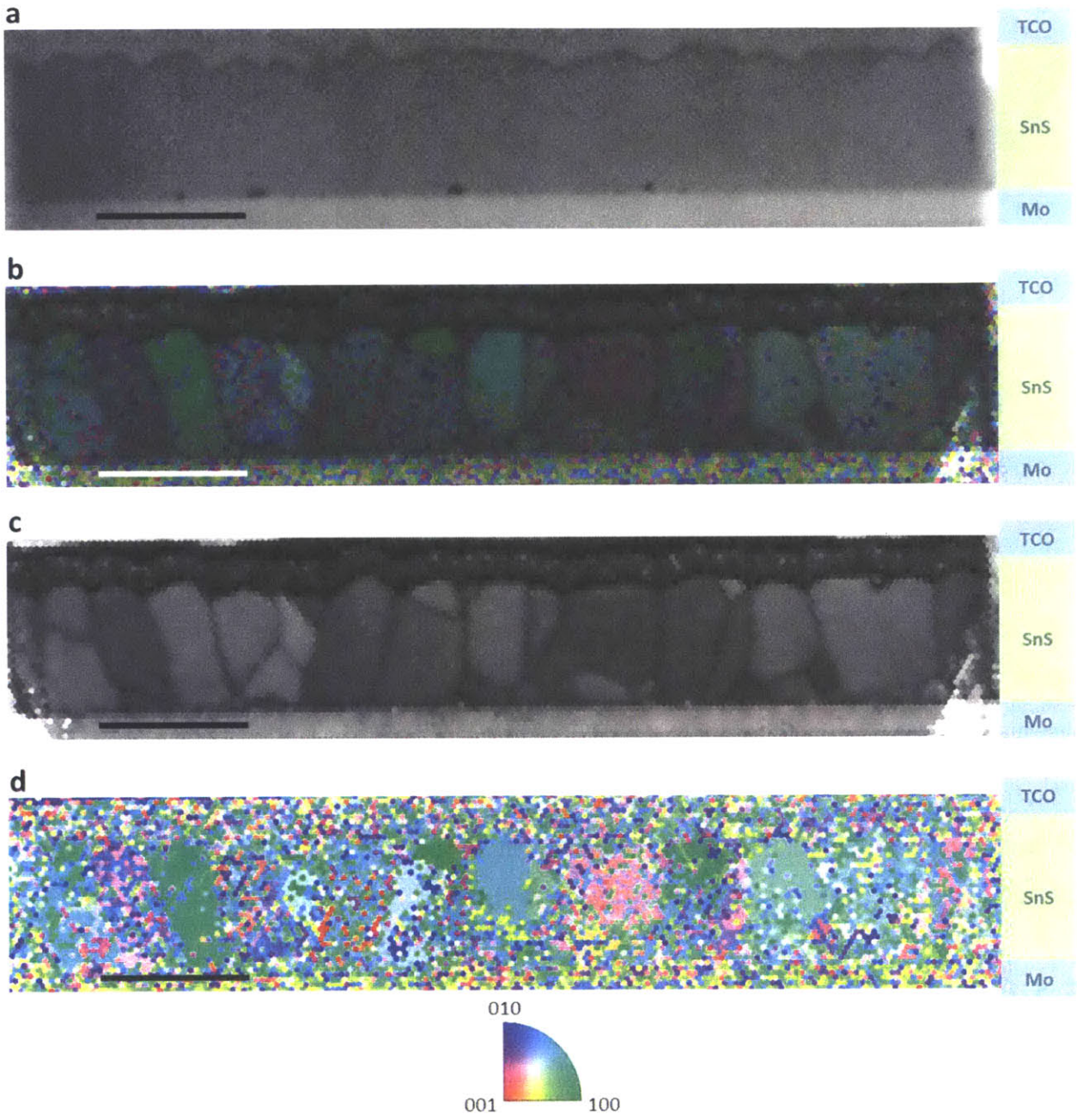

Figure 4-4. Correlative microscopy of the 240°C lamella. Transmission electron backscatter diffraction (tEBSD) data for the 240°C sample. (a) Scanning electron micrograph of the cross-section of the 240°C lamella. (b) Overlay of "Image quality" and inverse pole figure views from tEBSD data. The bright spots in the lower left and right corners may be ignored, as these correspond to areas coated with Pt used for the lamella preparation process. (c) "Image quality" view of tEBSD data; dark lines indicate the position of grain boundaries. All the images are aligned in the horizontal direction, and the scale bars indicate 1 μm.

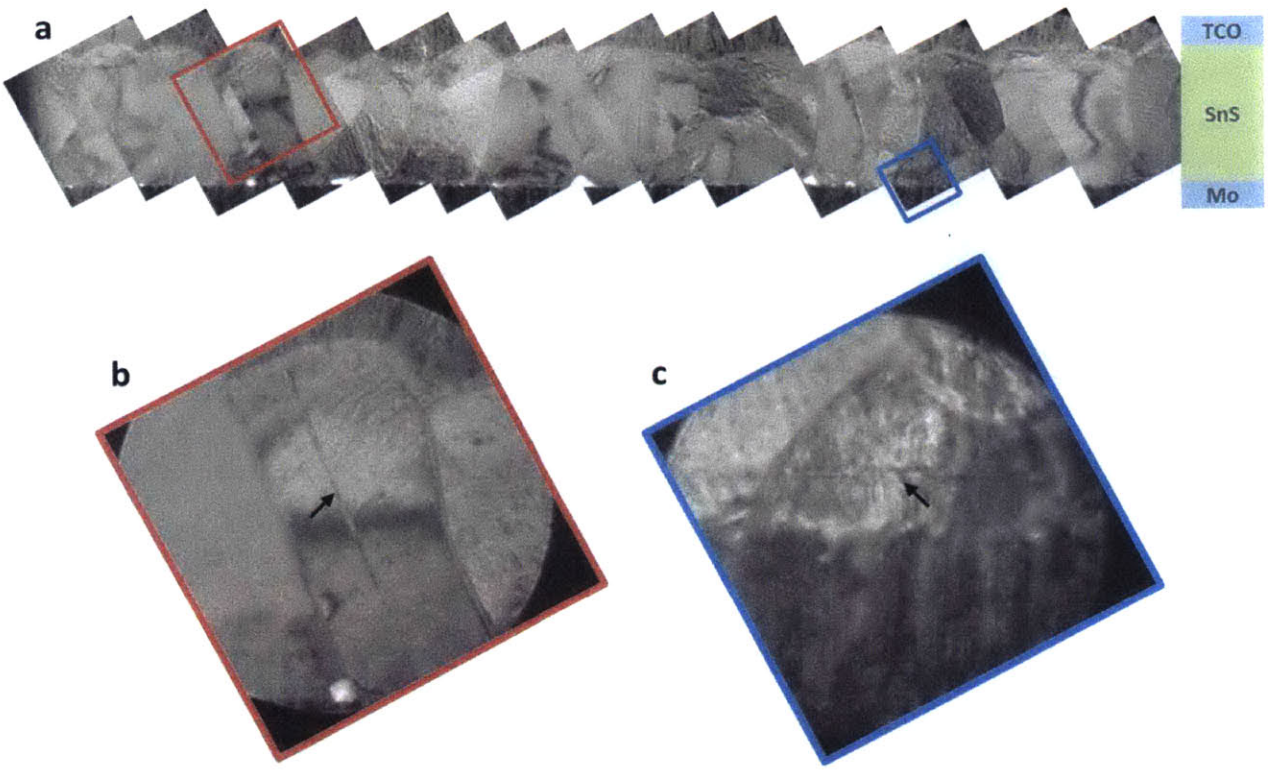

Figure 4-5. Transmission electron micrographs of the 240°C lamella. (a) Stitched micrograph of the entire lamella. Red and blue squares indicate locations of stacking faults. (b) Close-up of the red square in (a), showing a stacking fault (indicated by the arrow) that appears to run through the entire thickness of the SnS layer. (c) Close-up of the blue square in (a), showing one stacking fault (indicated by the arrow) near the Mo back contact.

be an intrinsic or extrinsic point defect. Such defects have been shown to limit the intragranular lifetimes of silicon and other thin-film PV absorber materials.[75,117]

4.3 Conclusion

This chapter marks a critical step in determining the lifetime-limiting defect(s) that are responsible for the short minority-carrier diffusion lengths in our SnS thin-films. By utilizing a combination of tEBSD, TEM, and EBIC measurements, extended structural defects are directly correlated to minority-carrier collection in our highest-performing (285°C) film from the growth temperature study of Chapter 3. The results suggest that intragranular point defects, as opposed to grain boundaries or intragranular extended structural defects, are likely responsible for the short diffusion length in the 285°C sample. In addition, extended structural defect density of the shorter-diffusion-length sample

grown at 240°C is measured to find that the improvement in diffusion length at 285°C is also likely due to reduction of detrimental intragranular point defects, rather than extended structural defects.

Chapter 5

Effect of SnS anisotropy on current and open-circuit voltage

5.1 Introduction

Chapters 3 and 4 investigate the effect of structural defects on the minority-carrier lifetime of SnS thin films, motivated by the fact that the low minority-carrier lifetime is currently the main barrier to achieving high-efficiency SnS photovoltaic devices. In this chapter, I explore secondary effects that may play a role in future device engineering efforts. In particular, this chapter explores the role that the structural anisotropy of SnS may play in device engineering.

As discussed in Section 1.1.2, SnS has a highly anisotropic crystal structure with an orthorhombic unit cell. This crystallographic anisotropy leads to anisotropic optoelectronic properties such as carrier mobility, absorption coefficient, surface energy, and electron affinity. I explore two of these material properties, electron affinity and surface energy, as they have the potential to have a profound impact on future device engineering efforts.

5.1.1 Anisotropic electron affinity

With regards to electron affinity, the electron affinity of SnS has been calculated to be highly dependent on the surface orientation.[25] In fact, the disparity between electron

affinities of different crystal planes of SnS is calculated to be as high as 0.9 eV.[25] Because SnS thin films are polycrystalline with a relatively random grain distribution, the orientation-dependent electron affinity is expected to lead to a lateral grain-to-grain variation of the SnS electron affinity across the thin-film surface. When the *n*-type buffer is deposited, this in turn leads to a laterally inhomogeneous conduction band offset at the heterojunction interface. For a random grain orientation distribution, this may lead to a significant fraction of grains having a sub-optimal conduction band offset, causing losses in the current and voltage of the device. Thus, the anisotropy of the electron affinity, combined with the randomly oriented grains of the polycrystalline SnS thin film, may inherently limit the true potential of a SnS-based photovoltaic device.

The issue of lateral inhomogeneity in polycrystalline thin-film photovoltaics is not new. Bandgap and electrostatic fluctuations in $Cu(In,Ga)(S,Se)_2$ (CIGS) and $Cu_2ZnSn(S,Se)_4$ (CZTS), caused by a variety of compositional and structural inhomogeneities, have long been hypothesized to cause V_{OC} loss in devices.[79,80] In the analytical model developed by Werner *et al.*,[79] both bandgap and electrostatic fluctuations form recombination pathways that span energy differences smaller than the average bandgap, thus decreasing the quasi-Fermi level difference in the material and limiting the V_{OC}.[79,80] For the case of CZTS, photoluminescence data has been analyzed to deduce that one major factor limiting device efficiency is the presence of electrostatic potential fluctuations on the order of 10 meV.[118]

However, the analytical model developed by Werner *et al.*[79] to treat electrostatic potential variation in a device is not directly applicable to the problem of grain-to-grain electron affinity variation in a device. This is because one of the fundamental assumptions of the model is that the length scale of the electrostatic variation is much smaller than the length scale of the space-charge region. This is obviously not the case for the case of grain-grain electron affinity variation in a SnS thin film, since the length scale of variation is the size of a grain, about 1 μm, while the length scale of the space-charge region is 100-400 nm (as shown in Chapter 3). For these types of cases in which the potential varies on a relatively large length scale, numerical multi-diode models may be used.[119]

In the multi-diode approach, the spatially inhomogeneous photovoltaic device is modeled by an equivalent circuit consisting of a network of photodiode elements, each of which may have unique electrical characteristics, connected in parallel. In the case of grain-to-grain variation of potential, each element may represent one grain. In the most general case, the network is two-dimensional, with each element representing a finite area of the device, and the elements are connected by a lateral series resistance. Thus, the two-dimensional area of the device is modeled by two-dimensional network of one-dimensional photodiode elements. While multi-diode models may provide insights about the effect of grain-to-grain inhomogeneities, they do not take into account the effect of lateral current flow across grain boundaries. Lateral current flow can be ignored in cases for which the drift and diffusion lengths are much smaller than the size of each grain, as might be the case for a multicrystalline silicon solar cell. However, in the case of the here-studied SnS films, the SnS grain size (100 nm – 1 μm) is typically on the same order as the minority-carrier collection length. Thus, lateral current flow may play a significant role in realistic SnS devices, an effect not captured by multi-diode models.

In the following computational simulation study, two models are used, each comprising a simple two-grain system, to determine the theoretical impact of the orientation-dependent electron affinity on SnS device performance. The first model uses a multi-diode approach, stringing the two grains in parallel, with each grain separately modeled as a one-dimensional optoelectronic system. The second model is a two-dimensional optoelectronic model of the two grains adjacent to one another, taking into account two-dimensional current flow effects. The results show that two dimensional effects indeed significantly affect device performance, and in a beneficial way. Lateral current from grains with sub-optimal electron affinity toward grains with near-optimal electron affinity makes the device robust to variations in the electron affinity from grain to grain. However, achieving uniform electron affinity, and thus grain orientation distribution, is still necessary to achieve the highest efficiency.

For this work, the design of the computational simulation and analysis of the results are the author's main contributions, and the execution of the simulation is done by David Berney Needleman.

5.1.2 Anisotropic surface energy

Similar to the electron affinity, the surface energy of SnS varies significantly across different crystal surfaces. The van der Waals character of the bonding between basal planes of the SnS crystal structure result in a basal-plane surface energy (9.6 meV/Å^2) less than half of any other crystal plane of SnS.[25] The basal plane of SnS is thus thermodynamically favored for a crystal in vacuum, which leads to a plate-shaped Wulff construction with the dominant crystal facet corresponding to the basal plane.[25]

This anisotropy may be harnessed to induce the growth of low-defect-density SnS films through the careful selection of a substrate. Traditionally, epitaxial growth is achieved by choosing a substrate of similar lattice constant. Indeed, heteroepitaxy of SnS onto sodium chloride, which is well lattice-matched to SnS, has been achieved.[120] However, another method is to take advantage of the layered structure of SnS and choose substrates that are terminated by van der Waals bonds. Thermally evaporated SnS growth on graphene[121] and mica[122] have been shown to yield highly basal-plane-oriented films large crystallite sizes (>1 μm), suggesting that van der Waals-terminated substrates increase the diffusion length of ad-atoms on the substrate and facilitate the layered growth of SnS. Although the morphological properties of the SnS films were measured in these works, the minority-carrier lifetime was not, and it remains to be seen whether SnS growth on van der Waals substrates results in higher minority-carrier lifetimes.

In the second portion of this chapter, SnS is grown on a SiO_2 substrate with and without a graphene overlayer, and the addition of the graphene is shown to improve the minority-carrier lifetime of the SnS film. Motivated by this improvement in lifetime, SnS is also grown on a Mo/graphene substrate, since Mo/graphene/SnS could be more easily inserted into the existing device fabrication process described in Chapter 3. Although the SnS film morphology on Mo/graphene is not directly transferrable to the device process, the results show a promising path toward the ideal SnS film, with both a low structural defect density enabling a high minority-carrier lifetime, as well as a uniform grain orientation ensuring a low variation in electron affinity across the film.

My main contributions to this portion of the work is in the experimental design, SnS film growth, most of the film characterization, and data analysis. The graphene is grown and transferred to the substrate by Marek Hempel, and the transient optical pump, terahertz probe measurements are performed by Benjamin K. Ofori-Okai.

5.2 Materials and Methods

5.2.1 Anisotropic electron affinity modeling

5.2.1.1 Schematic overview of models

Figure 5-1 shows a schematic representation of the two models. Both models contain two SnS grains, each with its own electron affinity χ_1 and χ_2. The schematic shown at left in Figure 5-1 shows the model using the multi-diode approach, called the "parallel" model. This model consists of two separate device stacks. The only difference between the device stacks is the electron affinity of the SnS grain at the SnS/Zn(O,S):N interface. The two device stacks are strung in parallel with no lateral resistance. The current-voltage (JV) curves of the two device stacks are first simulated separately, given χ_1 and χ_2, by numerically solving the semiconductor equations in (effectively) one-dimension. The total JV curve is computed by adding the current from the two device stacks.

The schematic shown at right in Figure 5-1 shows the two-dimensional model, called the "2D" model. Here, the two grains, each having a square cross-section, meet at a common grain boundary and are contained in a single device stack. The full two-dimensional semiconductor equations are numerically solved to obtain the total JV characteristics of this device.

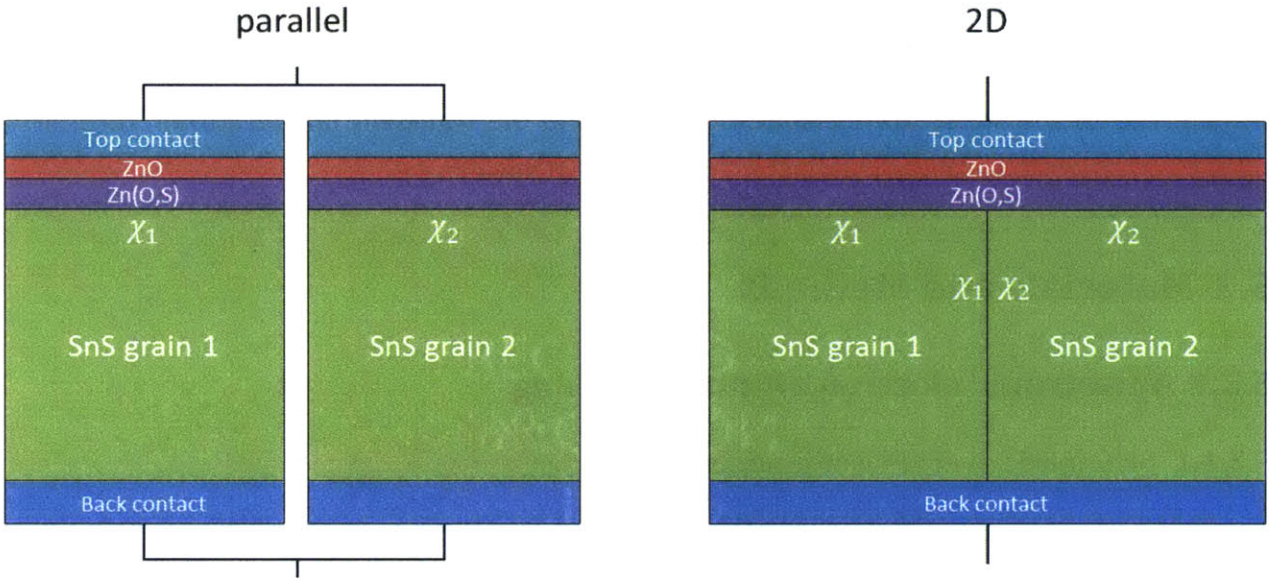

Figure 5-1. Schematic of the parallel 1D model (left) and the 2D model (right). Not to scale.

5.2.1.2 Numerical model

All device simulations are done using the TCAD Synopsis Sentaurus software package. The simulated device geometry is shown to scale in Figure 5-2. The device geometry consists of an ohmic bottom contact, two adjacent SnS slabs, a Zn(O,S):N layer, ZnO layer, and an ohmic top contact. All of the layers except for the SnS slabs span the entire width of the device. The thickness of the SnS slabs in the vertical (Y) direction is 1 μm. The total width of the simulated device is 1 μm, making each SnS slab 0.5 μm wide; however, reflective boundary conditions in the lateral (X) direction are employed, making the effective shape of each grain square (1 μm × 1 μm) as depicted in Figure 5-1.

The physical parameters of the SnS, Zn(O,S):N, and ZnO layers are similar to those previously determined in Section 3.1.3 for the 240°C sample and are listed in Table 5-1. The minority-carrier lifetime is set by Shockley-Read-Hall recombination with a single, symmetric-cross-section, neutral mid-gap defect level.[85,86] The results of the parallel and 2D models are computed for two scenarios: a "present-day" scenario, in which the minority-carrier lifetime is 100 ps, consistent with measurements on present-day devices,[68] and a "high-efficiency" scenario, in which the minority-carrier lifetime is 500 ns. These lifetimes are chosen to be consistent with a previously published work.[73]

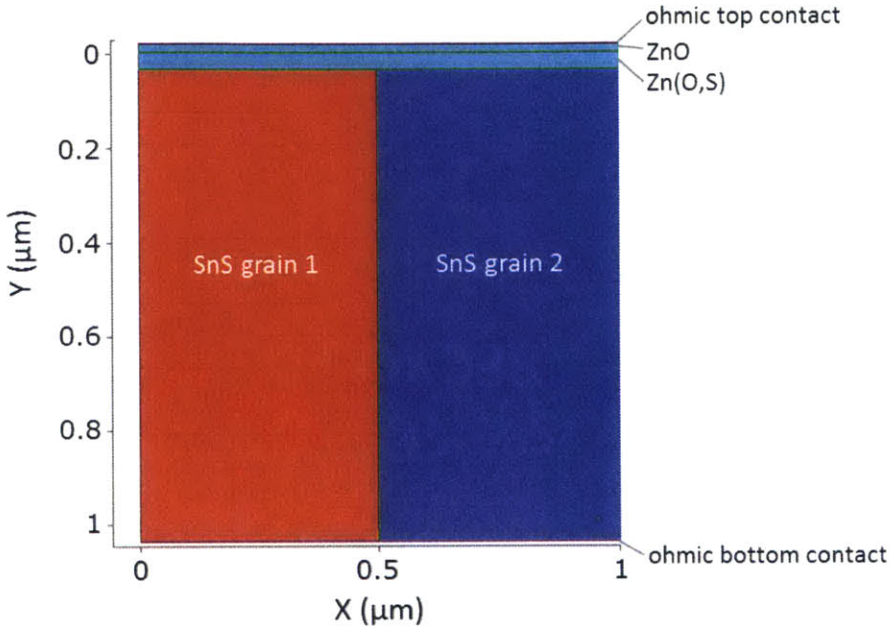

Figure 5-2. Two-dimensional device geometry for numerical simulations, consisting of an ohmic bottom contact (pink line), two adjacent slabs of SnS (red and blue), Zn(O,S):N/ZnO layers (light blue), and an ohmic topic contact (pink line), All layers except the SnS slabs span the entire width of the device. Each SnS slab is 0.5 μm × 1 μm, but the reflective boundary conditions in the X direction make the effective SnS slab size 1 μm × 1 μm.

For both the parallel and 2D models, the electron affinities of each SnS grain (χ_1 and χ_2) are separately varied from 3.28 eV to 5.28 eV in 0.1 eV increments. Thus, the disparity in electron affinity between the SnS grains, $\Delta\chi = \chi_2 - \chi_1$, is effectively varied from 0 to 2 eV. Note that for each grain, the SnS electron affinity is the same at the SnS/Zn(O,S):N interface as it is at the SnS/SnS interface. The generation rate is pre-computed using the Beer-Lambert law for AM1.5 illumination from the top of the device, using the previously measured absorption coefficient of SnS.[21] For the 2D model, the two-dimensional semiconductor equations are numerically solved at bias voltages from 0 V to the open-circuit voltage, using thermionic emission boundary conditions at heterojunctions, perfect ohmic contacts at the top and bottom of the device, and reflective boundary conditions in the lateral direction. The solar cell parameters J_{SC}, V_{OC}, FF, and efficiency are extracted from the simulated JV curves.

For the parallel model, the two device stacks are simply computed separately using the same simulation setup, except that the two adjacent grains of SnS are replaced by a single

Material parameter	Value for present-day scenario	Value for high-efficiency scenario	Source
SnS thickness	1000 nm		SEM cross-section
SnS bandgap	1.1 eV		[30]
SnS dielectric constant	42.1		[103], XRD for anisotropic correction
SnS $h^+(e^-)$ mobility	37.9		Hall effect (m_h^*/m_e^* from [30])
SnS $h^+(e^-)$ lifetime	100 ps	500 ns (500 ns)	
SnS h^+ carrier density	2.0e16 cm^{-3}		Hall effect
SnS optical absorption coefficient	Measured for $T_g = 240°C$.		[21]
SnS $h^+(e^-)$ effective mass	0.68 (0.28) m_0		[30]
SnS valence (conduction) band density of states	3.6e18 (1.4e19) cm^{-3}		from effective mass
SnS/Zn(O,S):N interface recombination velocity	1e7 cm/s	1e2 cm/s	[73]
SnS/SnS interface recombination velocity (2D model)	0 cm/s	0 cm/s	
Zn(O,S):N thickness	36 nm		[21]
Zn(O,S):N e^- carrier density	5.3e13 cm^{-3}		[73]
Zn(O,S):N, ZnO dielectric constant	9		[104]
Zn(O,S):N, ZnO $h^+(e^-)$ effective mass	2.0 (0.19) m_0		[105]
Zn(O,S):N, ZnO valence (conduction) band density of states	7.0e19 (2.0e18) cm^{-3}		from effective mass
ZnO thickness	10 nm		[21]
ZnO e^- carrier density	1e19 cm^{-3}		[106,107]
ZnO, Zn(O,S):N electron affinity	4.28 eV		[108]
ZnO, Zn(O,S):N bandgaps	> 2.5 eV		[73]

Table 5-1. Material parameter values for device layers assumed in optoelectronic simulations. Parameter values are equivalent to those used for the 240°C sample listed in Table 3-1, except for the Zn(O,S):N thickness and interface recombination velocity. The high-efficiency scenario column indicates only the values that differ from the present-day scenario. The values for the high-efficiency scenario are motivated by those chosen by Mangan *et al.*[73]

slab of SnS spanning the entire width of the device. This reduces each simulation to a one-dimensional problem, since the model does not vary in the X direction in this case. The resultant *JV* curves from the two device stacks are then added at each voltage bias to give the total *JV* curve of the parallel two-grain system. The solar cell parameters are similarly extracted from the computed total *JV* curve.

5.2.2 SnS growth on graphene

I deposit SnS on four different substrate types: SiO_2, $Si/SiO_2/Mo$, SiO_2/graphene, and $Si/SiO_2/Mo$/graphene. The SiO_2 substrates are fused silica (Quartz Scientific) squares of

size 8 mm × 8 mm × 0.5 mm. The Si/SiO_2 substrates are commercially available polished Si wafers with a thermal oxide (oxide thickness >300 nm), also of size 8 mm × 8 mm × 0.5 mm. All substrates are cleaned in a hot solvent bath. Mo is sputtered in two layers for a total thickness of 720 nm, as described in a prior work.[21] In the following text, "Mo substrate" shall refer to the $Si/SiO_2/Mo$ substrate. Monolayer graphene is synthesized on Cu foil as described in a prior work,[123] and then transferred onto the SiO_2 and $Si/SiO_2/Mo$ substrates using a PMMA transfer method.[124]

The SnS thin films are grown using a dedicated single-source thermal evaporator in the Langmuir configuration under high-vacuum conditions (10^{-7}–10^{-8} Torr), using commercially available SnS powder (Sigma Aldrich, >99.99%) as source material. Substrate temperature is held at 240 ± 30°C during the deposition, and substrate rotation is employed to guarantee uniform coverage. The deposition rate, controlled by the source temperature, is held at 1-2 Å/s, at a source-substrate distance of 10 cm. After SnS deposition, all samples are exposed to air for at least 24 hours before characterization.

SnS film morphology is imaged by field-emission scanning electron microscopy (SEM, Zeiss Ultra-55), and the crystal structure and texture of the films are analyzed by X-ray diffraction (Rigaku SmartLab) with Cu $K\alpha$ radiation using a θ-2θ scan.

The transient free carrier dynamics of the SiO_2/SnS and $SiO_2/graphene/SnS$ samples are measured with optical-pump, THz-probe transient photoconductivity in a similar fashion to previous measurements on SnS.[72] An optical pump at a wavelength of 800 nm is used to generate free carriers, and the amplitude of the transmitted THz electric field (T) through the sample is measured as a function of the time t after the pump event. The raw data is $\frac{\Delta T}{T_0} \equiv (T(t) - T_0)/T_0$, where T_0 is the measured transmission in the absence of a pump.

The sample is oriented such that both the optical pump and THz probe are incident on the SnS, as opposed to the SiO_2 substrate. All measurements are done at room temperature in air. Because graphene may interact with the THz probe, a control sample of similarly prepared SiO_2/graphene, without an SnS film, is also measured to ensure that the absorption in the graphene is negligible. The bandwidth of the THz measurement is

approximately 2 THz. Further details about the experimental setup may be found elsewhere.[125]

Similar to previous transient THz absorption analysis on SnS,[72] the raw data are transformed to excess-carrier concentration $\bar{n}(t)$ using the equation for the amplitude transmission through an air/ thin film/substrate structure,[126]

$$\bar{n}(t) \propto \frac{-\Delta T/T_0}{1+\Delta T/T_0}.$$

Because I am interested only in the relative difference in the excess-carrier decay dynamics between samples, $\bar{n}(t)$ is normalized relative to its maximum.

5.3 Results and Discussion

5.3.1 Anisotropic electron affinity modeling

The efficiency, J_{SC}, and V_{OC} for the present-day scenario are shown for all simulated pairs of χ_1 and χ_2 in the contour plots in Figure 5-3. The horizontal and vertical axes of all of the contour plots represent χ_1 and χ_2, respectively, and are equivalent across all of the contour plots. Plots on the left correspond to the parallel model, and plots on the right correspond to the 2D model. Positions P1, P2 and P3, shown once in Figure 5-3a, are positions of interest referred to in the following discussion and apply to all of the contour plots in Figure 5-3. Due to the reflective symmetry of the device geometry, all the plots are symmetric about the diagonal dotted line shown in Figure 5-3a, which corresponds to $\Delta\chi = 0$. Traversing the contour plot in a direction parallel to this line corresponds to keeping $\Delta\chi$ constant; that is, both χ_1 and χ_2 are varied together along any diagonal line of slope 1.

I begin by discussing the parallel model results. Figure 5-3a shows how the efficiency changes as χ_1 and χ_2 are varied for the parallel model. P1 indicates the efficiency maximum of 4.9%, at $\chi_1 = \chi_2 = 4.28$ eV. That is, the optimal efficiency occurs when both the disparity $\Delta\chi = 0$, and when the conduction band offset at the SnS/Zn(O,S):N heterojunction is zero (recall that the Zn(O,S):N electron affinity is also 4.28 eV). The energy band diagram across

the heterojunctions of both grains thus looks as shown in Figure 5-4a. In this case, for either grain, the minority electrons generated in the SnS layer experience no energetic change as they cross the heterojunction.

As we move to the left or down from the maximum efficiency point P1, the electron affinity of one of the SnS grains is lowered while keeping the other constant at its optimal value. The extreme case of this is shown by P2, at which the efficiency drops to 3.8%. This drop in efficiency can be attributed mostly to a drop in the V_{OC}. As we move from the maximum efficiency point (P1) toward P2, the V_{OC} (Figure 5-3b) drops by 28%, from 0.323 V to 0.233 V, while the J_{SC} (Figure 5-3c) remains nearly constant. The drop in V_{OC} from P1 to P2 can be explained by considering the band diagram of each grain across the heterojunction. In the case of P2, one of the grains has a lower electron affinity, leading to a negative conduction band offset, or "cliff" offset (Figure 5-4b). For this grain, the minority electrons thermalize down to the lower conduction edge of the Zn(O,S):N as they cross the heterojunction, resulting in a voltage loss for this grain. Although the other grain remains at an optimal band offset of zero, the loss in voltage incurred by the lower-electron-affinity grain dominates the total *JV* characteristics because the two grains are connected in parallel.

On the other hand, as we move to the right or up from the maximum efficiency point (P1), the electron affinity of one of the SnS grains is increased, and the efficiency drops more precipitously, down to 2.5% at P3. This efficiency loss can be attributed mostly to a drop in the J_{SC}. As we move from the maximum efficiency point (P1) toward P3, the J_{SC} (Figure 5-3c) drops by 49%, from 25.7 to 13.0 mA/cm^2, while the V_{OC} (Figure 5-3b) remains nearly constant. The decrease in J_{SC} can easily be understood again by considering the heterojunction energetics. The relatively high electron affinity of one SnS grain results in a positive conduction band offset, or "spike" offset, at the SnS/Zn(O,S):N interface (Figure 5-4c). For this grain, minority electrons experience a high energetic barrier at the SnS/Zn(O,S):N interface, impeding current flow across the interface. Thus, at P3, one grain has a current-blocking interface, while the other remains at the optimal band offset. When these two grains are connected in parallel, the currents add to result in about half of the current relative to the case where both grains have the optimal offset (P1).

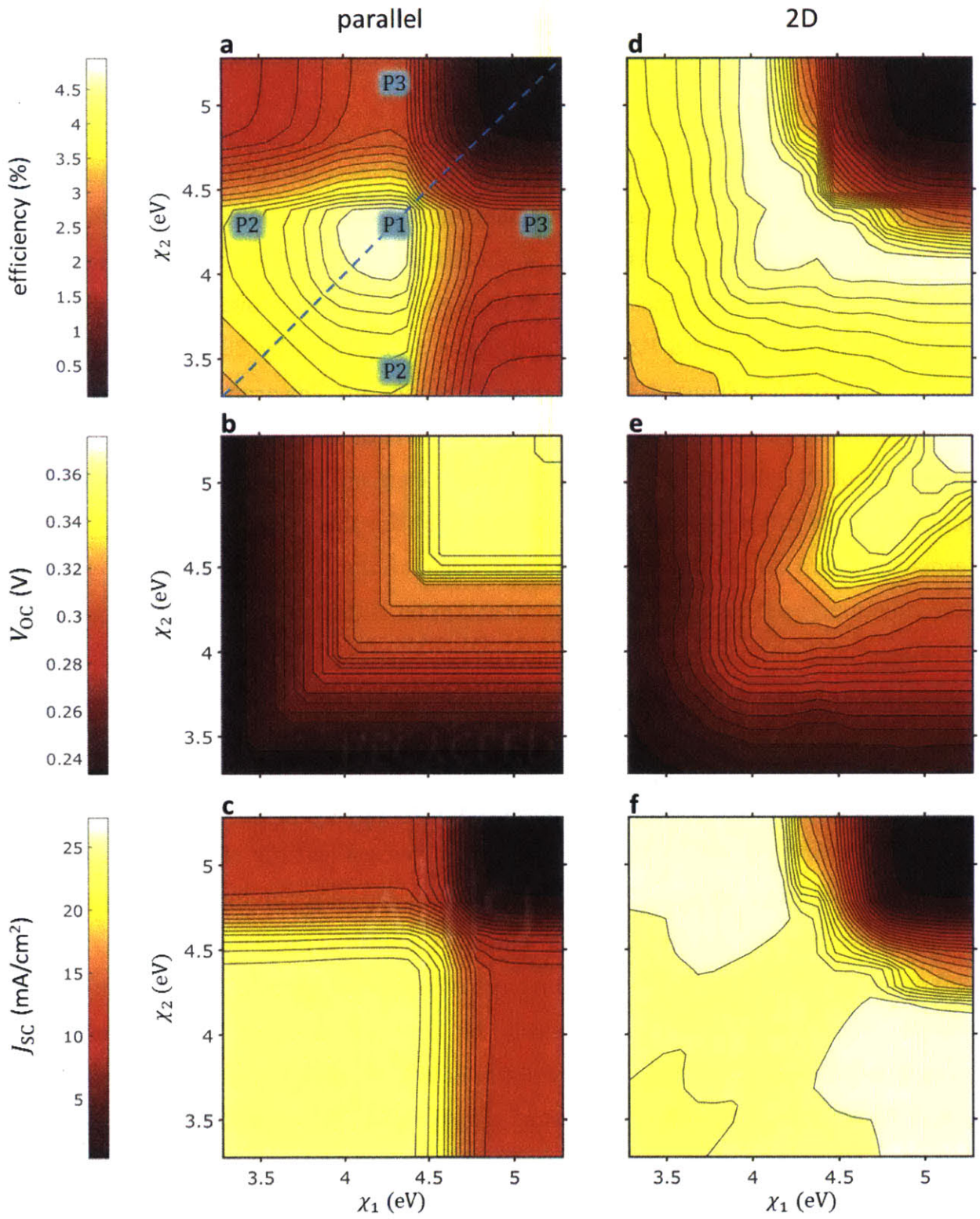

Figure 5-3. Contour plots of simulated efficiency, V_{OC}, and $J_{SC}$of present-day case using the parallel grain model (a-c) and 2D grain model (d-f). Horizontal and vertical axes represent the electron affinity of each grain and are equivalent across all contour plots. Numbers in (a) denote cases of interest discussed in the text.

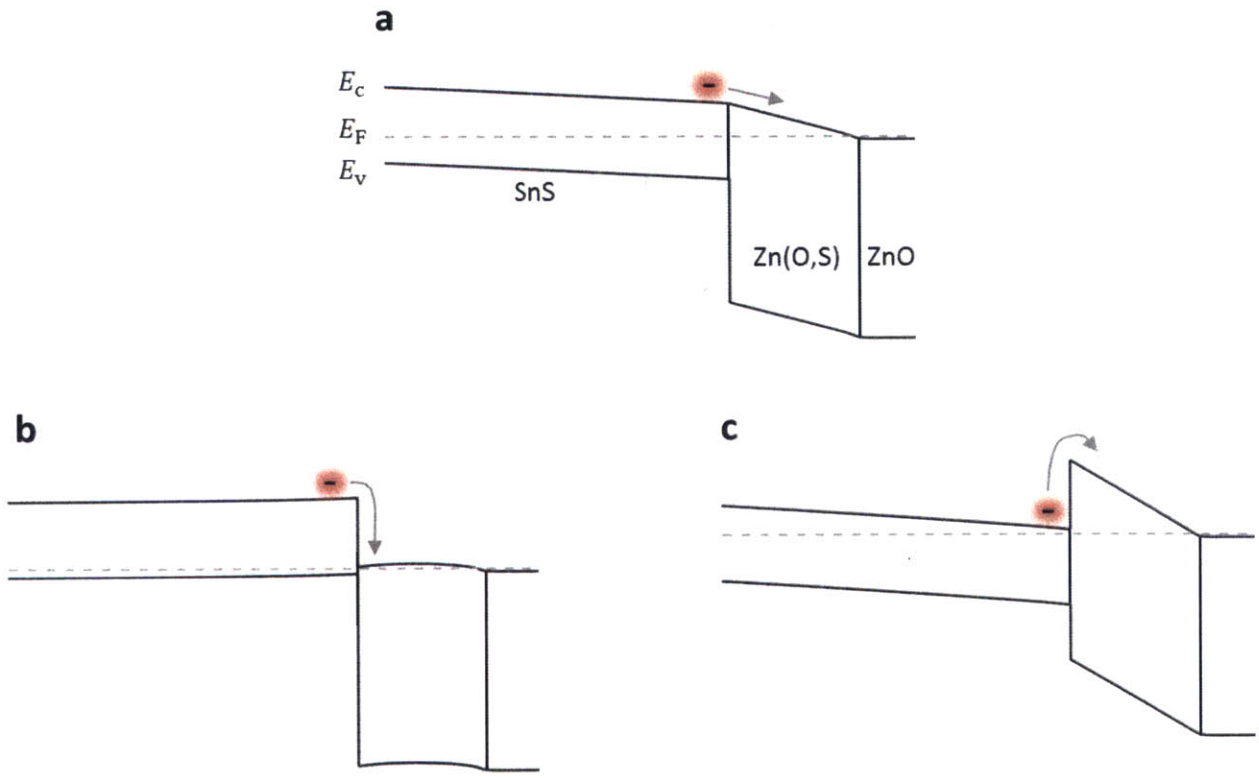

Figure 5-4. Energy band diagrams at zero bias for varying conduction band offsets between the SnS and Zn(O,S):N layers. Black lines refer to the conduction band position E_c and valence band position E_v, and the gray dotted line indicates the fermi level E_F. For clarity, band diagrams are drawn in the case of no illumination, with the understanding that the energetic differences between the SnS and Zn(O,S):N layers remain the same in the illuminated case. (a) For a conduction band offset of zero, electrons (red) see no energetic change going from SnS to Zn(O,S):N. (b) For a low SnS electron affinity, or equivalently a large negative conduction band offset, electrons must thermalize down to the lower conduction band edge of the Zn(O,S):N, resulting in a loss of voltage. (c) For a high SnS electron affinity, or equivalently a large positive conduction band offset, the flow of electrons is impeded by an energetic barrier at the interface, resulting in a loss of current.

As mentioned before, any diagonal of slope 1 on the contour plot is a line of constant $\Delta\chi$. Moving along the diagonal direction is thus equivalent to varying the electron affinity of the buffer layer relative to the SnS grains. This is exactly analogous to experimentally optimizing, or "tuning", the buffer layer conduction band position. In present-day SnS devices, for example, the Zn(O,S):N buffer layer conduction band position is tuned by varying the ratio of oxygen to sulfur content in the atomic layer deposition process; the conduction band position increases with a decreasing oxygen to sulfur ratio.[70,71,127] In practice, changing the buffer layer composition usually results in a change in the equilibrium carrier concentration in the buffer layer, which can have a significant effect on

the device performance.[71,73] However, the present work focuses on the effect of the conduction band position alone, and "tuning" of the buffer layer shall refer to tuning only the conduction band position.

Thus, in terms of device engineering, the relevant question is: given a SnS electron affinity disparity $\Delta\chi$ between the two grains, what is the maximum efficiency possible if the buffer layer conduction band position was optimized for that value of $\Delta\chi$? This may be found easily by identifying the path of maximum efficiency in Figure 5-3a as $\Delta\chi$ is increased. In this case, the path of maximum efficiency is a line from P1 to P2. The buffer-layer-optimized efficiency given a $\Delta\chi$ thus *always* occurs for a cliff offset at one of the grains, in the parallel model, because the decrease in efficiency due to the J_{SC} loss incurred by a spike offset (moving from P1 to P3) is greater than the decrease in efficiency due to the V_{OC} loss incurred by a cliff offset (P1 to P2).

Figure 5-5a more clearly shows how this buffer-layer-optimized efficiency varies with $\Delta\chi$. The efficiency is normalized to the global optimum of efficiency (P1). For the parallel model, the efficiency is highest when $\Delta\chi = 0$, and decreases monotonically as $\Delta\chi$ increases. The maximum electron affinity disparity expected for SnS, based on the aforementioned density functional theory calculations, is 0.9 eV.[25] At $\Delta\chi = 0.9$ eV, the optimized efficiency decreases by 21% relative to the global maximum. The optimized efficiency at $\Delta\chi = 0.9$ eV occurs at P2, where the efficiency loss is primarily due to a V_{OC} loss.

The simulated efficiencies in electron affinity parameter space for the 2D model (Figure 5-3d) are strikingly different qualitatively from those of the parallel model. Although the global maximum efficiency occurs in the same position at $\chi_1 = \chi_2 = 4.28$ eV, the path of maximum efficiency as $\Delta\chi$ increases now points in the direction of a spike offset (P3) rather than a cliff offset (P2). Moreover, the efficiency along this path of maximum efficiency does not change appreciably. This is more clearly seen by the blue curve in Figure 5-5a, which shows that as $\Delta\chi$ increases from 0 to 0.9 eV, the optimized efficiency decreases by no more than 2%. This striking robustness to the electron affinity disparity may be explained by examining the V_{OC} and J_{SC} for the 2D model.

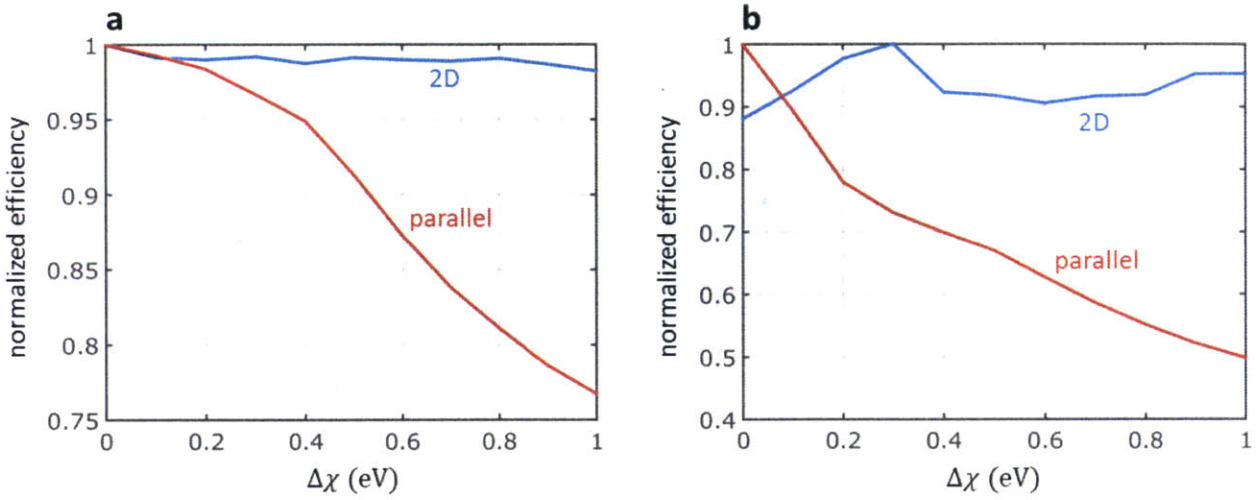

Figure 5-5. Normalized efficiency after buffer layer conduction band position optimization versus the electron affinity disparity between the two grains, for (a) the present-day scenario, and (b) the high-efficiency scenario. The red lines correspond to the parallel 1D model, while the blue lines correspond to the 2D model.

The V_{OC} of the 2D model (Figure 5-3e) looks qualitatively similar to that of the parallel model (Figure 5-3b). The same phenomenon as in the parallel model is at play here: as one electron affinity decreases, the conduction band offset becomes more of a cliff, resulting in a V_{OC} loss for that grain that dominates the total JV characteristics of the two-grain system.

In contrast, the J_{SC} of the 2D model (Figure 5-3f) looks strikingly different from that of the parallel model (Figure 5-3c). Most notably, moving from the global optimal efficiency (P1) to a spike offset region for one of the grains (P3) does not result in a decrease in J_{SC}. That is, the current-blocking effect observed in the parallel model is somehow mitigated. This behavior is investigated in more detail by analyzing the two-dimensional minority-carrier current flows in the two-grain system.

Figure 5-6a shows a two-dimensional contour plot of the magnitude of the electron current density J_e for the entire simulated device, for the case where $\chi_1 = 5.28$ eV and $\chi_2 = 4.08$ eV. At this point in electron affinity parameter space, the grain on the left should have a current-blocking spike offset at the SnS/Zn(O,S):N heterojunction, while the grain on the right should have a near-optimal offset. Figure 5-6b shows a larger view of the area denoted by the gray dotted box in Figure 5-6a, and the contour plot is overlaid with arrows showing the direction of J_e. Figure 5-6b shows that indeed, very little electron current flows

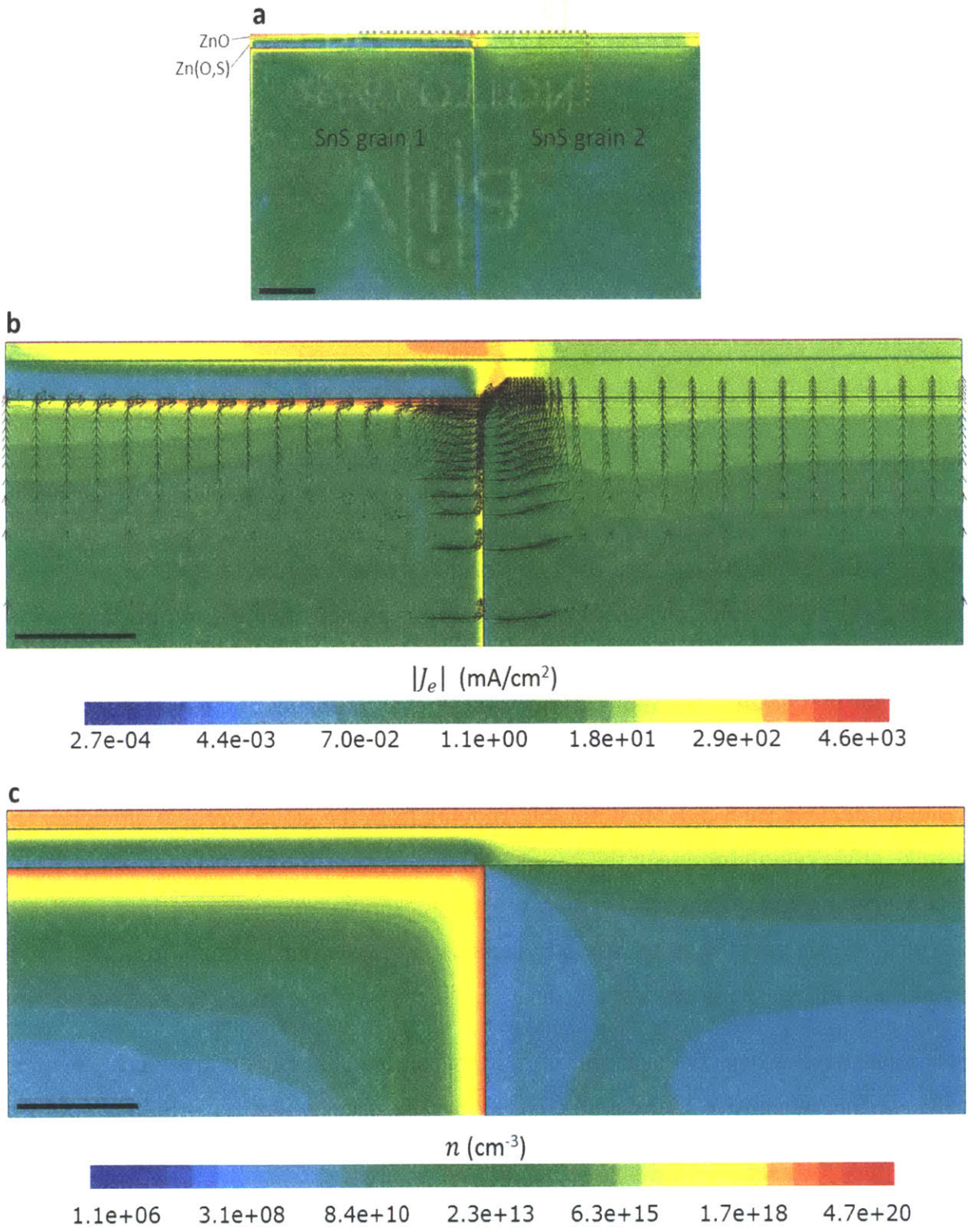

Figure 5-6. Contour plots for the 2D model with SnS electron affinities $\chi_1 = 5.28$ eV and $\chi_2 = 4.08$ eV. (a) Magnitude of the electron current density J_e. (b) Same, zoomed in on the gray dotted box area in (a), overlaid with arrows showing the direction of $-J_e$. (c) Electron density n for the same area as (b). Black scale bar indicates 250 nm.

through the SnS/Zn(O,S):N heterojunction on the left, where there is a current-blocking spike offset. However, there also exists another, distinctly two-dimensional effect. Electrons from the bulk of the left grain first travel to either the SnS/Zn(O,S):N heterojunction or the SnS/SnS heterojunction. Close to these interfaces, an inversion layer forms due to the disparate electron affinities on either side of the junctions, shown by the decrease in electron concentration in these areas (Figure 5-6c). These inversion layers provide electrons a high-conductivity path toward the triple junction where the two grains meet the Zn(O,S):N layer. At the triple junction, electrons cross into the Zn(O,S):N layer due to favorable energetics. Thus, because of lateral current, the electrons in the current-blocking grain that otherwise would have been lost in the parallel model are efficiently transferred to the Zn(O,S):N layer. The parallel model is thus insufficient to accurately model the effect of grain-to-grain electron affinity variation for the present-day case. When two-dimensional effects are taken into account, the device efficiency remains nearly constant for widely disparate electron affinities.

The results for the high-efficiency scenario are shown in Figure 5-7. Using the parallel model, the global efficiency maximum occurs at $\chi_1 = \chi_2 = 4.58$ eV (Figure 5-7a), which translates to a slight-spike offset at the SnS/Zn(O,S):N interface for both grains. Despite this difference, the qualitative characteristics of the efficiency, V_{OC}, and J_{SC} in electron affinity parameter space (Figure 5-7a-c) are similar to those using the parallel model in present-day scenario (Figure 5-3a-c). It remains true that as we move away from optimal towards a current-blocking (Figure 5-4c) or voltage-limiting (Figure 5-4b) case for one of the grains, the J_{SC} and V_{OC} decrease, respectively. However, quantitatively, the buffer-layer-optimized efficiency decreases more precipitously as a function of $\Delta\chi$(Figure 5-5b, red) relative to the present-day scenario. At $\Delta\chi = 0.9$ eV, the optimized efficiency decreases by 48% relative to the global optimum at $\Delta\chi = 0$. Thus, the parallel model tells us that the relative impact on device efficiency of grain-to-grain electron affinity variation is much greater in the high-efficiency scenario than in the present-day scenario.

However, the picture changes when using the 2D model. Most notably, the global optimal efficiency using the 2D model occurs at a nonzero $\Delta\chi$ of 0.3 eV, when $\chi_1 = 4.48$ eV and $\chi_2 = 4.78$ eV, or vice versa (Figure 5-7d). This occurs because the current-collecting benefit

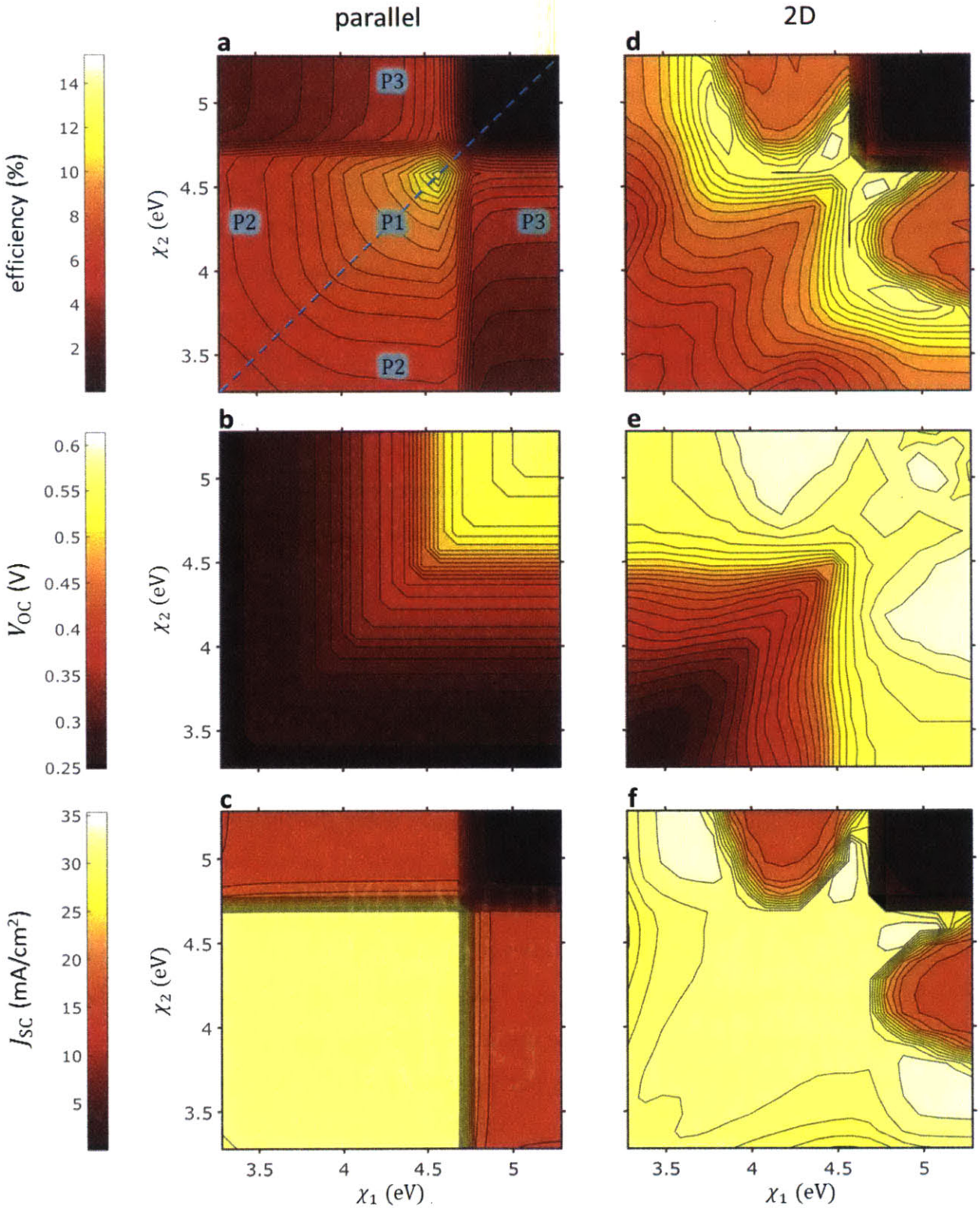

Figure 5-7. Contour plots of simulated efficiency, V_{OC}, and J_{SC} of high-efficiency case using the parallel grain model (a-c) and 2D grain model (d-f). Horizontal and vertical axes represent the electron affinity of each grain and are equivalent across all contour plots. Numbers in (a) denote cases of interest discussed in the text.

of the inversion layer induced at the SnS/SnS interface outweighs the slight loss in V_{OC} due to the mismatch in electron affinity. Much like the present-day scenario, however, the maximum-efficiency path as $\Delta\chi$ increases remains high in efficiency relative to the parallel model, as shown in Figure 5-5b by the blue curve. The optimized efficiency drops no more than 12% relative to the global optimum as $\Delta\chi$ increases from 0 to 0.9 eV (Figure 5-5b).

The V_{OC} and J_{SC} of the 2D model in the high-efficiency scenario (Figure 5-7e-f) also differ qualitatively from the 2D model in the present-day scenario. Most notably, the J_{SC} no longer exhibits robustness to change as we move from the global efficiency optimum toward P3 (Figure 5-7f). Instead, there is a precipitous drop in J_{SC} in the vicinity of P3. This is investigated further by again examining the two-dimensional current flow near this point. Figure 5-8 shows the magnitude of the electron density overlaid with arrows showing the direction of the electron flow, for the case where $\chi_1 = 5.28$ eV and $\chi_2 = 4.18$ eV. Evidently, in the left grain ($\chi_1 = 5.28$ eV), there is a significant flow of electrons downward toward the back contact through the inversion layer near the SnS/SnS interface. This reverse current is not observed in the present-day case because the minority-carrier lifetimes are too short to enable an appreciable current from the bulk to the inversion layer at the SnS/SnS interface. The high minority-carrier lifetime of the high-efficiency scenario makes the reverse current significant in the vicinity of P3, which explains the drop in J_{SC} near P3 (Figure 5-7f). As we move to the left from P3, the electron affinity of the non-current-blocking grain is decreased, thus making it more favorable for electrons to pass through the triple junction, and the J_{SC} is recovered. Thus, the mechanism of how the efficiency is robust to electron affinity variation is more complex in the high-efficiency case than in the present-day scenario.

For both the present-day and high-efficiency scenario, the 2D model results are drastically different from the parallel model results. Contrary to the parallel model, the 2D model more accurately tells us that the total device efficiency is relatively robust to the disparity in electron affinity between the two grains.

There are several caveats to note in generalizing this analysis. First, as mentioned in Section 5.2.1.2, the electron affinity for each grain is defined to be the same at the

SnS/Zn(O,S):N interface as it is at the SnS/SnS interface. In general, these two surfaces would likely be different crystal surfaces of SnS, and thus different electron affinities. Modifying the 2D model to take this account is a complex task and is not undertaken here.

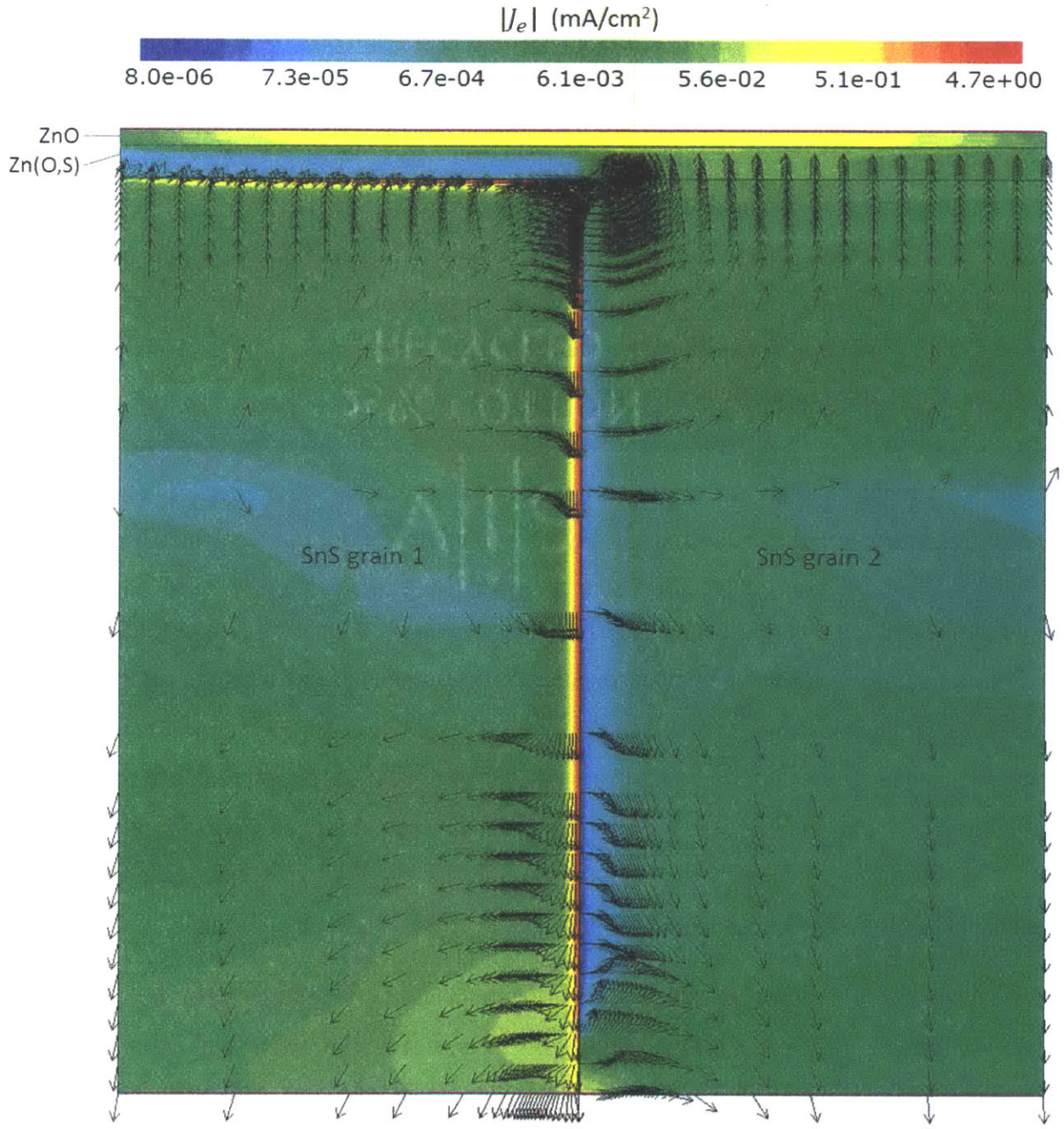

Figure 5-8. Magnitude of the electron current density J_e overlaid with arrows showing the direction of $-J_e$, computed using the 2D model for the high-efficiency scenario, with SnS electron affinities $\chi_1 = 5.28$ eV and $\chi_2 = 4.18$ eV. In this case, because of the high minority-carrier lifetime in the SnS, reverse currents to the back contact become significant.

However, the basic conclusion that lateral current makes the two-grain system robust to variation in electron affinity would not change. The presently simulated 2D cases are likely worst-case scenarios, in that very little current flows across the SnS/SnS grain boundary when the disparity of electron affinity is high. If, for example, the SnS electron affinities at the Zn(O,S):N interface are in a P3 scenario with one grain current-blocking, but the SnS electron affinities at the SnS/SnS interface are similar, then lateral grain-to-grain current, rather than a current through the vertical inversion layer, is expected. Thus, the electrons from the current-blocking grain would even more efficiently be transferred to the neighboring grain.

The second caveat is that the present models contain only two grains. While this is a useful model system to help understand the physics involved, especially with regards to lateral current effects, an actual SnS film would more accurately be modeled in three dimensions with each grain adjacent to four or more grains, and using a true grain orientation distribution to inform the distribution of electron affinities. However, again, I expect that the basic conclusion would remain the same in the three dimensional case: lateral current from current-blocking grains toward more optimal-electron-affinity grains would make the device more robust to variations in electron affinity.

5.3.2 SnS growth on graphene

The morphology of the of the SnS films on SiO_2 with and without graphene is strikingly different, as shown by the scanning electron micrographs in Figure 5-9. The SnS grains on the SiO_2 substrate (Figure 5-9a) appear platelet-shaped, consistent with the Wulff construction of SnS.[25] While many of the SnS grains near the substrate appear oriented with the basal plane parallel to the substrate, there are many off-angle grains that protrude above the basal-plane-oriented grains, resulting in a relatively rough surface morphology. The morphology changes with the addition of a graphene interlayer. The SnS film on a SiO_2/graphene substrate (Figure 5-9b) has a smoother surface morphology, presumably as a result of a lower fraction of grains with basal plane oriented non-parallel to the substrate.

These morphological results are consistent with the XRD spectra of the two samples, shown in Figure 5-10. Both the SiO_2/SnS and SiO_2/graphene/SnS samples exhibit a

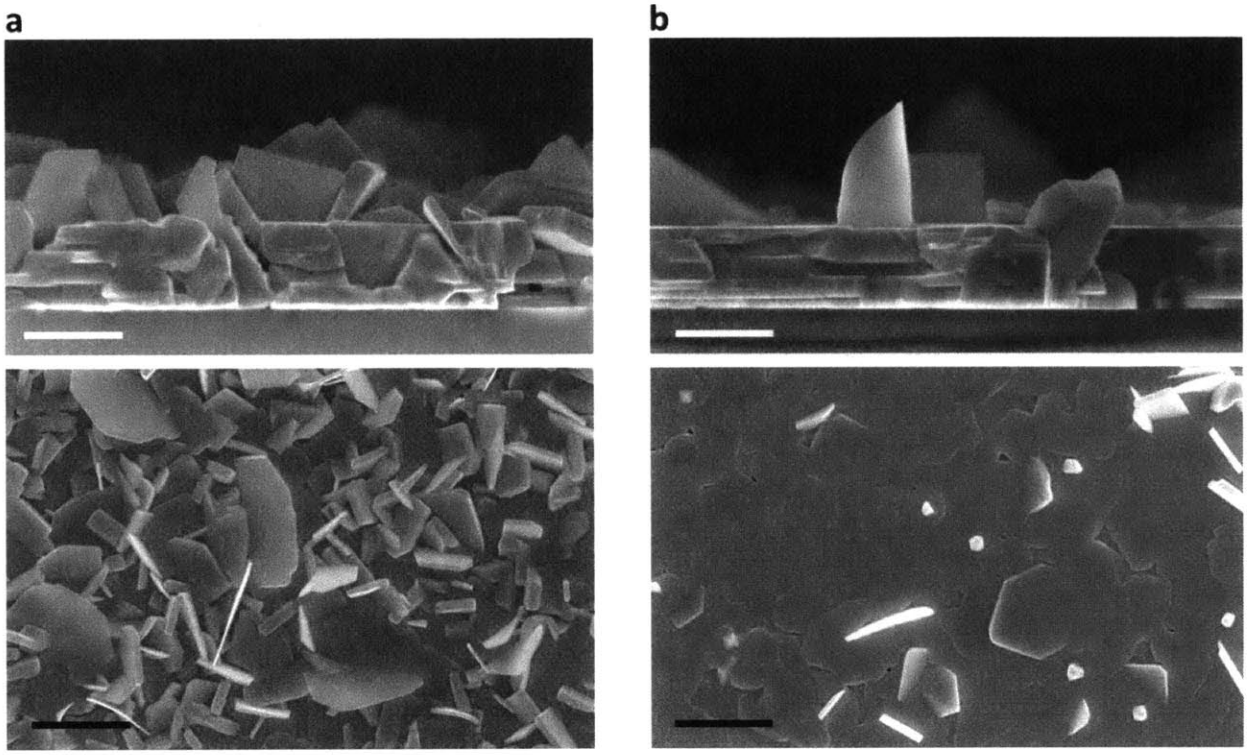

Figure 5-9. Cross-sectional (top) and plan-view (bottom) SEMs of (a) SiO_2/SnS and (b) SiO_2/graphene/SnS. White scale bars indicate 500 nm and black scale bars indicate 1 μm.

dominant (400) peak, indicating that the majority of grains in both cases are oriented with the basal plane parallel to the substrate. However, upon closer inspection of the XRD spectra, the SiO_2/graphene/SnS is found to have an even higher fraction of basal-plane-oriented grains than the SiO_2/SnS. This is shown by the inset in Figure 5-10, which allows comparison of the (111) peak to the (400) peak on a logarithmic scale. To within the error of the measurement, the SiO_2/graphene/SnS exhibits no evidence of any (111)-oriented grains, whereas the SiO_2/SnS shows a clear peak shoulder at the (111) peak location. This is only one example of an off-basal-orientation peak, but magnitudes of off-basal peaks for the graphene sample are found to be less than those of their non-graphene counterpart in all cases. This is consistent with the SEM results, which suggest that the off-basal grains are the cause of the relatively rough surface of the SiO_2/SnS sample. The graphene interlayer suppresses the growth of off-basal-oriented grains, which results in a smoother morphology of the SnS surface. Both the SEM and XRD results are also consistent with SnS growth on graphene in the literature.[121]

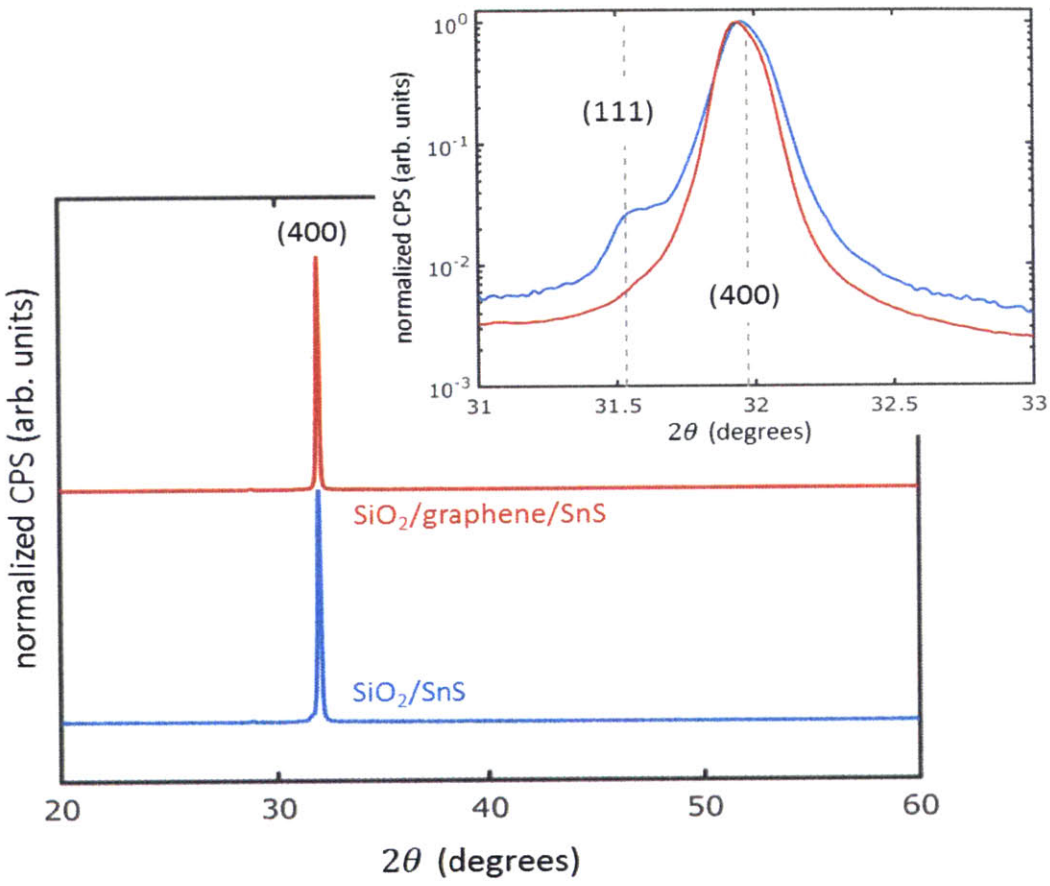

Figure 5-10. XRD spectra of the SiO_2/graphene/SnS (red) and SiO_2/SnS (blue) normalized to the (400) peak, vertically offset for clarity. Both samples exhibit high preference for the (400) orientation. The inset shows the same spectra on semilogarithmic axes near the the (400) peak, showing that the graphene suppresses the (111) orientation.

Figure 5-11 shows the normalized average excess-carrier concentration as a function of time for both samples, normalized to the maximum excess-carrier concentration of each sample. Note that the spikes in the signal at 30-33 ps and at 56-59 ps are artifacts due to multiple reflections off of optical elements upstream of the sample. Nevertheless, as a measure of the effective minority-carrier lifetime of the thin films, the time at which $\bar{n}(t)$ decays by $1/e$ of its maximum for each sample, $\tau_{1/e}$, is extracted. Note that this "effective" minority-carrier lifetime says nothing about the relative influence of bulk recombination versus surface recombination. Based on this measure, the SiO_2/graphene/SnS sample shows a marked increase in $\tau_{1/e}$ (41 ps) relative to the SiO_2/SnS sample (21 ps). Thus, the presence of the graphene interlayer causes not only a change in morphology and grain orientation distribution, but also the effective minority-carrier lifetime.

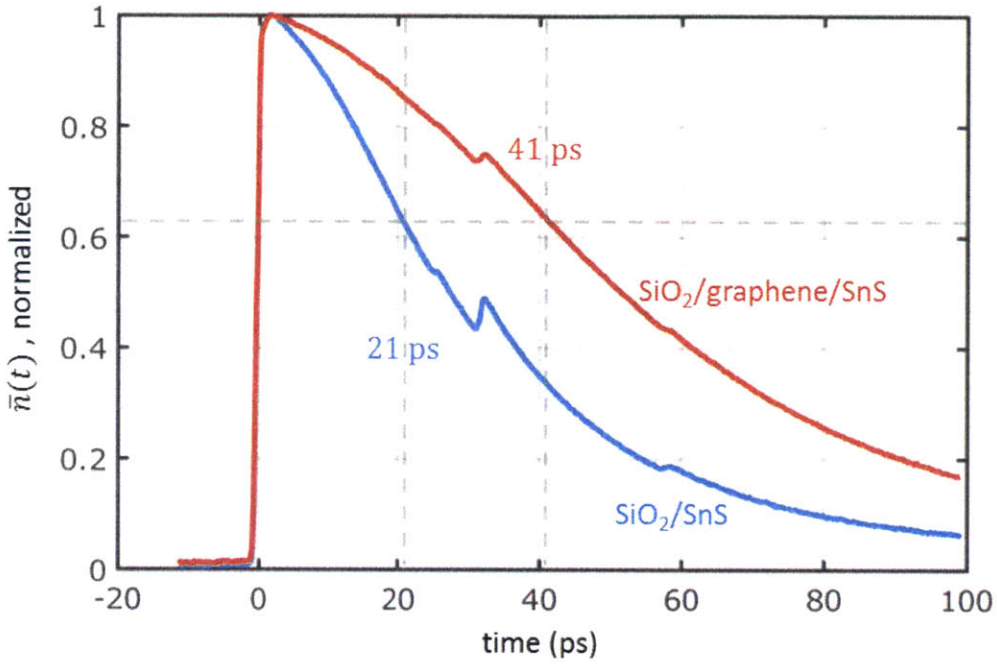

Figure 5-11. Transient terahertz absorption of the SiO_2/SnS sample (blue) and SiO_2/graphene/SnS sample (red), normalized to the peak absorption. The peak absorption corresponds to time = 0. The kinks at 30-33 ps and at 56-59 ps are artifacts due to multiple reflections off of optical elements upstream of the sample. The horizontal dotted line indicates $\bar{n}(t) = 1 - 1/e$, and the vertical dotted lines indicate where the blue and red curves intersect with the horizontal dotted line.

There are several mechanisms that may explain the increase in effective minority-carrier lifetime in the SiO_2/graphene/SnS sample. First, the bulk minority-carrier lifetime may be increasing due to a lower density of recombination-active extended structural defects. The SEM and XRD results suggest that grain orientation is more uniformly basal-plane-oriented in the graphene sample than in the non-graphene sample. This means that fewer high-angle grain boundaries are present in the graphene/SnS sample. Since high-angle grain boundaries may be more recombination active than other types, this lower density of high-angle grain boundaries in the graphene/SnS sample may partially explain its higher effective minority-carrier lifetime.

The effective minority-carrier lifetime may also increase because of a reduction of surface recombination at the SnS/substrate interface, the SnS/air interface, or both. Two effects may be at play in this case. First, if the surface recombination velocity at these interfaces is assumed to be equal between the two samples, then one would expect a lower recombination rate for the graphene/SnS sample, simply because the film on graphene has

a lower surface area. This is shown by the SEMs in Figure 5-9, where it is clear that while the SnS/substrate interfaces look equally smooth between the samples, the SnS/air interface for the SnS film grown without graphene has a higher surface area due to the protrusions of off-basal-oriented grains. Thus, the lower surface area of the graphene/SnS sample may explain the improvement in effective minority-carrier lifetime.

Another surface effect may come from the differences in surface recombination velocity at different crystal planes of SnS. The surface recombination velocity at the basal plane surface of SnS is expected to be less than that at other crystal planes because of the van der Waals bonding character at the basal plane. Like other layered-structure chalcogenides, the basal plane surface of SnS is intrinsically inert due to a lack of dangling bonds, which should result in a lack of the interface states normally present for a non-van-der-Waals surface.[26] Although the SnS/substrate interface appears to be dominated by the basal plane of SnS for both samples, the SnS/air interface is significantly different between the two samples. The smooth graphene/SnS sample has a SnS/air interface dominated by the basal plane, whereas the non-graphene sample has an SnS/air interface densely interspersed with off-basal surfaces because of the off-basal-oriented grains. Thus, the expected disparity in recombination activity between the basal plane and non-basal planes of SnS may account for the reduction of surface recombination for the graphene sample, leading to an increase in the effective minority-carrier lifetime.

The improvement in $\tau_{1/e}$ with the addition of a graphene layer on SiO_2 before SnS growth hints at a promising route toward uniformly oriented, low-structural-defect-density SnS films. However, to translate these learnings to a device performance enhancement with the present-day SnS device process, a conductive back substrate must be used. Thus, SnS is deposited on the same $Si/SiO_2/Mo$ substrates used in the current device process, with and without a graphene layer, with the intent of achieving similar-quality SnS films on Mo/graphene as for SiO_2/graphene. It is found that the difference in morphology caused by the graphene interlayer is even more pronounced between the SnS on the Mo substrate (Figure 5-12a) and that on the Mo/graphene substrate (Figure 5-12b). The SnS film on Mo exhibits a dense packing of grains of order 100 nm, with grain shapes more isotropic than the thin platelets on SiO_2. In contrast, the SnS film on Mo/graphene consists of basal-

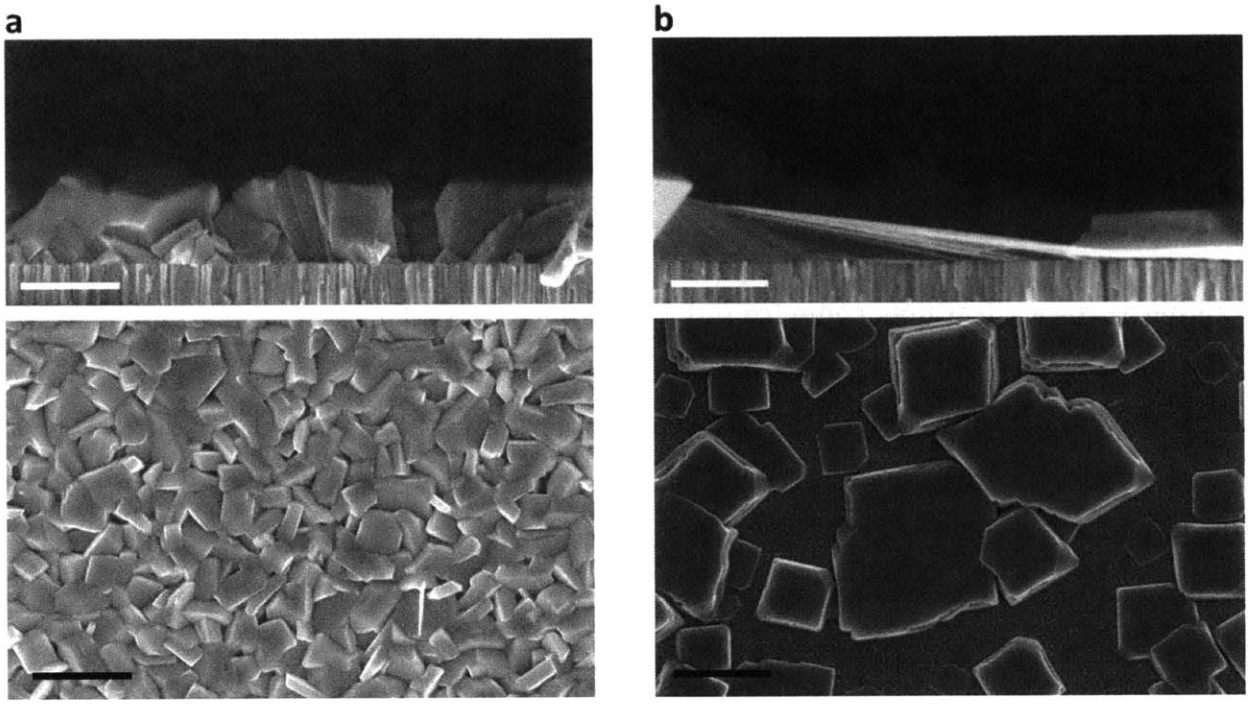

Figure 5-12. Cross-sectional (top) and plan-view (bottom) SEMs of (a) $Si/SiO_2/Mo/SnS$ and (b) $Si/SiO_2/Mo/graphene/SnS$. White scale bars indicate 500 nm and black scale bars indicate 1 μm.

oriented, platelet-shaped grains or groups of grains of order 1 μm, and the grains are separated by large (~1 μm) areas of bare substrate.

That the introduction of graphene on Mo has a more pronounced effect than that on SiO2 can be explained by the difference in surface energy expected between Mo and Mo/graphene, versus SiO_2 and SiO_2/graphene. The SiO_2 surface has an intrinsically low free surface energy < 1 J/m^2,[128] while the Mo surface has a relatively high free surface energy in the range 2-4 J/m^2.[129] The introduction of a graphene layer thus may lower the surface energy of the Mo substrate to a greater extent than it does on SiO_2, resulting in a more drastic difference in SnS nucleation density. However, the SnS morphology on Mo/graphene is also drastically different than that on SiO_2/graphene. The SnS on Mo/graphene seems to have a lower nucleation density that that on SiO_2/graphene, which disagrees with the trend in free surface energy of the bare Mo and SiO_2 surfaces. This difference may be due to the fact that the bare Mo surface is more rough than the SiO_2 surface. The Mo surface is terminated by crystal facets that are not parallel to the substrate plane. It may be that the graphene does not conform to the Mo surface, and rather rests on

the vertices of the Mo grains. This would drastically decrease the effect of the underlying Mo on the effective surface energy of the Mo/graphene, such that the effective surface energy of the Mo/graphene surface is *lower* than the effective surface energy of the SiO_2/graphene. This in turn could lead to the lower nucleation density of SnS on the Mo/graphene relative to the SiO_2/graphene that is observed.

The discontinuous nature of the Mo/graphene/SnS film is not conducive to device fabrication, since the *n*-type buffer layer and subsequent contact layers would, after deposition onto the discontinuous SnS film, make direct contact with the Mo back contact, leading to catastrophic shunting. A continuous SnS film may be obtained by further optimization of the SnS growth parameters, such as reducing the substrate temperature or increasing the deposition rate. This optimization is not pursued in the present work, but the striking change in morphology caused by the graphene layer observed here points at a potentially fruitful avenue for future device engineering efforts.

5.4 Conclusion

In summary, this chapter explored two avenues through which the anisotropic properties of SnS may impact future device performance. In the first avenue, the effect of the anisotropic electron affinity of SnS on device performance is quantified, attempting to take into account a laterally varying electron affinity due to a wide SnS grain orientation distribution in a device. It is found that the more commonly used parallel-diode model misses a key physical mechanism that makes SnS devices relatively robust to these lateral variations in electron affinity. In particular, lateral current enabled by a high-conductivity inversion layer funnels current from grains with sub-optimal band alignment at the SnS/Zn(O,S):N interface toward grains with near-optimal electron affinity, recovering the loss in current expected if the grains were connected simply in parallel. However, in general, achieving a uniform electron affinity, and thus uniform grain orientation distribution, is still deemed necessary to achieve the highest efficiency.

In the second avenue, I explore the potential for harnessing the anisotropic surface energy of SnS to grow films that are simultaneously uniform in grain orientation and low in

recombination-active defect density. In particular, the impact of a van der Waals-terminated substrate, graphene, on the SnS film morphology and the minority-carrier properties of the film are measured. The resultant films grown on graphene are highly textured with the basal plane oriented parallel to the substrate, which is consistent with the literature. More significantly, the presence of the van der Waals substrate enhances the effective minority-carrier lifetime of SnS. The enhancement in minority-carrier lifetime may be due both bulk and surface effects, such as a reduction of recombination-active grain boundaries in the bulk of the film, or the reduction of surface area leading to a decrease in total surface recombination. Attempts to use the graphene interlayer with a device-relevant substrate, molybdenum, show promise in terms of morphology, but further growth optimization is necessary to fully realize the benefit of a van der Waals-bonded interlayer in a SnS-based device.

Chapter 6

Toward *in-situ* optimization of film growth**

This thesis focuses on determining the structural defects in SnS that limit its device efficiency potential – from grain boundaries, to extended structural defects, to point defects, to structural inhomogeneity. Once the most detrimental defects are known, we would like to understand the physical mechanisms governing the formation and evolution of those defects during film growth and processing (*e.g.*, annealing), and then to optimize the film growth and processing parameters to reduce the density of those types of defects. In general, the cycle of learning and optimization for a given candidate polycrystalline thin-film absorber can be slow. The cycle typically consists of growing and processing a film, performing structural defect and electrical characterization, and then repeating with modified growth and processing parameters to ultimately reduce the density of detrimental defects and improve electrical performance. This cycle is inherently limited both in speed and the amount of learning per cycle, since the defect characterization is done *ex-situ*.

** The contents of this chapter are adapted from a previously published journal article in *Review of Scientific Instruments*,[100] the publisher of which, American Institute of Physics, has granted permission for authors to re-publish in a thesis.

Expediting this cycle of learning and optimization requires *in-situ* characterization of micro- and nanoscale defects in polycrystalline thin-film materials under realistic processing conditions. With *in-situ* characterization, it is possible to observe defect formation and evolution *during* the growth and processing steps, allowing us to explore the film growth and processing parameter space much more efficiently toward reduced defect density and high-quality films, while gaining more information about micro- and nano-scale defect physics. To this end, the present work focuses on the design and development of a sample stage for the purpose of *in-situ* characterization of nano-scale defects in thin-film PV materials.

The imaging of nanoscale features requires high-resolution techniques such as transmission electron, scanning electron, or scanning X-ray microscopy. Nanoscale synchrotron-based hard X-ray fluorescence (XRF) spectromicroscopy is particularly well-suited to study compositional aspects of defects in compound semiconductors because it allows for elemental concentration mapping at defect sites.[130] However, *in-situ* characterization of defects using this technique presents a number of challenges. Mimicking actual process conditions requires fast temperature ramp rates (300°C/min) up to temperatures of 600°C, often under corrosive atmospheres such as H_2S or H_2Se. The small length scales of the defects of interest (~100 nm) also necessitate accurate predictability of the sample thermal drift during heating and cooling to enable tracking of individual defects.

A variety of temperature stages with similar constraints has been previously developed for electron[131–134] and X-ray microscopes[135,136] with outstanding performance in certain application areas. However, these stages are not optimized to simultaneously accommodate the large solid angle needed for the detection of XRF photons, the mounting of large, electrically working devices, and the tracking of features with sub-micrometer resolution. Instead, stages optimized for transmission microscopy require extensive sample preparation, which may render the sample misrepresentative of the material of interest. For example, sample preparation for scanning transmission X-ray microscopy involves preparing a thin slice of the thin-film via focused ion beam milling, which may alter the material properties. Therefore, these stages are not optimal for studying thin-film

PV devices. Of the *in-situ* stages with ambient control tested at nanoprobe XRF beamlines,[137-139] the sample-mounting configuration often results in thermal drift and sample stick-slip effects that are inauspicious for detailed and highly reproducible measurements.

In this work, I design and build an *in-situ* temperature stage for hard X-ray micro- and nanoprobes, optimized to study defect kinetics in thin-film solar cells under actual processing conditions, and designed to require minimal sample preparation. The stage is capable of maintaining or flowing non-oxygen-containing atmospheres including H_2S and H_2Se. Temperature ramp rates of up to 300°C/min are achieved, with a maximum sample temperature of 600°C. To demonstrate its functionality, the stage is used for synchrotron X-ray fluorescence microscopy of $CuIn_xGa_{1-x}Se_2$ (CIGS) thin films. Predictable sample thermal drift for temperatures 25–400°C is measured, allowing features on the order of the resolution of the measurement technique (125 nm) to be tracked while heating.

The content of this chapter has been previously published in Review of Scientific Instruments.[140] My main contributions to this work are the design and assembly of the stage, the calibration of the stage, the operation of the stage for demonstration on CIGS thin films, and the analysis of feature displacement data. The sample preparation, some of the machining of stage components, acquisition of X-ray fluorescence data, and the analysis of atomic concentration distributions are done by my co-authors.

6.1 Design of *in-situ* temperature stage for X-ray spectromicroscopy

6.1.1 Stage design

Figure 6-1 shows the major features of the *in-situ* sample stage. The outside assembly, which makes up the walls of sample chamber, consists of two phenolically-impregnated graphite plates (MWI) with a quartz tube in between the plates. Graphite is chosen because of its high-temperature tolerance, non-reactivity with various corrosive atmospheres including H_2S and H_2Se, and low thermal expansion coefficient. Phenolic impregnation of

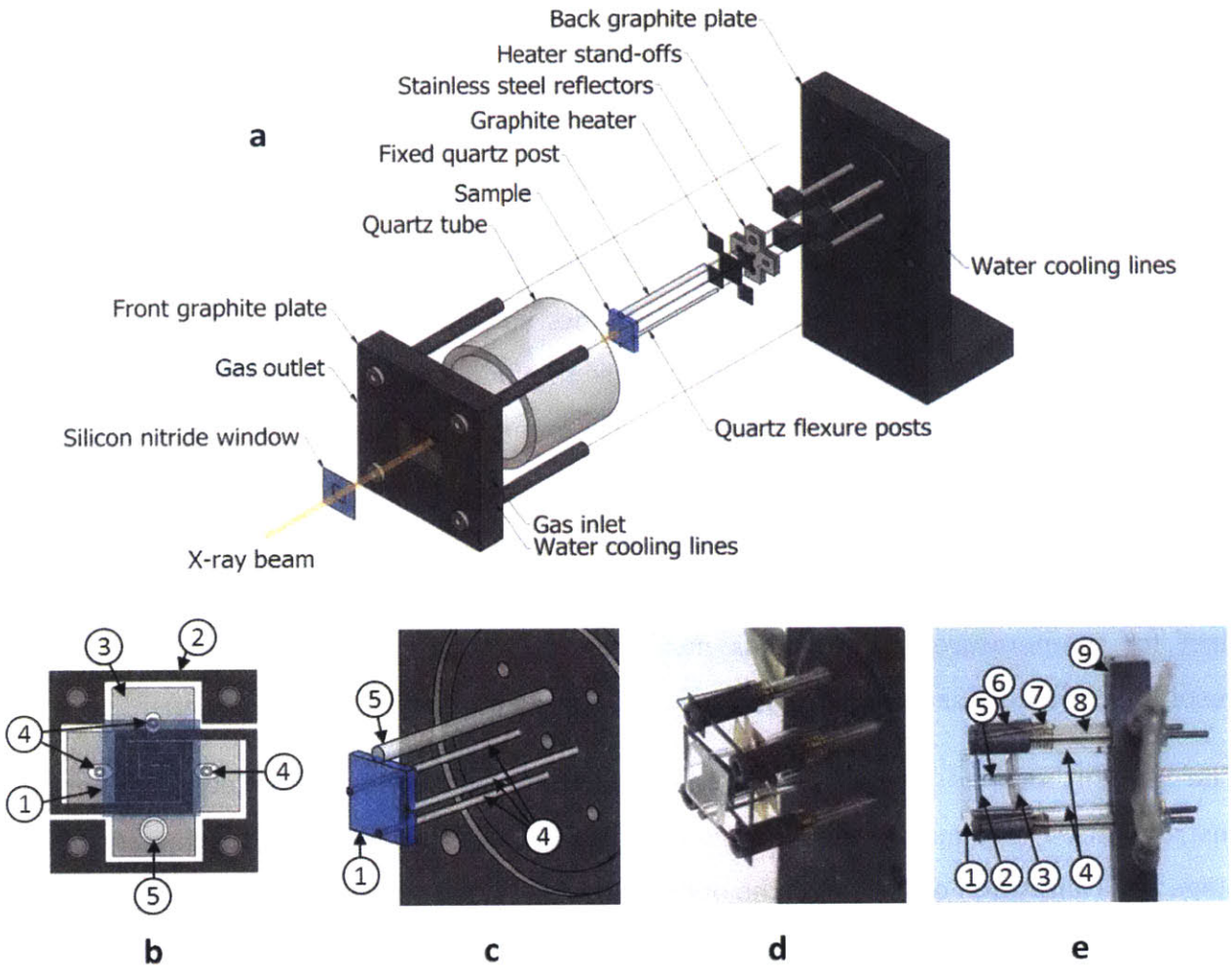

Figure 6-1. Schematics and pictures of in-situ stage. (a) Exploded isometric view of all important components of the stage. (b) Sample-facing view of interior components. 1: sample; 2: graphite heater; 3: stainless steel (SS) reflector; 4: quartz flexures; 5: fixed quartz post. (c) Close-up isometric view showing only the back plate, sample (blue), and sample-mounting post and flexures. (d) Photograph of internal components. (e) Photograph of internal components in profile view. 6: graphite contact post; 7: SS spring for capturing graphite heater; 8: quartz-sheathed SS rod for electrical leads to graphite heater.

the graphite ensures that the graphite is gas-impermeable for graphite temperatures up to 180°C, above which phenolic evaporates. In order to keep the graphite temperatures below 180°C, chilled water is flowed through horizontal channels bored through both plates. The water flows via gravity from a reservoir located 2 m above the sample stage. The exhaust water from the stage is deposited into a second reservoir below the stage. A peristaltic pump then drives water from the bottom reservoir back to the top reservoir through a water-water heat exchanger, completing the closed-cycle water system. A gravity-fed water

system was chosen to minimize the possibility of transferring pump-induced vibrations to the sample stage.

The front graphite plate includes an X-ray-transparent Si_3N_4 window of size 5 mm × 5 mm and thickness 500 nm, on a Si substrate of size 12.5 mm × 12.5 mm × 0.5 mm. For hard X-rays above 4 keV, the X-ray transmittance is above 95%.

The inside of the sample chamber contains the heater and sample-mounting mechanism. Four quartz-sheathed electrical leads double as mechanical posts which hold a laser-cut graphite (G370) heater (Figure 1b, d, e). Quartz sheathing protects the electrical leads from corrosion and prevents contamination of the sample due to out-gassing of corrosion products. The graphite heater is 200 μm thick and is cut into a spiral pattern with a resistance ranging from 80–100 Ω. Graphite is chosen as the resistive element for heating again because of its high temperature tolerance. The thin sheet geometry of the heater also helps in keeping the thermal mass small, allowing temperature ramp rates of 300°C/min. It is observed that the graphite heater readily oxidizes in oxygen-containing atmospheres for sample temperatures above 300°C, so only non-oxygen-containing atmospheres can be used for this design.

A central quartz-sheathed thermocouple post measures the temperature at a distance < 1 mm below the heater surface, providing temperature feedback to the temperature controller. Similar to the heater posts, the quartz sheathing protects the thermocouple from corrosion and prevents contamination of the sample due to the corrosion.

Laser-cut 304 stainless steel plates of thickness 100 μm are mounted below the heater to limit radiative losses towards the back plate. The plates are cut to provide clearance for the sample-mounting mechanism and central quartz-sheathed thermocouple.

The sample-mounting mechanism is designed to capture a 10 mm × 10 mm × 1.6 mm sodalime glass substrate, and consists of one thick quartz post (2 mm outer diameter, 1 mm inner diameter) and three thinner quartz posts (1 mm outer diameter, 0.8 mm inner diameter) arranged in a square pattern. The thick quartz post (or "fixed" post) remains immobile, while the three thinner posts (or "flexures") are designed to bend. The sample

substrate is slid between the four posts such that the substrate is captured along three side edges by the flexures, and on the fourth edge by the fixed quartz post. A custom hand tool is used to push on the corners of the sample surface and slide the sample along the posts. The tool is mechanically stopped by the tops of the quartz-sheathed electrical posts, ensuring repeatable sample height and tilt relative to the back graphite plate. The spring force due to the bending of the flexures keeps the substrate in place. This flexure design is used to eliminate stick-slip effects as the substrate is heated, as stick-slip at the interface between the substrate and the sample-mounting mechanism results in irreproducible jumps in substrate position at the micrometer scale. With the flexure design, the flexures continuously bend to accommodate the thermal expansion of the substrate as it is heated. At the same time, the point at which the substrate meets the fixed post serves as a fixed spatial reference point during heating. While this design does not provide kinematically exact constraint in the plane of the sample due to rotation about the fixed post, this is not a concern since there are no external loads on the sample after mounting it onto the stage (see next section for discussion of kinematic constraint).

The only sample preparation necessary for this stage design is to dice the specimen to 10 mm × 10 mm (± 0.1 mm), and to attach a 10 mm × 10 mm × 0.2 mm graphite sheet (G370) to the back of the substrate using a high-temperature thermally conductive cement (Omegabond 700). The graphite backing acts as an efficient absorber of radiative heat delivered by the heater.

6.1.2 In-plane kinematic constraint of the sample mount

The sample mount system consists of one thick quartz post (2 mm outer diameter, 1 mm inner diameter), and three thinner quartz posts (1 mm outer diameter, 0.8 mm inner diameter). All four posts are fixed to the back graphite plate by sliding them through close-fit through-holes in the graphite plate and applying silicone RTV sealant (Dow Corning 734) at the base. The posts extend 31 mm beyond the surface of the back graphite plate, and the sample is mounted flush with the free ends of the posts. The posts are thus modeled as cantilever beams with a concentrated load F at the free end, with maximum deflection d at the free end. The maximum deflection for such a system is $d = \frac{FL^3}{3EI}$, where L

is the length of the beam, E is the elastic modulus, and I is the second moment of area of the beam's cross-section. The bending stiffness of one post is thus $k = \frac{F}{d} = \frac{3EI}{L^3}$. For an annular cross-section of inner radius r_1 and outer radius r_2, $I = \frac{\pi}{2}(r_2^4 - r_1^4)$, which yields $k = \frac{3\pi E}{2L^3}(r_2^4 - r_1^4)$. Substituting 73 GPa for the elastic modulus of fused silica,[141] along with the relevant geometrical quantities, the bending stiffness of the thin posts is calculated to be $k_\mathrm{f} = 6.8 \times 10^3$ N/m, while the bending stiffness of the thick post is $k_\mathrm{p} = 1.7 \times 10^5$ N/m. Because $k_\mathrm{p} \gg k_\mathrm{f}$, I assume that the thick post is fixed in all subsequent calculations.

We now consider the stiffness of the sample mount system for an in-plane external load centered on the sample. Figure 6-2a shows a top view of the sample and sample mount system, with the x and y axes defined parallel to the sample edges, and the origin at the point of contact between the fixed post and the sample. The flexures A, B, and C are each deflected a distance d and make point contacts to three edges of the sample. The magnitude of the force imparted by each flexure to the sample is $F = k_\mathrm{f} d$, in a direction parallel to the deflection. With no external loads as in Figure 6-2b, the forces imparted by flexures A and C cancel, while the force imparted B is canceled by the normal force at the fixed post.

Consider a load P_y in the $+y$ direction centered on the sample, as shown in Figure 6-2c. Assuming no slip at the flexure-sample contacts, all three flexures are deflected in the $+y$ direction by a small distance Δy, while the sample loses contact with the fixed post. We now must have force balance in the y direction:

$$0 = \sum F_y$$
$$0 = P_y - F_{\mathrm{A},y} - F_{\mathrm{B},y} - F_{\mathrm{C},y}$$
$$0 = P_y - k_\mathrm{f}\Delta y - k_\mathrm{f}(d + \Delta y) - k_\mathrm{f}\Delta y = 0$$
$$P_y = k_\mathrm{f} d + 3k_\mathrm{f}\Delta y$$

Thus, for a load $P_y > k_\mathrm{f} d$ centered on the sample and in the $+y$ direction, the effective stiffness of the system is $k_y = \frac{P_y}{\Delta y} = 3k_\mathrm{f}$.

Now consider a load P_x in the $+x$ direction, as shown in Figure 6-2d. If we assume no slip at each of the sample edges, the sample will rotate about the fixed post contact. The load P_x thus imparts a torque $T_P = P_x\left(\frac{s}{2}\right)$ about the fixed post contact, resulting in a small rotation $\Delta\theta$. The torque T_P must be balanced by the torque imposed by the flexures after a small rotation $\Delta\theta$. Using the small angle approximation, we have

$$0 = \sum T$$

$$0 = T_P + F_{A,x}\left(\frac{\sqrt{2}}{2}\right)\left(\frac{s}{\sqrt{2}}\right) - F_{A,y}\left(\frac{\sqrt{2}}{2}\right)\left(\frac{s}{\sqrt{2}}\right) - F_{B,x}s - F_{C,x}\left(\frac{\sqrt{2}}{2}\right)\left(\frac{s}{\sqrt{2}}\right) - F_{C,y}\left(\frac{\sqrt{2}}{2}\right)\left(\frac{s}{\sqrt{2}}\right)$$

$$0 = T_P + k_f\left(d - \frac{s}{2}\Delta\theta\right)\left(\frac{\sqrt{2}}{2}\right)\left(\frac{s}{\sqrt{2}}\right) - k_f\left(\frac{s}{2}\Delta\theta\right)\left(\frac{\sqrt{2}}{2}\right)\left(\frac{s}{\sqrt{2}}\right) - k_f(s\,\Delta\theta)s$$

$$- k_f\left(d + \frac{s}{2}\Delta\theta\right)\left(\frac{\sqrt{2}}{2}\right)\left(\frac{s}{\sqrt{2}}\right) - k_f\left(\frac{s}{2}\Delta\theta\right)\left(\frac{\sqrt{2}}{2}\right)\left(\frac{s}{\sqrt{2}}\right)$$

$$0 = T_P - 2k_f s^2\Delta\theta$$

$$T_P = 2k_f s^2\Delta\theta$$

For small angles, the displacement in the x direction of the sample center is $\Delta x = \left(\frac{s}{2}\right)\Delta\theta$, so

$$T_P = 2k_f s^2\Delta\theta$$

$$P_x\left(\frac{s}{2}\right) = 2k_f s^2\Delta x\left(\frac{2}{s}\right)$$

$$P_x = 8\,k_f\Delta x$$

Thus, for a load P_x centered on the sample and in the $+x$ direction, the effective stiffness of the system is $k_x = \frac{P_x}{\Delta x} = 8k_f$. Substituting the previously calculated value for k_f yields the effective stiffnesses

$$k_y = 2.0 \times 10^4\ \text{N/m}$$

$$k_x = 5.4 \times 10^4\ \text{N/m}$$

Evidently, the in-plane stiffnesses are of the same order of magnitude, and following the principles of exact constraint design, this gives us adequate constraints without overconstraining the system.[142] We also note that the above stiffness equations hold even after a stick-slip event at the flexure-sample interface.

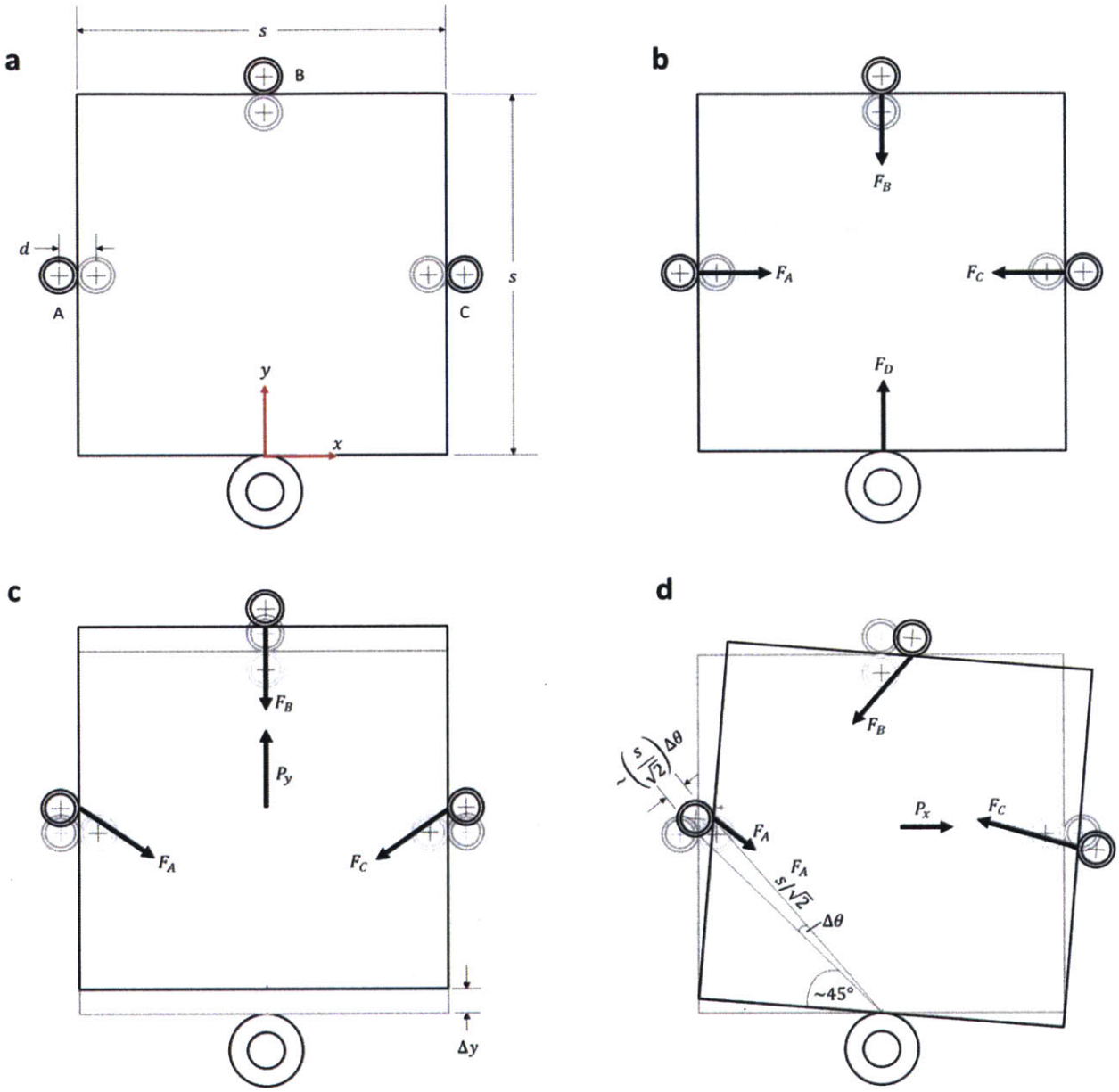

Figure 6-2. (a) Top view of the sample (square of side length s) mounted in the stage consisting of flexures A, B, and C and the fixed post at the bottom. The coordinate system is defined in red. Each flexure is deflected a distance d from its initial unloaded position (initial position shown in grey). (b) The normal forces imparted by the flexures and fixed post cancel in the case of no external loads. (c) An external load P_y in the $+y$ direction, centered on the sample face, results in a displacement Δy. (d) An external load P_x in the $+x$ direction, centered on the sample face, results in a rotation about the fixed post contact.

6.2 Demonstration on test-case thin-film PV absorber: CIGS

6.2.1 Materials and Methods

To test the stage, X-ray fluorescence spectromicroscopy are performed on CIGS thin-films at beamline 2-ID-D at the Advanced Photon Source. This beamline is outfitted with a nano-positioning stage, zone plates for X-ray focusing, and an order-sorting aperture to prevent unfocused X-rays from reaching the sample. The setup enables spatial resolutions on the order of 100 nm or better depending on the focusing optics used.[143] The *in-situ* stage is attached to the nano-positioning stage at the beamline with a custom aluminum adapter plate. For this experiment, nitrogen gas is flowed through the *in-situ* chamber at 10 sccm. The X-ray energy is 12.8 keV, just above the *K*-edge of selenium. The angle between the incident beam and the sample surface is 75°, and the angle between the incident beam and the detector is 43°. The sample temperature is first calibrated by pyrometry on a specially prepared substrate. The substrate used for the temperature calibration is identically prepared to ones used for samples, except that the upstream side, which for normal samples has the thin-film deposited onto it, is covered by a second graphite sheet identical to the graphite sheet on the backside. The graphite front provides a material of known emissivity with which to calibrate the pyrometer (Omega OS53x-CF). The substrate surface temperature is measured by pointing the pyrometer at the substrate face through the Si_3N_4 window of the stage. The pyrometer is insensitive to absorption in the thin Si_3N_4 window, but the spot size of the pyrometer is found to slightly overlap with the Si window frame. For this reason, the temperatures reported here are lower bounds. The temperature is calibrated under operating conditions, except without the incident X-ray beam. The additional heating due to the incident X-ray beam is negligible: assuming fast heat distribution in the sample (no local heating) and a photon beam of 10^9 photons/sec (each photon at 10 keV) that is fully absorbed by a 1 cm^2 thin-film solar cell on 1.6 mm thick glass, the beam leads to an additional heating rate on the order of 10^{-5} K/s if no heat transfer from the cell to the environment is provided. During the calibration, it is found that temperature stabilization of better than 1°C requires a settling time of 15 minutes or less, both for the temperature ramps up and down. Therefore, we waited 15 minutes after

setting a new temperature value for thermal stabilization of the calibration sample or of the sample of interest.

Once the temperature is calibrated, sample of interest is mounted into the *in-situ* stage. The sample temperature is incrementally increased, waiting 15 minutes for the temperature to stabilize at each new temperature. Sample features revealed through contrast in the measured XRF signal are tracked by alternating between large-area, coarse scans (6 μm × 10 μm, 200 nm step size) which enable a rough location of the feature after the expected thermal drift, and small-area, fine scans (4 μm × 6 μm, 125 nm step size) that allow a more accurate location of the feature. Quantitative atomic concentrations are then extracted from the XRF maps using a multicomponent stack analysis,[144] and correction for drift of the order-sorting aperture are taken into account.

6.2.2 Results and Discussion

Figure 6-3 shows processed XRF maps of the evolution and tracking of a feature as a function of sample temperature. The fact that we can resolve feature contrast as small as the resolution of the scan indicates that vibration-induced blurring of the image is limited to within the resolution of the scan. Figure 6-4a shows the displacement of a tracked feature as measured by the fine scans, for increasing sample temperature up to 400°C. Temperatures beyond 400°C resulted in losing track of the feature, possibly due to a microstructural change in the sample. The x and y directions are orthogonal in the plane of the substrate, defined in Figure 6-4b. There are several observations to note. First, we observe no discontinuities in displacement in either the x or y directions. This indicates that as the substrate temperature rises and the substrate expands, the quartz flexures bend without slip against the substrate edges. As mentioned previously, minimizing slip between the sample mount and the sample is key to achieving predictable feature displacement.

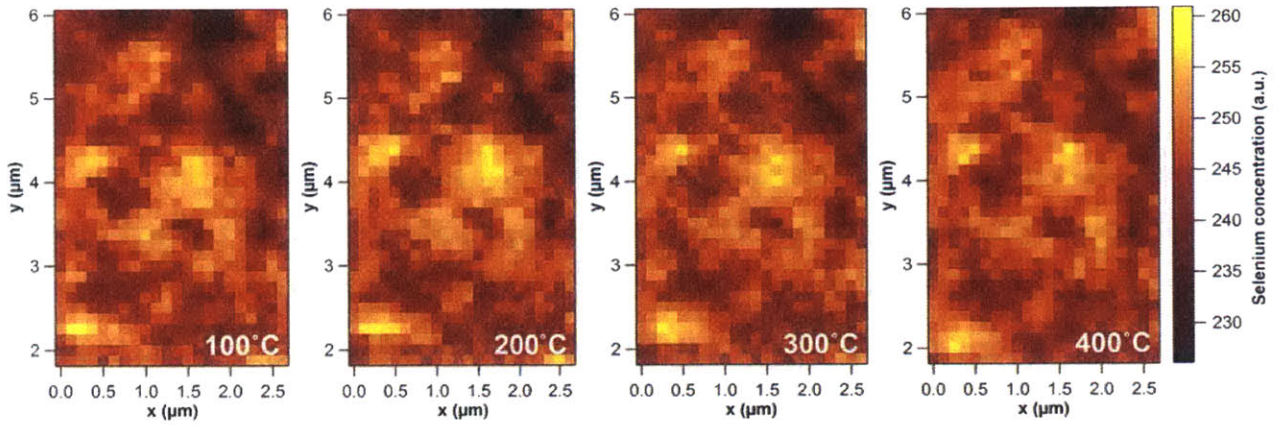

Figure 6-3. Maps of selenium concentration, measured by X-ray fluorescence (selenium *K* lines) at different sample temperatures using the *in-situ* heating stage. The maps are re-centered in the X-ray field of view at each temperature step to take into account the drift due to thermal expansion of the substrate. The same features can be seen at all temperatures, showing the excellent tracking capabilities of the heating stage.

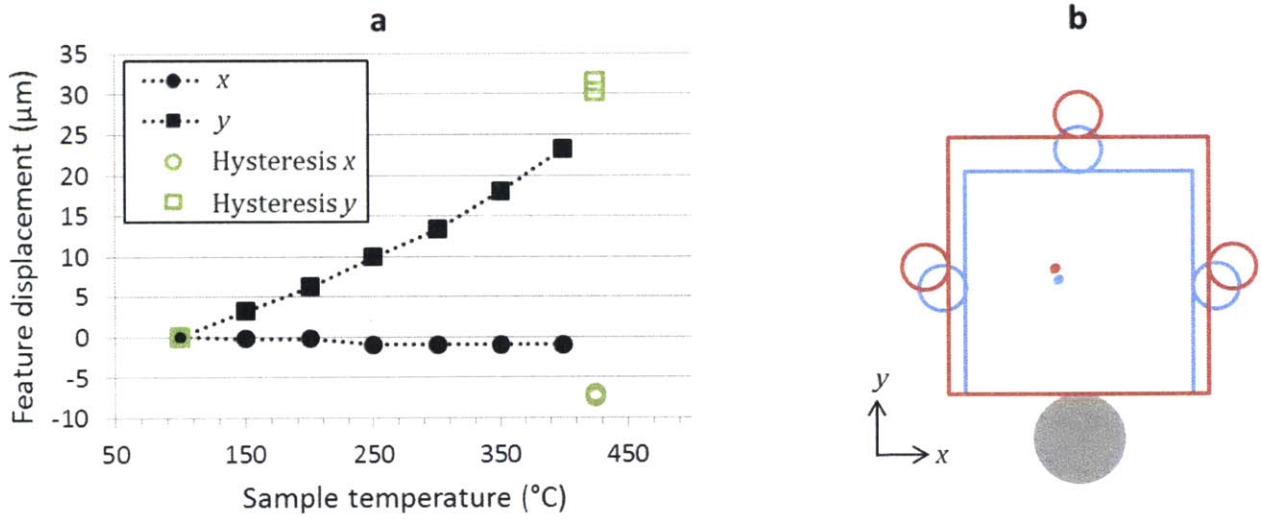

Figure 6-4. (a) Black filled points represent displacement of a sample feature in the plane of the substrate (***x*** and ***y***) as a function of sample temperature, as measured by tracking the feature with 125 nm pixel size of the X-ray fluorescence measurements. Green unfilled points demonstrate the lack of hysteresis for two temperature cycles after an initial ramp from 100 to 400°C. The green unfilled points were measured on a feature at a different substrate position, resulting in different absolute displacements than those of the black filled points. Error bars are within the width of the data markers. (b) Schematic of the top view of the sample during heating (not to scale). Grey filled circle is the fixed quartz post; smaller circles are quartz flexures; square outlines represent the perimeter of the substrate; and dots in the middle represent the tracked feature. As the substrate temperature rises (blue to red) and the substrate expands, the quartz flexures bend without slip against the substrate edges. While the expansion in the horizontal direction is distributed evenly among the left and right flexures, the expansion in the vertical direction is absorbed entirely by the top flexure.

Figure 6-4a also shows that the displacement in the y direction is far greater than the displacement in the x direction. This can be explained by the directionality of thermal expansion induced by the sample mounting mechanism and the choice of the measurement spot, being close to the center in x but far from the fixed post in y. Figure 6-4b shows a plan-view diagram of the sample face along with the positions of the fixed post and flexures at two different temperatures. As the substrate temperature rises and the substrate expands, the quartz flexures bend without slip against the substrate edges. While the expansion in the horizontal direction is distributed evenly among the left and right flexures, the expansion in the vertical direction is absorbed entirely by the top flexure. Thus, the expected displacement field due to thermal expansion varies linearly with distance from the fixed post for the y direction, and varies linearly with distance from the vertical centerline of the sample for the x direction. Because the sodalime glass substrate is thick compared to the multilayer thin-film device stack (1.6 mm compared to < 10 μm), the displacement due to the thermal expansion of the thin-film layers is negligible, and we expect the tracked feature to follow the displacement field of the substrate only. Since the tracked feature is in this case close to the center of the sample (indicated in Figure 6-4b), we expect far less displacement in the x direction that in the y direction, which is what is observed. Moreover, the displacement in the x and y directions have a near-linear trend with a slope that is consistent with the range of thermal expansion coefficients expected for sodalime glass for temperatures from 25–400°C ($9–21 \times 10^{-6}$ K^{-1}),[145] further confirming that thermal expansion of the substrate accounts for the observed thermal drift.

The hysteresis of the feature displacement is also measured by cycling the sample temperature from 100°C to 400°C three times, tracking a different feature than before. For each extreme, we wait 15 minutes for the temperature to stabilize. Ramping back down to 100°C after the initial ramp up to 400°C, the sample feature does not return to its previous position at 100°C to within the spatial resolution. There is a shift of -11 μm in the y direction and -4 μm in the x direction relative to the previous position at 100°C. This shift may be due to stick-slip motion between the flexures and substrate, possibly because the sample had not settled into a slip-free position on the flexures before heating.

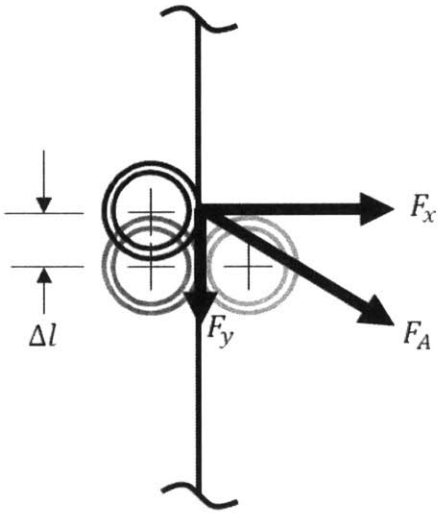

Figure 6-5. Example of non-ideal flexure-sample contact at flexure A. The light grey shows the initial position of the flexure before sample mounting; the dark grey shows the ideal position of the flexure after sample mounting, where the flexure is not displaced tangent to the sample edge; the black shows the misaligned flexure, with a tangential displacement of Δl. When Δl is large enough, the tangential flexure force F_y will overcome the force of friction and the flexure will slip along the sample edge.

For example, if flexure A is not centered on the sample edge upon mounting the sample, as in Figure 6-5, then the flexure imparts a force $F_y = k_f \Delta l$ tangential to the sample edge, where Δl is the tangential deviation of flexure A before heating the sample. The maximum tangential force allowable before slip occurs is equal to the force of static friction F_f between the flexure and sample edge

$$F_f = \mu_s F_N$$

where μ_s is the coefficient of static friction between the flexure and sample edge, and $F_N = F_x$ is the normal force imparted by the flexure. Upon heating the sample, the flexure ideally bends to accommodate the thermal expansion without slip, and Δl increases. However, the increase in Δl due to thermal expansion of the sample may increase F_y to the maximum allowable tangential force F_f, leading to slip.

For small deviations from ideal flexure placement, the normal force is $F_N \approx k_f d$, where k_f is the stiffness of the flexure as found in the previous section, and d is the ideal displacement of the flexures upon mounting the sample. The maximum allowable tangential deviation in the position of the flexure can be obtained by equating F_f and F_y:

$$F_f = F_y$$
$$\mu_s k_f d = k_f \Delta l$$
$$\Delta l = \mu_s d$$

Substituting the actual ideal displacement in our stage ($d = 0.5$ mm) and taking the worst-case literature value for the coefficient of static friction for glass-glass contact ($\mu_s = 0.9$),[146] we obtain $\Delta l = 450$ μm. Thus, the maximum allowable tangential deviation of the flexure-substrate contact from ideal placement is ~450 μm; any greater deviation would result in slip at the flexure-substrate interface due to the tangential component of the flexure force overcoming the force of static friction. This precision is difficult to achieve with manual mounting of the sample, and it is possible that the tangential deviation of one of the flexures upon initial mounting of the sample is close to the slip threshold of 450 μm. If this is the case, then upon heating, the tangential deviation increases to the slip threshold, at which point the flexure necessarily slips to a more stable position closer to ideal placement. This slip event brings the tangential deviation of the flexure below the slip threshold for subsequent thermal cycles, resulting in no additional slip events.

Indeed, using this shifted position as a new baseline position, the sample feature position shows no hysteresis when subsequently ramping back up to 400°C, down to 100°C, and back up to 400°C. These subsequent measurements are shown by the green unfilled points in Figure 6-4a. This indicates that the initial shift was a one-off event in which the sample settled into a more stable position in the sample mount, after which no measurable stick-slip displacements occur. Vibration annealing immediately after sample mounting, as is sometimes done for precision flexure-based kinematic couplings,[147] may prevent this initial stick-slip event in future experiments.

Figure 6-6 shows an example of the data that can be collected using this heating stage. From each of the selenium concentration maps shown in Figure 6-3 and from similar maps taken at intermediate temperatures (50, 150, 250, 350°C), the statistical distribution of the selenium concentration is extracted in a histogram accounting for all pixels of a map. Comparing these histograms of the selenium concentration at different temperatures, there are significant distribution changes, although these temperatures are significantly below

the highest processing temperature of CIGS layers. In particular, the low-concentration tail decreases, whereas the peak height increases with temperature. Pixels populating the low-concentration tail appear in the peak at higher temperatures, indicating that areas of low concentration get enriched by selenium as temperature increases. Thus, a homogenization of the selenium distribution is observed with increasing temperature. The relations between low- and high-concentration areas with grain boundaries and solar cell performance are discussed by West, *et al.*[148] Further experiments are necessary to show whether the change of the selenium distribution is caused by topological changes, densification of low-concentration areas, or stoichiometric changes. Additional applications of the heating stage for the study of CIGS layers involving combined XRF and X-ray-beam-induced current microscopy is discussed elsewhere.[149]

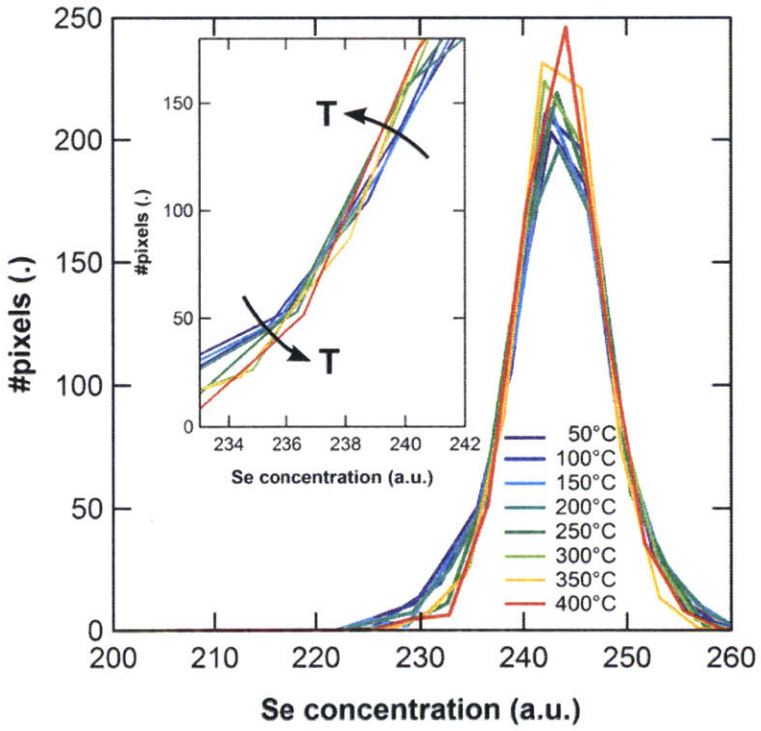

Figure 6-6. Statistical distribution of the selenium concentration in a 2.75 µm × 4.25 µm large area (the same as shown in Figure 2), measured at temperatures from 50 (purple) to 400°C (red) with 50°C increments. The inset shows a zoom into the low-selenium-concentration tail of the distribution.

6.3 Conclusion

In summary, I have designed and fabricated an *in-situ* sample stage for nanoscale X-ray spectromicroscopy of thin-film materials, capable of simulating realistic processing conditions and requiring minimal sample preparation. The stage can achieve sample temperature ramp rates of up to 300°C/min and a maximum sample temperature of 600°C, similar to the typical processing conditions for CIGS thin-films. Careful selection of construction materials also enables controlled non-oxidizing atmospheres inside the sample chamber such as H_2Se and H_2S. The unique flexure-based sample mount yields finely predictable thermal drift, allowing features on the order of 100 nm to be tracked and measured.

To our knowledge, the present work is the first demonstration of tracking a sample feature on a device-representative substrate with nanoscale resolution across such a large temperature range (25-400°C) under a controlled atmosphere. Thus, the stage enables previously unattainable *in-situ* studies on nanoscale defect kinetics under industrially relevant processing conditions, allowing a deeper understanding of how process conditions affect defect characteristics. Furthermore, it is possible to use the stage for *in-situ* optimization of process conditions, including time-temperature profiles and atmospheric conditions, with the goal of reducing the most detrimental defects. This is an important step toward expediting the cycle of learning and optimization for polycrystalline thin-film PV absorbers, with the ultimate goal of improving device efficiencies.

Lastly, I envision that the stage could be modified for use with other high-resolution spatially-resolved measurements. The highest resolution achieved here (125 nm) is limited not by the stage, but by the beamline. Thus, the stage may be transferrable to other beamlines for higher-resolution XRF, X-ray beam induced current measurements, as well as entirely different measurement techniques such as scanning electron microscopy and near-field scanning optical microscopy. The design is also anticipated to be used in next-generation dedicated instruments such as the planned In-Situ Nanoprobe at APS.[150]

Chapter 7

Conclusions

The path toward high-efficiency SnS-based PV devices is now more clear than ever before. Before this thesis, there were no known works directly correlating any type of defect density directly to the minority-carrier lifetime. This thesis takes important steps toward identifying the efficiency-limiting structural defects in present-day SnS-based PV devices, and showing several paths toward high-efficiency SnS-based PV devices by optimizing growth parameters.

The limits of using growth temperature as a parameter to control structural defects and minority-carrier diffusion length are delineated. For the best-performing SnS films grown at the highest growth temperature, the lifetime-limiting defects in SnS are not extended structural defects such as dislocations or grain boundaries. Rather, intragranular point defects distributed throughout the bulk of the SnS layer are likely responsible for the short minority-carrier lifetimes, and thus low efficiency, in present-day SnS-based PV devices. While the present work does not achieve a step-change in the efficiency of state-of-the-art SnS devices, it is the author's hope that these learnings will steer the focus of present-day SnS research toward the control of extrinsic and intrinsic point defect concentrations. Extrinsic defects may be reduced by using higher-purity feedstock SnS, as well as higher-purity materials for the growth and annealing environments. Characterization of low-concentration extrinsic defects is notoriously difficult. However, synchrotron X-ray fluorescence is particularly well-suited for this task, and the use of the temperature stage

developed in this thesis may help to identify detrimental contaminants, understand their kinetics, and measure their impact on minority-carrier lifetime if combined with X-ray beam induced current measurements.[149]

Control of the intrinsic point defect concentration, especially sulfur vacancy concentration, via annealing is a topic that has been explored by Hartman.[8] Based on Kröger-Vink theory, modern density functional theory calculations, and the assumption that tin vacancies account for the majority carrier concentration, Hartman calculates that the density of sulfur vacancies should be below 10^{11} cm^{-3} for annealing conditions identical to those used in this thesis, which would not likely affect the minority-carrier lifetime assuming a conservative estimate for the capture cross-section of a sulfur vacancy. However, it has since been suggested that sodium contamination in the SnS films may contribute to a fraction of the majority carrier concentration,[151] which may render this calculation an underestimate of the actual sulfur vacancy concentration. Thus, it is possible that sulfur vacancies may contribute to the low minority-carrier lifetime in present-day SnS. The cation to anion ratio, in this case Sn to S, may be used to indirectly estimate the sulfur vacancy concentration. However, measuring the ratio is a difficult task, and this is a well-known problem in other compound semiconductors. Rutherford backscattering spectrometry and secondary ion mass spectrometry are leading candidates for this measurement.

As work on reducing extrinsic and intrinsic point defect concentration progresses, extended structural defects will likely become the lifetime-limiting defects in SnS-based devices. This work shows that some grain boundaries, for example, are indeed highly recombination active. This loss mechanism can be reduced by passivating grain boundaries or reducing the density of grain boundaries by achieving larger grains through the optimization of process parameters. Post-growth annealing is one route toward the latter as found in Hartman, and has the added benefit of the potential to control intrinsic point defect concentrations. The here-presented work on SnS growth on van der Waals substrates suggests another route toward increasing grain size. We now know that the highly oriented nature of films grown in this manner would have the added benefit of preventing losses due to the anisotropic electron affinity of SnS. Ultimately, achieving a SnS film with low extended structural defect density will require the simultaneous

optimization of substrate type, growth temperature, and post-growth annealing parameters.

Bibliography

1 IPCC, *Climate Change 2014: Synthesis Report. Contribution of Working Groups I, II and III to the Fifth Assessment Report of the Intergovernmental Panel on Climate Change* (Geneva, Switzerland, 2014).

2 M.Z. Jacobson and M. a. Delucchi, *Energy Policy*, **39**, 1154 (2011).

3 R.C. Pietzcker, D. Stetter, S. Manger, and G. Luderer, *Applied Energy*, **135**, 704 (2014).

4 *Photovoltaics Report* (Freiburg, Germany, 2015).

5 D.B. Needleman, J.R. Poindexter, R.C. Kurchin, I.M. Peters, G. Wilson, and T. Buonassisi, *Energy and Environmental Science*, (2016).

6 *First Solar Annual Report* (2013).

7 V. Fthenakis, *MRS Bulletin*, **37**, 425 (2012).

8 K. Hartman, Annealing for Intrinsic Point-Defect Control and Enhanced Solar Cell Performance : The Case of H2S and Tin Sulfide (SnS), Massachusetts Institute of Technology, 2015.

9 D.B. Mitzi, O. Gunawan, T.K. Todorov, K. Wang, and S. Guha, *Solar Energy Materials and Solar Cells*, **95**, 1421 (2011).

10 R.C. Sharma and Y.A. Chang, *Binary Alloy Phase Diagrams, Vol. 3*, 3280 (1990).

11 V. Piacente, S. Foglia, and P. Scardala, *Journal of Alloys and Compounds*, **177**, 17 (1991).

12 R. Colin and J. Drowart, *The Journal of Chemical Physics*, **37**, 1120 (1962).

13 J. Marinace, *Physical Review*, **96**, 593 (1954).

14 W.H. St. Clair, B.K. Shibler, and I.S. Solet, *U.S. Bur. Mines Rept. Invest.*, (1954).

15 D.N. Klushin and V.Y. Chernykh, *Zhur. Neorg. Khim*, **5**, (1960).

16 H. Rau, *Ber. Bunsenges, Physik. Chem.*, **71**, (1967).

17 A.W. Richards, *Transactions of the Faraday Society*, **51**, 1193 (1955).

18 H. Wiedemeier and F.J. Csillag, *Thermochimica Acta*, **34**, 257 (1979).

19 I. Langmuir, *Journal of the American Chemical Society*, **54**, 2798 (1932).

20 G.M. Pound, *Journal of Physical and Chemical Reference Data*, **1**, 135 (1972).

21 V. Steinmann, R. Jaramillo, K. Hartman, R. Chakraborty, R.E. Brandt, J.R. Poindexter, Y.S. Lee, L. Sun, A. Polizzotti, H.H. Park, R.G. Gordon, and T. Buonassisi, *Advanced Materials*, **26**, 7488 (2014).

22 H. Wiedemeier and G. Von Schnering, *Z. Kristallogr.*, **148**, 295 (1978).

23 A. Ettema, R. de Groot, C. Haas, and T. Turner, *Physical Review B*, **46**, 7363 (1992).

24 W. Albers, C. Haas, H.J. Vink, and J.D. Wasscher, *Journal of Applied Physics*, **32**, 2220 (1961).

25 V. Stevanović, K. Hartman, R. Jaramillo, S. Ramanathan, T. Buonassisi, and P. Graf, *Applied Physics Letters*, **104**, 211603 (2014).

26 E. Bucher, in *Photoelectrochem. Photovoltaics Layer. Semicond.*, edited by A. Aruchamy (Kluwer Academic Publishers, Dordrecht, 1992), pp. 1–64.

27 P. Sinsermsuksakul, J. Heo, W. Noh, A.S. Hock, and R.G. Gordon, *Advanced Energy Materials*, **1**, 1116 (2011).

28 A. Aruchamy, *Photoelectrochemistry and Photovoltaics of Layered Semiconductors* (Springer Science & Business, 2013).

29 I. Lefebvre, M. Szymanski, J. Olivier-Fourcade, and J. Jumas, *Physical Review B*, **58**, 1896 (1998).

30 J. Vidal, S. Lany, M. d'Avezac, A. Zunger, A. Zakutayev, J. Francis, and J. Tate, *Applied Physics Letters*, **100**, 032104 (2012).

31 L. Makinistian and E. a. Albanesi, *Physica Status Solidi (B)*, **246**, 183 (2009).

32 A.P. Lambros, D. Geraleas, and N.A. Economou, *Journal of Physics and Chemistry of Solids*, **35**, 537 (1974).

33 T. Sorgenfrei, F. Hofherr, T. Jauß, and a. Cröll, *Crystal Research and Technology*, **7**, n/a (2013).

34 Z. Zainal, M.Z. Hussein, and A. Ghazali, *Solar Energy Materials and Solar Cells*, **40**, 347 (1996).

35 D. Avellaneda, G. Delgado, M.T.S. Nair, and P.K. Nair, *Thin Solid Films*, **515**, 5771 (2007).

36 R.W. Miles, O.E. Ogah, G. Zoppi, and I. Forbes, *Thin Solid Films*, **517**, 4702 (2009).

37 H. Noguchi, A. Setiyadi, H. Tanamura, T. Nagatomo, and O. Omoto, *Solar Energy Materials and Solar Cells*, **35**, 325 (1994).

38 M. Devika, K.T. Ramakrishna Reddy, N. Koteeswara Reddy, K. Ramesh, R. Ganesan, E.S.R. Gopal, and K.R. Gunasekhar, *Journal of Applied Physics*, **100**, 023518 (2006).

39 C. Cifuentes, M. Botero, E. Romero, C. Calderón, and G. Gordillo, *Brazilian Journal of Physics*, **36**, 1046 (2006).

40 K.T. Ramakrishna Reddy, P. Purandhara Reddy, P.K. Datta, and R.W. Miles, *Thin Solid Films*, **403-404**, 116 (2002).

41 F. Jiang, H. Shen, W. Wang, and L. Zhang, *Journal of The Electrochemical Society*, **159**, H235 (2012).

42 K. Ramakrishna Reddy, N. Koteswara Reddy, and R. Miles, *Solar Energy Materials and Solar Cells*, **90**, 3041 (2006).

43 W. Shockley and H.J. Queisser, *Journal of Applied Physics*, **32**, 510 (1961).

44 K. Emery and D. Myers, *NREL*, Reference Solar Spectral Irradiance, Accessed October 2014.

45 R.D. Engelken, *Journal of The Electrochemical Society*, **134**, 2696 (1987).

46 P. Pramanik, P.K. Basu, and S. Biswas, *Chemical Analysis*, **150**, 269 (1987).

47 E. Turan, M. Kul, a S. Aybek, and M. Zor, *Journal of Physics D: Applied Physics*, **42**, 245408 (2009).

48 M. Ristov, G. Sinadinovski, M. Mitreski, and M. Ristova, *Solar Energy Materials and Solar Cells*, **69**, 17 (2001).

49 B. Ghosh, M. Das, P. Banerjee, and S. Das, *Applied Surface Science*, **254**, 6436 (2008).

50 M. Ichimura, K. Takeuchi, Y. Ono, and E. Arai, *Thin Solid Films*, **361-362**, 98 (2000).

51 A. Ghazali, Z. Zainal, M. Zobir Hussein, and A. Kassim, *Solar Energy Materials and Solar Cells*, **55**, 237 (1998).

52 L.S. Price, I.P. Parkin, A.M.E. Hardy, R.J.H. Clark, T.G. Hibbert, and K.C. Molloy, *Analysis*, 1792 (1999).

53 A.T. Kana, T.G. Hibbert, M.F. Mahon, K.C. Molloy, I.P. Parkin, and L.S. Price, *Polyhedron*, **20**, 2989 (2001).

54 I.P. Parkin, L.S. Price, T.G. Hibbert, and K.C. Molloy, *Journal of Materials Chemistry*, **11**, 1486 (2001).

55 B.P. Bade, S.S. Garje, Y.S. Niwate, M. Afzaal, and P. O'Brien, *Chemical Vapor Deposition*, **14**, 292 (2008).

56 J.Y. Kim and S.M. George, *J. Phys. Chem.*, **114**, 17597 (2010).

57 S. Lopez and A. Ortiz, *Semiconductor Science and Technology*, **9**, 2130 (1994).

58 N. Koteeswara Reddy and K.T. Ramakrishna Reddy, *Solid-State Electronics*, **49**, 902 (2005).

59 T.H. Sajeesh, A.R. Warrier, C.S. Kartha, and K.P. Vijayakumar, *Thin Solid Films*, **518**, 4370 (2010).

60 T. Minemura, K. Miyauchi, K. Noguchi, K. Ohtsuka, H. Nakanishi, and M. Sugiyama, *Physica Status Solidi (C)*, **6**, 1221 (2009).

61 W. Guang-Pu, Z. Zhi-Lin, Z. Wei-Ming, G. Xiang-Hong, C. Wei-Qun, H. Tanamura, M. Yamaguchi, H. Noguchi, T. Nagatomo, and O. Omoto, in *Proc. 1994 IEEE 1st World Conf. Photovolt. Energy Convers. - WCPEC (A Jt. Conf. PVSC, PVSEC PSEC)* (IEEE, 1994), pp. 365–368.

62 K. Hartman, J.L. Johnson, M.I. Bertoni, D. Recht, M.J. Aziz, M. a. Scarpulla, and T. Buonassisi, *Thin Solid Films*, **519**, 7421 (2011).

63 Yanuar, F. Guastavino, C. Llinares, K. Djessas, and G. Masse, *Journal of Materials Science Letters*, **19**, 2135 (2000).

64 N.K. Reddy, K. Ramesh, R. Ganesan, K.T.R. Reddy, K.R. Gunasekhar, and E.S.R. Gopal, *Applied Physics A: Materials Science and Processing*, **83**, 133 (2006).

65 A. Tanusevski and D. Poelman, *Solar Energy Materials and Solar Cells*, **80**, 297 (2003).

66 H. Nozaki, M. Onoda, M. Sekita, K. Kosuda, and T. Wada, *Journal of Solid State Chemistry*, **178**, 245 (2005).

67 S.A. Bashkirov, V.F. Gremenok, V.A. Ivanov, V.V. Lazenka, and K. Bente, *Thin Solid Films*, **520**, 5807 (2012).

68 R. Jaramillo, V. Steinmann, C. Yang, K. Hartman, R. Chakraborty, J.R. Poindexter, M.L. Castillo, R. Gordon, and T. Buonassisi, *Journal of Visualized Experiments*, (2015).

69 D. Bonnet, *Thin Solid Films*, **361-362**, 547 (2000).

70 P. Sinsermsuksakul, K. Hartman, S. Bok Kim, J. Heo, L. Sun, H. Hejin Park, R.

Chakraborty, T. Buonassisi, and R.G. Gordon, *Applied Physics Letters*, **102**, 053901 (2013).

71 P. Sinsermsuksakul, L. Sun, S.W. Lee, H.H. Park, S.B. Kim, C. Yang, and R.G. Gordon, *Advanced Energy Materials*, **4**, (2014).

72 R. Jaramillo, M. Sher, B.K. Ofori-Okai, V. Steinmann, C. Yang, K. Hartman, K.A. Nelson, A.M. Lindenberg, R.G. Gordon, and T. Buonassisi, *Journal of Applied Physics*, **119**, 035101 (2016).

73 N.M. Mangan, R.E. Brandt, V. Steinmann, R. Jaramillo, C. Yang, J.R. Poindexter, R. Chakraborty, H.H. Park, X. Zhao, R.G. Gordon, and T. Buonassisi, *Journal of Applied Physics*, **118**, 115102 (2015).

74 D.K. Schroder, *Semiconductor Material and Device Characterization* (John Wiley & Sons, Inc., Hoboken, NJ, USA, 2005).

75 D. Macdonald and L.J. Geerligs, *Applied Physics Letters*, **85**, 4061 (2004).

76 W. Seifert, G. Morgenstern, and M. Kittler, *Semiconductor Science and Technology*, **8**, 1687 (1993).

77 S. Pizzini, *Journal of The Electrochemical Society*, **133**, 2363 (1986).

78 J. Chen and T. Sekiguchi, *Japanese Journal of Applied Physics*, **46**, 6489 (2007).

79 J.H. Werner, J. Mattheis, and U. Rau, *Thin Solid Films*, **480-481**, 399 (2005).

80 U. Rau and J.H. Werner, *Applied Physics Letters*, **84**, 3735 (2004).

81 P. Wurfel, *Physics of Solar Cells*, 2nd editio (Wiley-VCH, 2010).

82 M.A. Green, *Solar Cells: Operating Principles, Technology and System Applications* (University of New South Wales, Kensington, 1998).

83 R. Scheer and H.-W. Schock, *Chalcogenide Photovoltaics: Physics, Technologies, and Thin Film Devices* (Wiley-VCH, 2011).

84 S.M. Allen and E.L. Thomas, *The Structure of Materials* (John Wiley & Sons, Inc., New York, 1999).

85 W. Shockley and W. Read, *Physical Review*, **87**, 835 (1952).

86 R. Hall, *Physical Review*, **87**, 387 (1952).

87 C. Donolato, *Journal of Applied Physics*, **84**, 2656 (1998).

88 V. Kveder, M. Kittler, and W. Schröter, *Physical Review B*, **63**, 115208 (2001).

89 P.R. Wilshaw, T.S. Fell, and M.D. Coteau, *Le Journal de Physique IV*, **01**, C6 (1991).

90 M. Ohring, *Materials Science of Thin Films: Deposition and Structure*, 2nd ed. (Academic Press, Amsterdam, 2002).

91 C. V. Thompson, *MIT Course 3.44 Lecture Notes*, (2013).

92 C. V. Thompson, *Annual Review of Materials Science*, **30**, 159 (2000).

93 B.A. Movchan and A. V. Demchishin, *Phys. Met. Metallogr.*, **28**, (1969).

94 H.T.G. Hentzell, C.R.M. Grovenor, and D.A. Smith, *Journal of Vacuum Science & Technology A: Vacuum, Surfaces, and Films*, **2**, 218 (1984).

95 C.. Ferekides, D. Marinskiy, V. Viswanathan, B. Tetali, V. Palekis, P. Selvaraj, and D.. Morel, *Thin Solid Films*, **361-362**, 520 (2000).

96 W.N. Shafarman and J. Zhu, *Thin Solid Films*, **361**, 473 (2000).

97 M. Devika, N. Koteeswara Reddy, D. Sreekantha Reddy, Q. Ahsanulhaq, K. Ramesh, E.S.R. Gopal, K.R. Gunasekhar, and Y.B. Hahn, *Journal of The Electrochemical Society*, **155**, H130 (2008).

98 Y. Guo, W. Shi, Y. Zhang, L. Wang, and G. Wei, *Proceedings of SPIE*, **6984**, 69841P (2008).

99 P.A. Nwofe, K.T.R. Reddy, G. Sreedevi, J.K. Tan, I. Forbes, and R.W. Miles, *Energy*

Procedia, **15**, 354 (2012).

100 R. Chakraborty, V. Steinmann, N.M. Mangan, R.E. Brandt, J.R. Poindexter, R. Jaramillo, J.P. Mailoa, K. Hartman, a. Polizzotti, C. Yang, R.G. Gordon, and T. Buonassisi, *Applied Physics Letters*, **106**, 203901 (2015).

101 GIMP - The GNU Image Manipulation Program, www.gimp.org (2001-2015).

102 M.D. Abràmoff, P.J. Magalhães, and S.J. Ram, *Biophotonics International*, **11**, 36 (2004).

103 R.E. Banai, H. Lee, M. a. Motyka, R. Chandrasekharan, N.J. Podraza, J.R.S. Brownson, and M.W. Horn, *IEEE Journal of Photovoltaics*, 1 (2013).

104 N. Ashkenov, B.N. Mbenkum, C. Bundesmann, V. Riede, M. Lorenz, D. Spemann, E.M. Kaidashev, a. Kasic, M. Schubert, M. Grundmann, G. Wagner, H. Neumann, V. Darakchieva, H. Arwin, and B. Monemar, *Journal of Applied Physics*, **93**, 126 (2003).

105 S.Z. Karazhanov, P. Ravindran, a. Kjekshus, H. Fjellvåg, U. Grossner, and B.G. Svensson, *Journal of Applied Physics*, **100**, (2006).

106 V. Quemener, M. Alnes, L. Vines, P. Rauwel, O. Nilsen, H. Fjellvåg, E. V Monakhov, and B.G. Svensson, *Journal of Physics D: Applied Physics*, **45**, 315101 (2012).

107 H. Hejin Park, R. Heasley, and R.G. Gordon, *Applied Physics Letters*, **102**, 1 (2013).

108 C. Persson, C. Platzer-Björkman, J. Malmström, T. Törndahl, and M. Edoff, *Physical Review Letters*, **97**, 146403 (2006).

109 R.E. Banai, L.A. Burton, S.G. Choi, F. Hofherr, T. Sorgenfrei, A. Walsh, B. To, A. Cröll, and J.R.S. Brownson, *Journal of Applied Physics*, **116**, 013511 (2014).

110 G.B. Harris, *The London, Edinburgh, and Dublin Philosophical Magazine and Journal of Science*, **43**, 113 (1952).

111 J.F. Nye, *Physical Properties of Crystals: Their Representation by Tensors and Matrices*, 2nd ed. (Clarendon Press, Glasgow, 1960).

112 M. Burgelman, P. Nollet, and S. Degrave, *Thin Solid Films*, **361**, 527 (2000).

113 J.W. Orton and M.J. Powell, *Reports on Progress in Physics*, **43**, 1263 (1980).

114 H.C. Card and E.S. Yang, *IEEE Transactions on Electron Devices*, **24**, 397 (1977).

115 O.F. Vyvenko, O. Krüger, and M. Kittler, *Applied Physics Letters*, **76**, 697 (2000).

116 V. Steinmann, R. Chakraborty, P. Rekemeyer, K. Hartman, R.E. Brandt, A. Polizzotti, C. Yang, T. Moriarty, S. Gradecak, R.G. Gordon, and T. Buonassisi, *Submitted to Advanced Energy Materials*, (2016).

117 S. Siebentritt, *Solar Energy Materials and Solar Cells*, **95**, 1471 (2011).

118 T. Gokmen, O. Gunawan, T.K. Todorov, and D.B. Mitzi, *Applied Physics Letters*, **103**, 103506 (2013).

119 P.O. Grabitz, U. Rau, and J.H. Werner, *Physica Status Solidi (A) Applications and Materials Science*, **202**, 2920 (2005).

120 A. Wangperawong, S.M. Herron, R.R. Runser, C. Hägglund, J.T. Tanskanen, H.-B.-R. Lee, B.M. Clemens, and S.F. Bent, *Applied Physics Letters*, **103**, 052105 (2013).

121 W. Wang, K.K. Leung, W.K. Fong, S.F. Wang, Y.Y. Hui, S.P. Lau, Z. Chen, L.J. Shi, C.B. Cao, and C. Surya, *Journal of Applied Physics*, **111**, 093520 (2012).

122 S.F. Wang, W.K. Fong, W. Wang, and C. Surya, *Thin Solid Films*, **564**, 206 (2014).

123 X. Li, W. Cai, J. An, S. Kim, J. Nah, D. Yang, R. Piner, A. Velamakanni, I. Jung, E. Tutuc, S.K. Banerjee, L. Colombo, and R.S. Ruoff, *Science*, **324**, 1312 (2009).

124 G. Borin Barin, Y. Song, I. de Fátima Gimenez, A.G. Souza Filho, L.S. Barreto, and J. Kong, *Carbon*, **84**, 82 (2015).

125 M.-J. Sher, C.B. Simmons, J.J. Krich, A.J. Akey, M.T. Winkler, D. Recht, T. Buonassisi, M.J. Aziz, and A.M. Lindenberg, *Applied Physics Letters*, **105**, 053905 (2014).

126 F. Gao, G.L. Carr, C.D. Porter, D.B. Tanner, G.P. Williams, C.J. Hirschmugl, B. Dutta, X.D.

Wu, and S. Etemad, *Physical Review B*, **54**, 700 (1996).

127 H.H. Park, R. Heasley, L. Sun, V. Steinmann, R. Jaramillo, K. Hartman, R. Chakraborty, P. Sinsermsuksakul, D. Chua, T. Buonassisi, and R.G. Gordon, *Progress in Photovoltaics: Research and Applications*, **20**, n/a (2014).

128 G.A. Parks, *Journal of Geophysical Research: Solid Earth*, **89**, 3997 (1984).

129 J.G. Che, C.T. Chan, W.-E. Jian, and T.C. Leung, *Physical Review B*, **57**, 1875 (1998).

130 M.I. Bertoni, D.P. Fenning, M. Rinio, V. Rose, M. Holt, J. Maser, and T. Buonassisi, *Energy & Environmental Science*, **4**, 4252 (2011).

131 J.F. Creemer, S. Helveg, G.H. Hoveling, S. Ullmann, a M. Molenbroek, P.M. Sarro, and H.W. Zandbergen, *Ultramicroscopy*, **108**, 993 (2008).

132 T. Yaguchi, M. Suzuki, A. Watabe, Y. Nagakubo, K. Ueda, and T. Kamino, *Journal of Electron Microscopy*, **60**, 217 (2011).

133 L.F. Allard, S.H. Overbury, W.C. Bigelow, M.B. Katz, D.P. Nackashi, and J. Damiano, *Microscopy and Microanalysis*, **18**, 656 (2012).

134 S. Mehraeen, J.T. McKeown, P. V Deshmukh, J.E. Evans, P. Abellan, P. Xu, B.W. Reed, M.L. Taheri, P.E. Fischione, and N.D. Browning, *Microscopy and Microanalysis*, **19**, 470 (2013).

135 E. de Smit, I. Swart, J.F. Creemer, G.H. Hoveling, M.K. Gilles, T. Tyliszczak, P.J. Kooyman, H.W. Zandbergen, C. Morin, B.M. Weckhuysen, and F.M.F. de Groot, *Nature*, **456**, 222 (2008).

136 M.I. Ahmad, D.G. Van Campen, J.D. Fields, J. Yu, V.L. Pool, P.A. Parilla, D.S. Ginley, M.F.A.M. Van Hest, and M.F. Toney, *Review of Scientific Instruments*, **86**, 013902 (2015).

137 S. Hudelson, B.K. Newman, S. Bernardis, D.P. Fenning, M.I. Bertoni, M.A. Marcus, S.C. Fakra, B. Lai, and T. Buonassisi, *Advanced Materials*, **22**, 3948 (2010).

138 S. Hudelson, High Temperature Investigations of Crystalline Silicon Solar Cell Materials, Massachusetts Institute of Technology, 2009.

139 D.P. Fenning, B.K. Newman, M.I. Bertoni, S. Hudelson, S. Bernardis, M.A. Marcus, S.C. Fakra, and T. Buonassisi, *Acta Materialia*, **61**, 4320 (2013).

140 R. Chakraborty, J. Serdy, B. West, M. Stuckelberger, B. Lai, J. Maser, M.I. Bertoni, M.L. Culpepper, and T. Buonassisi, *Review of Scientific Instruments*, **86**, 113705 (2015).

141 B.H.W.S. De Jong, R.G.C. Beerkens, and P.A. van Nijnatten, in *Ullmann's Encycl. Ind. Chem.* (Wiley-VCH Verlag GmbH & Co. KGaA, Weinheim, Germany, 2000).

142 D.L. Blanding, *Exact Constraint: Machine Design Using Kinematic Principles* (ASME Press, New York, 1999).

143 W. Yun, B. Lai, Z. Cai, J. Maser, D. Legnini, E. Gluskin, Z. Chen, a. a. Krasnoperova, Y. Vladimirsky, F. Cerrina, E. Di Fabrizio, and M. Gentili, *Review of Scientific Instruments*, **70**, 2238 (1999).

144 B. West, M. Stuckelberger, A. Jeffries, S. Gangama, B. Lai, B. Stripe, J.M. Maser, V. Rose, S. Vogt, and M. Bertoni, *Manuscript in Preparation*.

145 B.C. Schmid, A.N. Finn, and J.C. Young, *Bureau of Standards Journal of Research*, **12**, 421 (1934).

146 P.J. Blau, *ASM Handbook, Volume 18 - Friction, Lubrication, and Wear Technology* (ASM International, 1992).

147 A.H. Slocum and M.L. Culpepper, *Precision Engineering*, **36**, 55 (2012).

148 B. West, M. Stuckelberger, B. Lai, B. Stripe, J.M. Maser, V. Rose, S. Vogt, and M. Bertoni, *Manuscript in Preparation*.

149 M. Stuckelberger, B. West, S. Husein, H. Guthrey, M. Al-Jassim, R. Chakraborty, T. Buonassisi, J.M. Maser, B. Lai, B. Stripe, V. Rose, and M. Bertoni, in *Proc. IEEE PVSC* (New Orleans, 2015).

150 J. Maser, B. Lai, T. Buonassisi, Z. Cai, S. Chen, L. Finney, S.-C. Gleber, C. Jacobsen, C. Preissner, C. Roehrig, V. Rose, D. Shu, D. Vine, and S. Vogt, *Metallurgical and Materials Transactions A*, **45**, 85 (2014).

151 V. Steinmann, R.E. Brandt, R. Chakraborty, R. Jaramillo, M. Young, B.K. Ofori-Okai, C. Yang, A. Polizzotti, K.A. Nelson, R.G. Gordon, and T. Buonassisi, *APL Materials*, **4**, 026103 (2016).